Numerical modelling of particle impact and residual stresses in cold sprayed coatings: A review

Surface & Coatings Technology 409 (2021) 126835

Contents lists available at ScienceDirect

Surface & Coatings Technology

journal homepage: www.elsevier.com/locate/surfcoat

Numerical modelling of particle impact and residual stresses in cold sprayed coatings: A review

Ahmed Fardan [a,b], Christopher C. Berndt [c], Rehan Ahmed [b,*]

[a] Department of Industrial and Materials Science, Chalmers University of Technology, SE-412 96 Göteborg, Sweden
[b] School of Engineering and Physical Sciences, Heriot-Watt University, Edinburgh EH14 4AS, UK
[c] Surface Engineering for Advanced Materials (SEAM), Swinburne University of Technology, Hawthorn, Victoria 3122, Australia

ARTICLE INFO

Keywords:
Cold spray
Residual stress
Finite element analysis
Impact modelling
Particle impact
Particle deformation

ABSTRACT

Cold spray technology provides protective coatings, additive manufacturing and repair to a wide array of industrial sectors. Alternative tags for cold spray include, kinetic metallisation, kinetic fusion, hypersonic spray, gas dynamic cold spray, cold spray printing, and cold spray additive manufacturing. These processes employ the same physics principles of accelerating micrometre-sized particles to supersonic velocities that impact and adhere onto a suitably prepared substrate. Numerical modelling has been used extensively to study particle impact modelling. The prediction of critical velocity, deformation mechanism and, more recently, residual stresses have been areas of interest that have been evaluated by numerical methods such as Lagrangian, Eulerian, Smoothed Particle Hydrodynamics, Coupled Eulerian-Lagrangian, and Molecular Dynamics. The crucial findings of these models are summarised, and their comparative outcomes assessed with a critical analysis of their merits and weaknesses. The process parameters applied in the simulations such as particle diameter, impact velocity, pre-heat temperature and material chemistry is compiled. The experimental techniques used for residual stress measurements; such as X-ray diffraction, neutron diffraction, material removal, curvature measurement and deformation techniques, are concisely reviewed from the context of being applied to cold spray deposits.

1. Introduction

1.1. Cold spray technology

Cold spray (CS) technology belongs to the group of thermal spray processes in which micrometre-sized particles (5–100 μm) are accelerated to supersonic velocities (300–1200 m/s) through a de-Laval nozzle to impact a substrate and form a coating [1–3]. Unlike thermal spray coating, in CS technology, the particle temperature is lower than its melting point [2,3]. Adhesion to the substrate and internal splat-to-splat cohesion is achieved largely through metallurgical bonding and mechanical interlocking caused by the increased local plastic deformation in the particle/substrate interface [2,4,5]. Since CS processing takes place at a much lower temperature than conventional thermal spray technology, then common issues such as oxidation, melting, evaporation, thermal residual stresses and phase transformation can be avoided [5–8]. CS coatings are used in manufacturing and heavy machine industries: for example, aerospace, automotive, medical, marine and other fields. The coating protects the substrate from aggressive environments such as low temperature corrosion from fluids, oxidation at high temperature, and harsh reactive environments. CS has found extensive niche applications in additive manufacturing (known as CSAM, cold spray additive manufacturing) to manufacture components and for repair overhaul [5,9–12]. Residual stresses are developed during coating deposition and have been found to significantly impact component life. As the impact dynamics are boundary conditions that control the development of residual stress, it is important that the influence of CS processing parameters be fully understood.

The impact velocity of the particle plays a vital role in the splat deformation and bonding mechanism between the particle and the substrate [13,14]. The particles must be deposited at a critical minimum velocity that leads to adiabatic shear instabilities (ASI), which causes metallurgical bonding due to explosive cladding [15,16]. When a particle impacts the substrate there are changes in temperature and plastic strains that are depicted in Fig. 1a. This leads to localized heating that then leads to localized plastic flow, which is also known as adiabatic shear. There is a point of thermal instability known as ASI that arises when thermal softening becomes larger than the rate of strain hardening

* Corresponding author.
E-mail address: R.Ahmed@hw.ac.uk (R. Ahmed).

https://doi.org/10.1016/j.surfcoat.2021.126835
Received 30 October 2020; Received in revised form 5 December 2020; Accepted 28 December 2020
Available online 12 January 2021

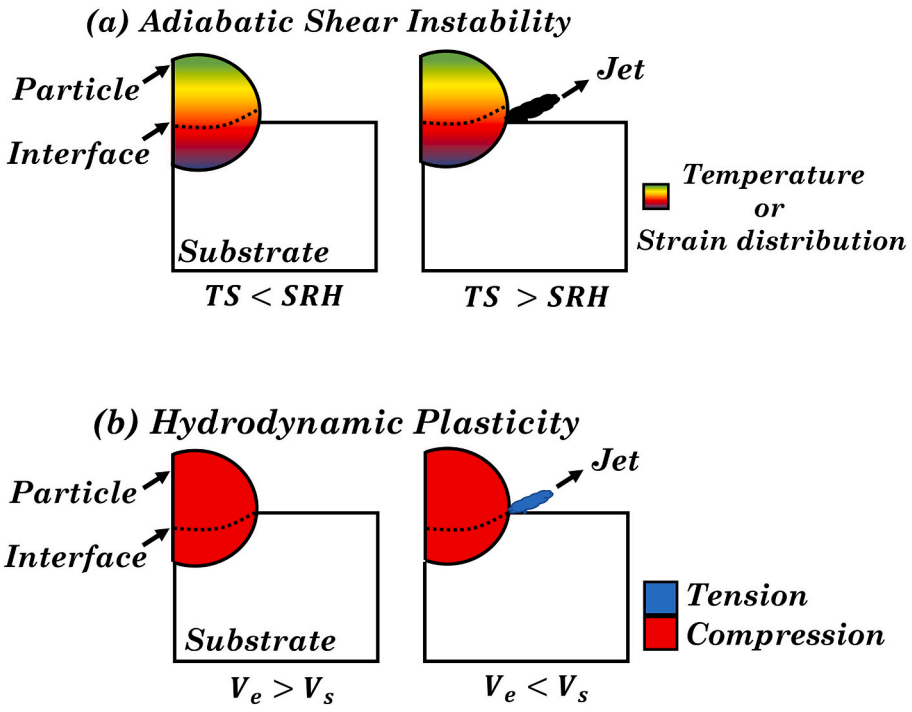

Fig. 1. Schematic representation of the jet formation due to (a) Adiabatic Shear Instability, first proposed by Assadi et al. [15] and (b) Hydrodynamic Plasticity proposed by Hassani et al. [18]. *TS* = thermal softening, *SRH* = strain rate hardening, V_e = edge velocity, V_s = shock velocity.

[17]. At this point of instability, jetting is found to occur in the periphery of the particle. But a recent hypothesis claims that the bonding is due to hydrodynamic plasticity and not ASI [18]. This study performed simulations with and without thermal softening and found that the plastic strain distribution and particle deformation was similar. It was argued that the jetting was caused due to pressure release and not ASI. Pressure waves are generated as the particle impacts the substrate. The generated pressure waves are compressive and are non-uniformly distributed in the particle and substrate (Fig .1b). The two velocities of interest are V_e (edge velocity) and V_s (shock velocity). During the early stages $V_e > V_s$ but a point is reached when $V_S > V_e$. This is the point where the hydrodynamic stresses exceed the flow strength of the material and jetting occurs [18–20]. Other studies dealing with hypervelocity impacts such as liquid droplet impact, shaped-charge jetting and explosion welding have also concluded that the jetting is caused due to the pressure release, hence agreeing with this mechanism [19,20]. The paper proposing hydrodynamic plasticity [18] as the mechanism for the bonding rather than adiabatic shear instability (ASI) led to a debate between Assadi et al. [21] and Hassani et al. [22]. The discussion points by Hassani et al. [22] are convincing; however, further investigations are worthwhile to examine any validity for ASI can completely be ignored.

The critical velocity of the particle is a material-specific parameter defined by the material properties of density, particle size and morphology [13,23]. These mechanisms of adhesion can be investigated by experimental studies; but herein lie fundamental practical limitations. For example, when a CS particle impacts a substrate, significant plastic deformation takes place for 0–100 ns; resulting in very high strain-rates (about 10^7 s^{-1}) [4]. The impact process and particle deformation cannot be acutely observed during coating deposition. In fact, experimental analysis of single and multiple impacts relies on post coating analysis. Numerical methods can, therefore, provide insights concerning the understanding of the impact and deformation processes.

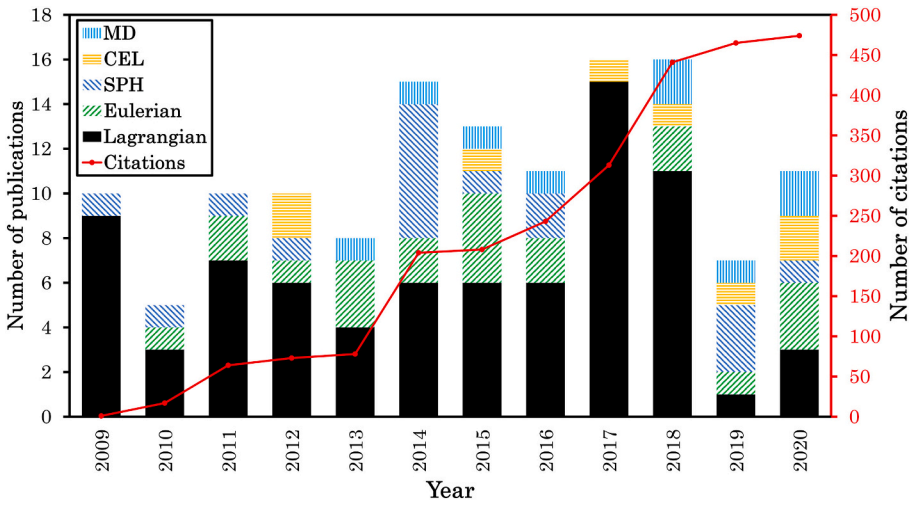

Fig. 2. Number of reported publications on cold sprayed particle impact numerical models and the yearly rise in the number of citations (until July 2020).

1.2. Overview of modelling methods

Table 1 lists the advantages, disadvantages, computational accuracy and efficiency of the different modelling techniques used to model cold spray particle impact. And Table 2 list numerical modelling process parameters for particles impacting a substrate. The bulk of the published work studies the effect of particle size, impact velocity and particle/substrate preheat temperature. Many numerical simulations have been developed to study the impact and deformation process of the particle and substrate under different constraints such as material combination [2,4,14,15,24], impact velocity [4,14,25], particle diameter [4,26], preheating temperature [3,27], mesh size [13], impact angle [13] and impact configuration [28]. Methods for modelling particle impact include Smoothed Particle Hydrodynamics (SPH), the Lagrangian method, Arbitrary Lagrangian Eulerian (ALE) and the Eulerian method [27,29]. There have also been studies conducted by Coupled Eulerian-Lagrangian (CEL) and Molecular Dynamics [18,30].

The Lagrangian method has been widely used to model high-velocity impact but there is an issue of excessive mesh distortion that leads to the termination of the program. Other issues include very high plastic strain, rebound of particles and unrealistic deformation of the particle and substrate. Some publications use adaptive meshing e.g. ALE in the Lagrangian method to provide a strain history that is sequenced with respect to the deformation time [27,31–36]. Another advantage of using the Lagrangian method is the use of the axisymmetric method with heat transfer that reduces the computational time significantly. With the advancement in computational software, Eulerian methods have been used widely because the deformation simulation is comparable to experimental observations. But one disadvantage of using the Eulerian method is that the contact properties, for instance, conductance and coefficient of friction, cannot be varied since the software (e.g., Abaqus FEA) employs default contact interactions [37]. This software limitation can be overcome by using the Coupled Eulerian-Lagrangian (CEL) method in which the particle is Eulerian, and the substrate is Lagrangian. SPH is another form of the Lagrangian method in which the elements are discretized as particles; as demonstrated by examples based on this method [26,38–41]. Molecular Dynamics (MD) is also being used to model nano-particle impact to study dislocation and adhesion mechanisms [30].

Fig. 2 depicts the yearly publications and citations of various finite element models in peer-reviewed journals. The Lagrangian method has been the most used method due to its availability in commercial software. However, there has been a reduction in the number of publications from 2017 and the usage of other methods such as CEL and Eulerian have increased. Most of the numerical models ($n = 84$) use Lagrangian formulation, while $n = 23$ for Eulerian, $n = 17$ for SPH, and $n = 10$ for CEL. There has been a steady increase in citations with every year showing that numerical modelling is a highly researched topic that is heading towards interlinking multi-scale models. The use of MD simulations, which is adept at studying stress, strain and temperature effects under high-speed impacts, is noticed in Fig. 2. Several MD simulations have examined dislocations and other microstructural changes using Quasi Coarse-Grained Dynamics (QCGD) [42,43]. However, the particle sizes are in the range of nanometres (nm), which are difficult to relate to CS practice.

1.3. Model assumptions

There are basic assumptions considered when modelling the particle impact. In most of the cases, the particle is assumed to be perfectly spherical. This condition may not be valid in experiments since there can be deviations from spherical morphologies [36]. Additionally, small satellites can be attached to particles that arise from powder manufacturing processes such as atomization [44]. Another assumption is that the impact velocity for multiple particle impacts is simplified to have the same velocity. But in experiments, there is a velocity distribution based on the particle size distribution [44].

It has been observed that only some numerical models consider heat transfer, which is a limitation since an important outcome is to predict critical velocity. For instance, numerical studies coupled with experimental validation show that the critical velocity decreases as the initial particle temperature is increased [29,45]. Therefore, consideration of heat transfer within the model improves the validation accuracy.

There are other phenomena that cannot be modelled or are difficult to model by finite element methods. These phenomena include the effect of surface roughness, micro-cracks at the interface, stresses due to phase transformation, stress relaxation, coating-substrate bonding, splat-splat bonding, and interactions among these material behaviours [6,46]. These are important phenomena that influence cold spray technology and, especially, residual stresses predicted without these phenomena might not be accurate. Furthermore, the material properties used for the residual stress modelling can affect the residual stress profiles obtained [47]. Section 7 on 'Future research' provides techniques that address these issues for researchers.

1.4. Residual stresses

Residual stresses affect the integrity, performance, service life, fatigue performance and corrosion resistance [48,49] of coated components. There have been experimental studies dedicated to measuring residual stresses in CS coatings and its effect on coating adhesion and fatigue life of the component [23,50–53]. The residual stresses formed in the cold sprayed coating is mostly compressive due to the plastic deformation and peening effect [49,54]. There are different stresses formed during and post particle impact that affect the final residual stress state in CS coatings [55]. These three stresses are listed below.

(a) Peening stress: The high impact velocity of the particles causes compressive stresses in the coating. The underlying mechanism is comparable to the shot peening process used in engineering components to impart compressive stresses. Peening stresses improve the fatigue life and delays crack propagation in components.
(b) Quenching stress: Quenching stress is caused due to the contraction of the impacted particle that is restricted by the underlying coating or substrate. Quenching stresses are tensile due to the restricted contraction of the splat that is at a higher temperature, and the underlying coating or material that is at a lower temperature. Quenching and peening stresses are often grouped and referred to as deposition stresses.
(c) Thermal stress: Thermal stresses are caused due to the difference in coefficient of thermal expansion (CTE) of the coating and substrate. The stresses can be tensile or compressive depending on the mismatch of CTE. For example, tensile stresses will be formed in the coating and compressive stresses in the substrate if $CTE_{coating} > CTE_{substrate}$.

Thermal and quenching stresses do not affect largely the residual stress state in CS coatings due to the lower deposition temperatures. The thermal stresses are magnified for substrate temperatures greater than 400 °C [56,57]. Thermal and quenching stresses can be ignored if temperatures are lower than 400 °C.

Residual stresses can be measured by experimental techniques such as X-ray diffraction (XRD) [58–68]; neutron diffraction [55,65,66,69–82]; curvature measurements [49,62,83,84]; material removal such as hole-drilling and layer removal [60,62,68,79,83–87]; digital image correlation [88]; deformation measurements such as strain gauges [89]; the contour method [71,72]; the ring-opening test [90–93]; and nanoindentation [94]. There are limitations to experimental techniques: they take time and resources to obtain accurate residual stress values [95]. There are also differences in the experimental methods of measuring residual stress; e.g., the layer removal and hole drilling

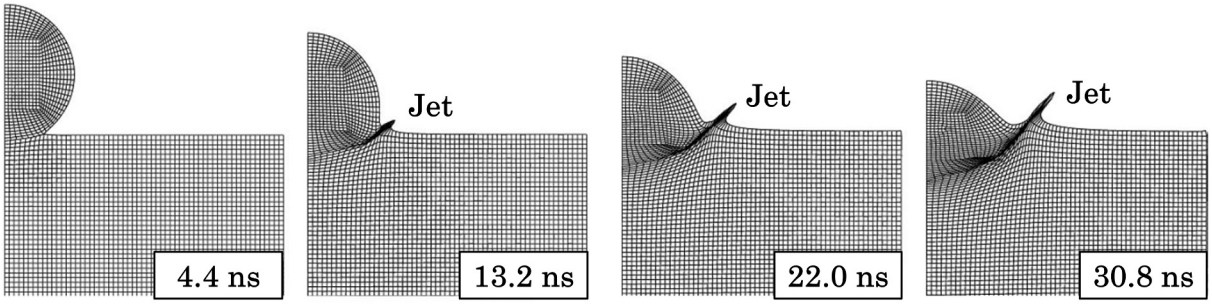

Fig. 3. Formation of jet for a 25 μm Cu particle impacting Cu substrate with an impact velocity of 550 m/s. Particle and substrate are at room temperature (295 K). Contact time are represented. The impact was simulated using the axisymmetric Lagrangian method in Abaqus FEA. Image adapted from [103].

methods rely on the three-dimensional strain distribution during a destructive measurement, whereas X-ray and neutron diffraction techniques rely on the interatomic spacing of selected crystalline peaks to measure residual stress [55,76,79,89].

The verification of a finite element (FE) simulation of residual stress, therefore, requires a comprehensive understanding of the nature of residual stress measured in the experimental and modelling results. Hence, residual stresses in the cold sprayed coating can be measured using numerical simulations [57,88]. The common methods used for residual stress modelling are temperature-displacement coupled Lagrangian, Eulerian and Coupled Eulerian-Lagrangian methods [18,29,47,96]. Commonly used commercial software for modelling residual stress in CS coatings include Abaqus FEA owned by Dassault Systems Simulia (Johnston, RI, USA) and Ansys/LS-DYNA (Canonsburg, PA, USA).

Table 3 shows numerical models that have studied residual stresses in cold sprayed coatings. Table 4 summarises experiments that have measured residual stresses in cold sprayed coatings. Tables 3 and 4 will be discussed further in Sections 5.1 and 5.2 respectively.

1.5. Prior review documentation

There are limited review papers on the numerical modelling of cold spray impact. Wen Ya Li et al. [45] summarises the effect of impact velocity, impact angle, pre-heating and prediction of critical velocity. Wen Ya Li et al. [29] also summarise numerical models using the Eulerian method and mention residual stresses. Review papers, summarised in Table 5, address the bonding behaviour [9,97,98], the effect of process parameters [5,7,99,100], particle deformation [6,7,45], and residual stresses [29,101,102] in cold sprayed coatings.

This current review addresses particle impact numerical modelling in association with residual stresses. This work summarises numerical methods for modelling particle impact and residual stresses; thereby providing deep insights into the strategies for modelling of residual stresses.

2. Particle deformation and bonding mechanisms

There have been several theories for the bonding mechanism in cold sprayed coatings, but adiabatic shear instability (ASI) is the theory agreed upon by a majority of researchers [6,7,9,15,29,45,97–99,101,103]. ASI is caused when a particle travels with or above its critical velocity and impacts the substrate. Critical velocity refers to the particle impact velocity above which the particle bonds to the substrate. The critical velocity differs with materials, particle size, pre-heat temperatures and impact angle [45]. ASI was first proposed by Assadi et al. [15] through their numerical and experimental work as being responsible for the bonding of cold sprayed coatings. This was confirmed by Grujicic et al. [103] and since then similar studies [13,25,27–29,45] have been exploited to predict critical velocities for different material combinations. However, it was proposed by Hassani et al [18] that hydrodynamic plasticity is the reason for bonding and not ASI [21,22].

When a particle impacts the substrate with or above its critical velocity, a pressure field is generated and propagates within the particle and substrate at their point of contact. The pressure field causes a shear load that pushes the material in the horizontal direction, and this causes

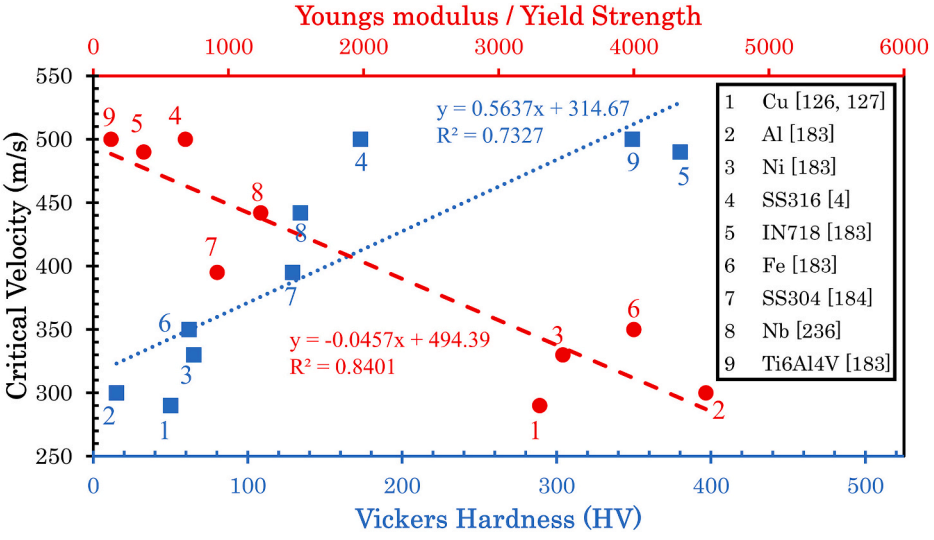

Fig. 4. The relation between critical velocity, Vickers Hardness, ratio of Young's modulus and yield strength for some of the commonly used materials in cold spray coatings (Data is obtained from papers in Table 2 and Hardness data from databases such as Azom and Matweb [248–256]).

localized shear straining. Under critical conditions, the shear loading leads to an ASI where thermal softening dominates over local strain and strain rate hardening [98,103,104]. ASI causes the material to flow in a viscous manner outward and causes the jet formation that is typical of cold sprayed coatings. Fig. 3 shows the jet formation in the finite element simulation performed by Grujicic et al. [103]. The onset of ASI is used to predict the critical velocity and other processing parameters.

Physical bonding, also termed as mechanical bonding, and metallurgical bonding has been suggested as mechanisms that enhance coating adhesion to the substrate [9]. Hence, critical velocity is an important parameter that has also been explored to investigate bonding. For example, Fig. 4 compiles the critical velocities of different materials plotted against the Vickers hardness of the CS coating. Note that each data point represents identical particle and substrate materials; i.e., spraying particles of chemistry 'A' against an 'A' substrate. It is seen that there is a linear relationship between the critical velocity and Vickers hardness. The Young's modulus and yield strength ratio display a linear relation with the critical velocity, which shows that the critical velocity must be higher to obtain successful bonding in harder materials and vice versa. The Young's modulus/yield strength ratio is plotted to view the elastic to plastic transition in metals and alloys. Materials with a lower Young's modulus and yield strength ratio, such as Ti-6Al-4V, IN718 and SS316, require higher impact velocities for bonding. This is due to the elastic to plastic transition that is required for bonding between the coating and substrate, which occurs at higher velocities for these materials.

Table 6 represents the mechanical and thermal properties of the materials being studied. It is seen that there is a notable relation between the thermal properties and critical velocity. High critical velocities are associated with materials of low thermal diffusivity; noting that thermal diffusivity is thermal conductivity divided by density and specific heat capacity. This velocity-thermal diffusivity relationship is related to the assumption of ASI since a particle impacting a material with high diffusivity will attain thermal instability quicker than for materials of lower diffusivity. Such correlations can benefit industrial outcomes and further improvements to understanding CS formation mechanisms include dissimilar material combinations, pre-heating and particle size affects.

3. Material properties

3.1. Elastic properties

The elastic behaviour of the particle and substrate can be predicted using temperature-dependent data of Young's modulus (E) with respect to Poisson's ratio (ν). The parameters E and ν must range from room temperature up to and above the melting point of the material. Some studies indicate that the temperature at the particle/substrate interface can reach above its melting point in the early stages of impact [27,81]. The intermolecular potential for solids at high temperature was developed by Gustav Mie (in 1903) [105]. The form of this relationship was extended by Gruneisen (in 1912) giving rise to the Mie-Gruneisen equation of state (EOS) that captures elastic behaviour [47]. EOS is a thermodynamic equation describing the characteristics of solids and fluids. The internal energy and pressure of the material can be characterized by the following relations [47,106]:

$$e(V,T) = e_{ref}(V) + e_T(V,T) \tag{1}$$

$$p(V,T) = p_{ref} + \frac{\Gamma(V)}{V} e_T(V,T) \tag{2}$$

where $V = {}^{1}/_{\rho}$ denotes the specific volume, T denotes the temperature, p is the pressure, e is the internal energy and Γ is the Gruneisen parameter that represents the thermal pressure from a set of vibrating atoms. The subscript *ref* refers to parameter at the reference temperature while (V, T) refers to the parameter at certain volume and temperature [47,96]. Combining Eqs. (1) and (2), the common form of the Mie-Gruneisen EOS is obtained [107]:

$$p - p_H = \frac{\Gamma}{V}(E_m - E_H) \tag{3}$$

where p_H and E_H are pressure and internal energy from the Hugoniot approximation. A 'Hugoniot' is a mathematical approximation from the pressure-volume ($p - V$) curve for materials under shock conditions [107]. E_m is internal energy per unit volume. The Mie-Gruneisen parameter Γ is defined as:

$$\Gamma = \Gamma_o \frac{\rho_o}{\rho} \tag{4}$$

where Γ_o is material constant and ρ_o is the reference density. E_H, Hugoniot energy, is given by:

$$E_H = \frac{p_H \eta}{2\rho_o} \tag{5}$$

where $\eta = 1 - (\rho/\rho_o)$ is the nominal volumetric compressive strain. Combining Eqs. (3)-(5), the Mie-Gruneisen EOS is rewritten as:

$$p = p_H\left(1 - \frac{\Gamma_o \eta}{2}\right) + \Gamma_o \rho_o E_m \tag{6}$$

The Mie-Gruneisen EOS is represented in the linear '$U_s - U_p$' Rankine-Hugoniot[1] form for numerical simulations [108]. The EOS without phase transitions and dynamic yielding, along with a linear fit assumption for shock velocity [47,96] as a function of particle velocity, is represented as [109]:

$$U_s = C_o + sU_p \tag{7}$$

where U_s represents the shock velocity, C_o is the isentropic speed of sound, U_p is the velocity of the particle, s is a dimensionless parameter that is related to the pressure derivative of the isentropic bulk modulus [96]. The $U_s - U_p$ result is given by:

$$p = \frac{\rho_o {C_o}^2}{(1 - s\eta)^2}\left(1 - \frac{\Gamma_o}{2}\right) + \Gamma_o \rho_o E_m \tag{8}$$

One disadvantage of the EOS method is for the need of reliable and complete data that includes thermal expansion effects [110,111]. Commercial software such as Abaqus FEA does not include EOS and coefficient of thermal expansion data as material properties, since it is logically impossible [37]. This issue can be overcome by using temperature-dependent elastic properties, such as Young's Modulus and Poisson's ratio, with CTE to study residual stresses. Additionally, the Mie-Gruneisen EOS must be used in conjunction with temperature-dependent viscosity to obtain comparable deformation behaviour of splats [47,96]. Even though EOS is capable of incorporating thermal expansion effects, it is difficult to obtain reliable and complete data. Hence, an alternative method that is often used models residual stresses as temperature-dependent elastic properties and CTE [29,57].

3.2. Plastic properties

The traditional plastic stress/strain values do not suffice for numerical modelling of high-velocity impacts because the material undergoes a broad range of strain rates and temperatures [112]. Most of the numerical simulations use models developed for specific materials.

[1] Rankine-Hugoniot represents the material response with an advancing shock wave and is based on the conservation of volume, energy and momentum. This form is used as a linear expression in simulations because the coefficient of the quadratic term is negligible.

3.2.1. Johnson-Cook plasticity (JC) model

The Johnson-Cook plasticity formulation is suitable to model the elastic-plastic response of the material [112,113]. The material behaviour at high strain rates and temperature is given by [113]:

$$\sigma = (A + B\varepsilon^{n})(1 + Cln\dot{\varepsilon}^{*})(1 - T^{*m}) \tag{9}$$

where ε is the equivalent plastic strain; $\dot{\varepsilon}^{*} = \dot{\varepsilon}/\dot{\varepsilon}_{o}$ is the dimensionless plastic strain rate where $\dot{\varepsilon}$ is strain rate and $\dot{\varepsilon}_{o}$ is reference strain rate; and T^{*} is homologous temperature. The five material constants are A = static yield strength, B = strain-hardening modulus, n = strain-hardening exponent, C = strain rate-sensitive coefficient, and m = thermal softening exponent [47].

3.2.2. Preston-Tonks-Wallace (PTW) model

The PTW model was developed for metallic plastic flow under explosive loading and high-velocity impacts [114]. The flow stress is defined as [115]:

$$\sigma = 2\left[\widehat{\tau}_{s} + \alpha ln\left[1 - \varphi exp\left(-\delta - \frac{\theta\varepsilon}{\alpha\varphi}\right)\right]\right]G_{p} \tag{10}$$

$$\alpha = \frac{s_{0} - \widehat{\tau}_{y}}{p_{PTW}}, \delta = \frac{\widehat{\tau}_{s} - \widehat{\tau}_{y}}{\alpha}, \varphi = exp(\delta) - 1 \tag{11}$$

where $\widehat{\tau}_{s}$ is the normalized work-hardening saturation stress, $\widehat{\tau}_{y}$ is the normalized yield stress, θ is strain hardening rate, ε is the equivalent plastic strain, s_{0} is the saturation stress at 0 K and p_{PTW} is the strain hardening constant.

3.2.3. Mechanical Threshold Stress model (MTS)

The Mechanical Threshold Stress model is a physics-based model suitable for high strain rate and high deformation simulations [116]. The plastic shear modulus (G_{p}) from Eq. (10) is defined by the MTS model [117]:

$$G_{p}(T) = G_{0} - \frac{D}{exp\left(\frac{T_{0}}{T}\right) - 1} \tag{12}$$

where G_{0} is the shear modulus at 0 K, D is a material constant, T_{0} is a temperature material constant and T is the material temperature [115].

The work-hardening saturation stress and yield stress are obtained from the equations below [115]:

$$\widehat{\tau}_{s} = max\left\{s_{0} - (s_{0} - s_{\infty})erf\left[\kappa\widehat{T}ln\left(\frac{\gamma\dot{\xi}}{\dot{\varepsilon}_{p}}\right)\right], s_{0}\left(\frac{\dot{\varepsilon}_{p}}{\gamma\dot{\zeta}}\right)^{\beta}\right\} \tag{13}$$

$$\widehat{\tau}_{y} = max\left\{y_{0} - (y_{0} - y_{\infty})erf\left[\kappa\widehat{T}ln\left(\frac{\gamma\dot{\xi}}{\dot{\varepsilon}_{p}}\right)\right], min\left\{y_{1}\left(\frac{\dot{\varepsilon}_{p}}{\gamma\dot{\zeta}}\right)^{y_{2}}, s_{0}\left(\frac{\dot{\varepsilon}_{p}}{\gamma\dot{\zeta}}\right)^{\beta}\right\}\right\} \tag{14}$$

where $\widehat{T} = T/T_{m}$, T_{m} is the melting temperature, s_{∞} is the saturation stress near the melting temperature, κ is the temperature dependence constant, γ is the strain rate dependence constant, $\dot{\varepsilon}_{p}$ is the plastic strain rate, β is the high strain rate exponent, y_{0} is the yield stress constant at 0 K, y_{∞} is the yield stress constant near melting temperature, y_{1} is the medium strain rate constant, y_{2} is the medium strain rate exponent. The unnamed parameter ($\dot{\zeta}$) in Eqs. (13) and (14) is given by [115]:

$$\dot{\zeta} = \frac{1}{2}\left(\frac{4\pi\rho}{3M}\right)^{\frac{1}{3}}\left(\frac{G_{p}(T)}{\rho}\right)^{\frac{1}{2}} \tag{15}$$

where M is the atomic mass.

PTW and MTS models were used by Cormier et al. [115] in commercial Abaqus FEA software. PTW and MTS parameters use the subroutine 'VUHARD' since they are not available within the user interface of Abaqus FEA. Few models use PTW and MTS, while the Johnson-Cook plasticity criteria is most widely applied.

3.2.4. Zerilli Armstrong (ZA) model

The Zerilli Armstrong (ZA) model can model the plastic behaviour of material [118]. ZA is a dislocation mechanics-based constitutive relation that describes flow stress of metals. A modified version of the ZA model can describe the flow stress at high temperatures [119,120]:

$$\sigma = (C_{1} + C_{2}\varepsilon^{n})exp(-((C_{3} + C_{4}T^{*})T^{*} + (C_{5} + C_{6}T^{*})ln\dot{\varepsilon}^{*})) \tag{16}$$

where ε_{p} is the equivalent plastic strain, $\dot{\varepsilon}^{*}$ is the equivalent plastic strain rate normalized with respect to the reference strain rate $\left(\dot{\varepsilon}_{p}/\dot{\varepsilon}_{0}\right)$; $T^{*} = T - T_{r}$, where T is the absolute temperature and T_{r} is the reference temperature. C_{1}, C_{2}, C_{3}, C_{4}, C_{5}, C_{6} and n are material constants.

Apart from elastic and elastic-plastic behaviour, other properties such as density; coefficient of thermal expansion; thermal conductivities of the solid and liquid; specific heat capacities of the solid and liquid; and latent heat must be used in the simulation. All the above-mentioned parameters, except latent heat, are temperature-dependent and values from room temperature to the melting point must be available.

4. Numerical methods

4.1. Lagrangian model

Most of the early models used a Lagrangian model for particle impact [3,4,13,27,28,32]. Normal impact models take advantage of the symmetrical nature of the impact and employ quarter [4] or axisymmetric models [27,32] to reduce computational time significantly. The Lagrangian method mostly uses hexahedral elements for meshing, with the mesh refined in the particle and closer to the substrate impact area to obtain comparable deformation behaviour and for mesh convergence. However, mathematical truncation errors are likely in the Lagrangian method due to severely distorted elements [32], which can be overcome by using Arbitrary Lagrangian-Eulerian (ALE) adaptive remeshing [32]. The ALE method requires an additional computational step where continuous remeshing, either arbitrary or in a pre-defined fashion, is used; which can increase the computational time [14,15,25,121–124]. Additionally, previously published sources cite that there are more drawbacks when using the ALE method [123]. For instance, unrealistic particle deformation at high speeds [121], a decrease in equivalent plastic strain with time [122], and underprediction of the particle/substrate interface temperature [123] are notable drawbacks reported in the literature. These drawbacks are highly affected by the frequency of the remeshing increment [121], interpolation errors during the remeshing [122], high strain gradients closer to the interface [122], and deviation of integration and material points during remeshing [123]. The contact interactions between splats also impose restrictions on ALE. The nodes within the contact zone cannot be automatically re-meshed since contact interactions override the ALE routine.

Another major disadvantage in the Lagrangian model is the severe distortion of the particle and substrate that causes the program to terminate above a certain impact velocity [3]. This impact velocity can be determined only when the user simulates the model. For the case of 20 μm Cu impacting a Cu substrate, Li et al. found that the program terminates due to excessive grid distortion above 500 m/s [3]. Temperature-dependent Young's modulus, Poisson's ratio, density, thermal conductivity and specific heat must be used in a dynamic explicit temperature-dependent module for particle analysis. The plasticity needs to be modelled using the Johnson-Cook plasticity model or other similar models due to the high strain rates on impact.

As mentioned, Li et al. performed impact of Cu particle (20 μm) on Cu substrate at an impact velocity of 500 m/s. It was concluded that the

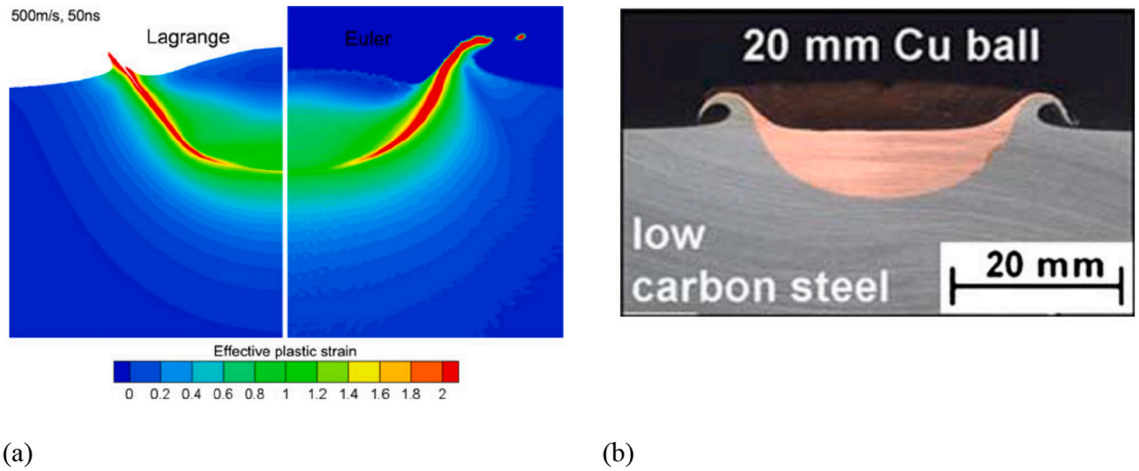

Fig. 5. (a) Contours of effective plastic strain for Lagrangian and Eulerian method [128], (b) Macroscopic picture for 20 mm Cu ball on low carbon steel [129].

maximum temperature and plastic strain was acting around the contact zone and not the initial impact area. The melting of the particle or substrate was not the bonding mechanism but bonding arose from ASI [3]. There was no heat transfer between the particle and substrate interface (adiabatic process), modelled after Grujicic et al. [103]. Doing so, caused the localization of shear and the impacting particle softens due to the heating which ultimately led to ASI. The numerical model was then run at different impact velocities. The velocity at which the ASI form is the critical velocity. The critical velocity for Cu particle (20 μm) impacting Cu substrate ranged from 298 to 356 m/s and depended on particle temperature and oxidizing conditions [13]. A study on velocity effects was also performed using Lagrangian and ALE methods. It was found that the meshing size affects the localized shear instability and the deformation using the ALE method was similar to the experimental observations [27].

Yildrim et al. [4] simulated material combinations of copper, titanium, 316 L steel and aluminum with different impact velocities using the Lagrangian method. The model was used to study the bonding between the particle and substrate bonding of different materials bonding using a cohesive zone model. The effective interfacial cohesive strength parameter was varied to study the bonding behaviour. The numerical model deepened the understanding of bonding and showed the influence of interfacial strength on critical velocity. The critical velocity estimated is lower for high cohesive strength showing that improving surface conditions by cleaning the oxides or contaminants improves the bonding. This method can probably be used to study the effect of surface preparation, although it can be difficult to estimate the cohesive strength for different surface preparations.

Yin et al. [28] studied two 20 μm Cu particles impacting a Cu substrate in parallel and sequential configurations with respect to spray distance. Additionally, a sequential impact of three particles and multiple impacts involving five particles examined the formation of porosity. Although the deformation in the Lagrangian method was not comparable to experimental observations due to the distorted element in the jet, it provided an understanding of particle-particle interaction and porosity formation. The porosity formation during cold spraying showed that due to the nature of the deformation of the particles, the coating is less dense on the surface when compared to the inside of the coating. This observation also agreed with experimental studies performed by Li et al [125].

King et al. used Lagrangian axisymmetric with ALE remeshing for copper particles impacting commercially pure and 7050 aluminum [32]. The numerical model was used to understand the deformation and adhesion mechanism. Although there were earlier works using ALE remeshing [25,27], this work was unique in terms of finding if the bonding is due to interfacial melting and also performed experiments to confirm this. And from the numerical and experimental study, it was confirmed that there can be the presence of interfacial melting.

4.2. Eulerian model

The Eulerian method is suitable to model high deformation processes, which makes it suitable for CS. The deformation behaviour of particle impact for the Eulerian method is comparable to experimental observations [2,3,29,57,126,127]. Li et al. first proposed to use the Eulerian model for CS impact to overcome the elemental distortion experienced in the Lagrangian method [27]. In the Eulerian method, the mesh consists of 3 regions- particle or particles, the substrate and void. Commercial software such as Abaqus FEA, allows the Eulerian method to model one part and segments can be partitioned for other sections. Different materials can be assigned to the regions using the multi-material mode within Abaqus FEA [37]. The material within the mesh can flow freely, which makes it suitable to model severe plastic deformation in CS [29]. The contact between the particle and substrate cannot be varied because the software (Abaqus FEA) incorporates default contact interactions [37]. The Eulerian method does not allow 2D models; however this is overcome by using a single element in the thickness direction, referred to as a Eulerian slice, to reduce computational costs. The width and height of the substrate are usually taken as five times larger than the particle diameter [29,45]. The bulk of the CS impact modelling work using the Eulerian method has been carried out by Li et al. [2,3,29,57,126,127].

Li et al. [2] used a Eulerian slice to model the impact of Cu (351 m/s), Ni (374 m/s) and Al (514 m/s) particles on Cu, Ni and Al substrates at a mesh size of 0.2 μm. The model aided understanding of the experiments that studied interface behaviour. The model does not make significant advances compared to the previous models published, however the model is used to study the interfacial temperature change and compared to experimental observations. It was found that the interfacial temperature increased to a high value but lower than the melting point. This was found to be closer to recrystallisation temperature and it was concluded that recrystallisation occurs.

A similar model by Yu et al. [126] used the Eulerian slice model to study the impact of Cu particles (20 μm) on a Cu substrate at velocities from 200 to 700 m/s to determine the critical velocity at which jetting begins. One of the applications of obtaining critical velocity from a numerical model previously developed by the research group [2,3,29,57,126,127] was demonstrated in this work. The critical velocity for Cu/Cu system was found to be around 290 m/s and good deposition was observed in the range of 290 to 400 m/s, above this splashing was found to occur. In another work, Yu et al. [127] used the previously established model to study the effect of preheating on the

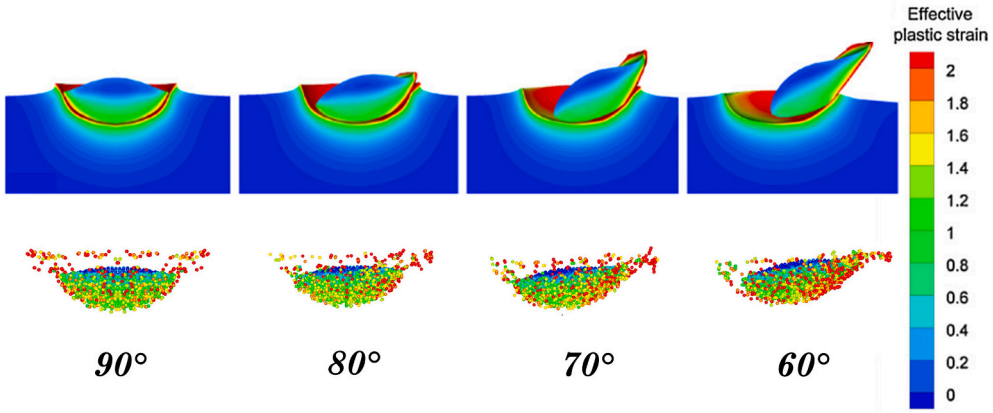

Fig. 6. Numerical results for copper particle impacting copper substrate for different impact angle modelled using SPH method (top) and Lagrangian method (bottom) [39].

particle impact behaviour. It was concluded that preheating helped to form a uniform deformation pattern that was beneficial in increasing the effective contact area between the particle and substrate.

In addition, Li et al. [57] modelled the impact of a Cu particle (20 μm) impacting Cu and Al substrates using the Eulerian slice model with heat transfer to study residual stresses. This was a significant advancement in cold spray modelling. The period of the simulation was set at 1 μs to study the residual stresses with a mesh resolution of 0.2 μm. As well, multiple particle impact to obtain a thicker coating was implemented to compare with experimental residual stress profiles. Li et al. [29] published a review paper on the Eulerian method to model cold spray impact. The effect of mesh resolution, impact velocity, pre-heating and oxide film was summarised.

Fig. 5 compares Lagrangian and Eulerian simulations with an experimental macro-image [128,129]. It is seen that the Eulerian method of modelling provides visually comparable results with the experimental deformation. The distribution of the effective plastic strain is similar for the Lagrangian and Eulerian methods, which has been the driving force to incorporate the Eulerian method for CS impact modelling. Drawbacks of the Eulerian model are (i) the requirement of a fine mesh that increases computational time, (ii) the inter-mixing of the particle and substrate that renders it difficult to distinguish the particle/substrate interface [128], and (iii) coalescence of the particles in a multiple particle method [46].

The size of the mesh used in the Eulerian model could also influence the simulation results [29]. The literature [27,29,130] indicates that the shape of the deformed particle and the numerical results of plastic strain and temperature, derived from the simulation, were influenced by the mesh size. The predicted plastic strain and temperature for coarser mesh sizes were lower than the fine mesh as the results are element-averaged similar to the Eulerian method [29,130]. The finer mesh sizes lead to increased computational time. It was found that a mesh size of 1/100 dp (dp is the particle diameter) yields desirable results [29].

Several researchers have provided modified formulations to solve the coalescence issue in droplet or bubble modelling [131–133]. Although the formulations proposed are for droplet/bubble modelling they have been reported here as the method is probably transferrable to CS particle impact modelling. The techniques used for droplet/bubble modelling are front tracking, level set, marker particle, shock capturing, VOF, and Lattice-Boltzmann [134,135]. Mühlbauer et al. [134] provides a comprehensive review for the model formulation. Some of the advantages and disadvantages of selected methods will be highlighted here.

Front tracking is a robust and accurate method but requires mapping of the interface mesh onto the Eulerian mesh and dynamic remeshing, which increases the computational time. The level set method is conceptually simple and easy to implement, however there are issues with accuracy and mass conservation. The marker particle method has high accuracy and is robust but is computationally expensive and requires re-distribution of the marker particles [134].

Balcázar et al. [132] used a multiple marker level set method to prevent coalescence of droplets/bubbles. The model agreed well with the experimental results. Modified versions of level set formulations have been proposed by Chang et al. [131] and He et al. [133]. The results of the modified versions agree with experimental or previously established numerical methods. Although the numerical methods to prevent coalescence are used in droplet/bubble modelling it is not used in CS impact modelling as commercial software is primarily used for modelling. Incorporating formulations to prevent coalescence can be explored further by researchers working on numerical modelling simulations.

4.3. Smoothed Particle Hydrodynamics (SPH)

Smoothed Particle Hydrodynamics is a non-mesh based Lagrangian method that was initially developed for astrophysics problems and then applied to engineering problems. It can undergo severe deformation, which attracted early publications that modelled high-velocity impacts. The mesh is discretized into smaller elements. Each element is assigned characteristics of the material [26,38,39,136] with the precise size decided by the mesh resolution [39].

Manap et al. performed simulations of a Cu particle impacting steel substrate at various velocities to determine the bonding mechanism. It was found that the rebounding distance was minimal, implying good bonding, for velocities between 450 and 1000 m/s [40]. Manap et al. studied the effect of Al and Ti particles (25 μm) impacting Al, Ti and mild steel substrates at velocities of 700 to 800 m/s. The elastic properties were modelled using Mie–Gruneisen EOS while plastic properties were modelled using the Johnson-Cook plasticity model. It was concluded that the SPH method can be used to optimize spray parameters and to predict coating quality [136]. Another study of the rebound phenomenon by Manap et al. employed SPH for a 25 μm Al particle impacting an Al substrate at 450, 700 and 1050 m/s [41]. The work performed by Manap et al. were based on a similar SPH formulation where the interaction was considered using a cohesive zone model [38,40,41,136]. The only notable progress made among the different papers were applying the model to find the critical velocity and the velocity range for deposition while comparing it with experimental results.

Gnanasekaran et al. [26] carried out single and multiple particle impact using 2D and 3D SPH models for Cu/Cu configuration. The effect of particle diameter and impact angle was studied using an in-house code. It was concluded that the bonding was effective for impact angles between 80° and 90°. Increasing particle diameter caused the kinetic energy to increase, which resulted in an early onset of thermal softening. The notable progress made in this work is that the failure

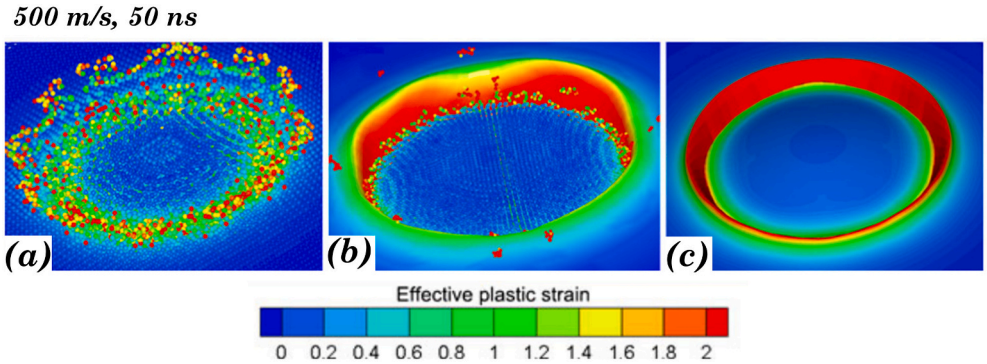

Fig. 7. Effective plastic strain distribution for Cu/Cu simulations using (a) SPH model, (b) SPH (particle) and Lagrangian (substrate), (c) Lagrangian model [128].

model was included, and the code was developed in-house. Using an in-house code can give the researcher freedom and flexibility to modify the formulation. This is an attractive future research direction as SPH method has certain drawbacks and ability to modify SPH formulation can probably help in overcoming these drawbacks.

Li et al. studied impact angle, particle diameter and mesh resolution used in SPH simulation for Cu/Cu configuration at a velocity of 500 m/s. The size of the SPH particles had minimal effect on the deformation and compression ratio; thereby making it suitable for CS simulation [39]. Fig. 6 compares Lagrangian and SPH simulations for Cu/Cu with respect to impact angle [39]. For normal impact, the maximum plastic deformation acts in the region around the impact zone and jetting forms. On decreasing the incident angle, the plastic deformation becomes non-symmetrical and plastic strain increases on the right-hand side. There is a decrease in the contact area with the decrease in incident angle and this was also observed in the experimental studies performed. The deformation modelled by SPH is comparable to that modelled by Lagrangian with the exception of some splashing in the jet region [39].

A comprehensive comparison of Lagrangian, Eulerian and SPH methods by Yin et al. [128] found that SPH and Eulerian models were suitable for simulation of the CS process rather than the Lagrangian method due to problems of rebound and mesh continuity for the latter. SPH and Eulerian deformation patterns were comparable to the experimental observations. Fig. 7 compares models for pure SPH, SPH-Lagrangian and pure Lagrangian methods obtained from Yin et al. [128]. The pure SPH model undergoes significant splashing in the jetting region and undergoes high plastic deformation. The combination of SPH for the particle and Lagrangian for the substrate, (Fig. 7b), is comparable to a pure Lagrangian approach (Fig. 7c). The particles adhere well to the substrate without undergoing the rebound phenomenon [128].

Although the SPH method is suitable for high deformation simulations, there are limiting drawbacks [137]. The results from SPH are less accurate when compared to other methods (e.g., Lagrangian or Coupled Eulerian-Lagrangian) when there is no severe deformation. SPH requires a fine mesh to obtain comparable results with other methods and this increases the computational time. The CEL method is more suitable and provides accurate results for models involving high deformation (see Section 4.4). SPH is viable for simulations when other methods are (i) computationally expensive, or (ii) unable to model extreme levels of deformation. This is evident from the number of papers published using different methods for CS modelling (Fig. 2). The number of models employing SPH technique is much lower than the other methods.

Tensile stability is another limitation of SPH, where the particle motion becomes unstable under a tensile stress state. The instability arises from the interpolation technique of SPH and causes particle jetting, particle fragmentation at the jetting region, and particle connectivity issues. This behaviour of the SPH method is evident from Fig. 6 and Fig. 7. It is seen that the SPH particle undergoes fragmentation and jetting prediction by SPH is greater than by other methods. Higher order kernel functions (e.g., quadratic, cubic, or quintic mathematical constructs) can obtain more accurate and stable results, but at the expense of increased computational time [137].

The contact interaction between the particle and substrate also requires consideration. The default contact interactions between the particle and substrate may not be captured well by the SPH method. The poor contact interactions arise due to pseudo-particles, which are discretized elements of the mesh that are not part of the default contact interactions and are similar to point mass. There are also limitations to the contact thickness requirements and only default or reasonable non-zero contact thickness must be specified. Additionally, higher frictional values should not be used in the contact interaction of the SPH particles and contact cannot be defined between a Eulerian mesh and SPH domain. The contact interaction is an important feature in CS modelling and all the contact limitations of SPH method must be considered [137].

The computational time for SPH is higher than other methods and requires a finer mesh for accurate results. Using parallel computer processing will reduce computational time for multiple particle impact. However, there are numerical limitations when parallelisation is considered for SPH. The minimum number of pseudo-particles is 10,000 to have good scalability. Certain results associated with SPH particles, such as a history output in Abaqus FEA, are not supported. Contact issues can be encountered. For instance, slave nodes cannot be assigned to the SPH domain and the general domain (if used) must be assigned to the entire SPH domain. The computational process also becomes intensive as dynamic load balancing cannot be used and leads to a significant increase in memory usage [137].

4.4. Coupled Eulerian-Lagrangian (CEL)

Coupled Eulerian-Lagrangian (CEL) uses Eulerian and Lagrangian formulations and is more effective than Eulerian alone when contact interactions between the particle and substrate must be varied since Eulerian employs default contact interactions [37]. CEL method has been used to model thermal spray impact of yttrium-stabilized zirconia (YSZ) particles on a stainless steel substrate [47,96] as well as the impact of CS particles [31,138–141].

Bolelli et al. modelled a quarter of the particle-substrate domain of 30 μm particle WC-Co (12% and 17%) impacting on a substrate of the same material. The particle before impact was designed with pores of 3 μm diameter at a spacing of 8 μm. The impact velocity varied from 400 to 700 m/s while the particle temperature varied from 700 to 1000 K with the substrate at a constant temperature of 373 K. The simulation runs were carried out with and without damage initiation criteria and the results compared with experimental SEM images [139]. It was found that the model with the damage initiation criteria was comparable to the experiment. Increasing the impact velocity promotes the particle spreading and increases the bonding to the substrate, but also causes fragmentation and particle rebound.

Jing et al. used Abaqus FEA to simulate Cu and Al particles (25 μm) impacting on Cu and Al substrates at 300 K using Lagrangian, ALE and

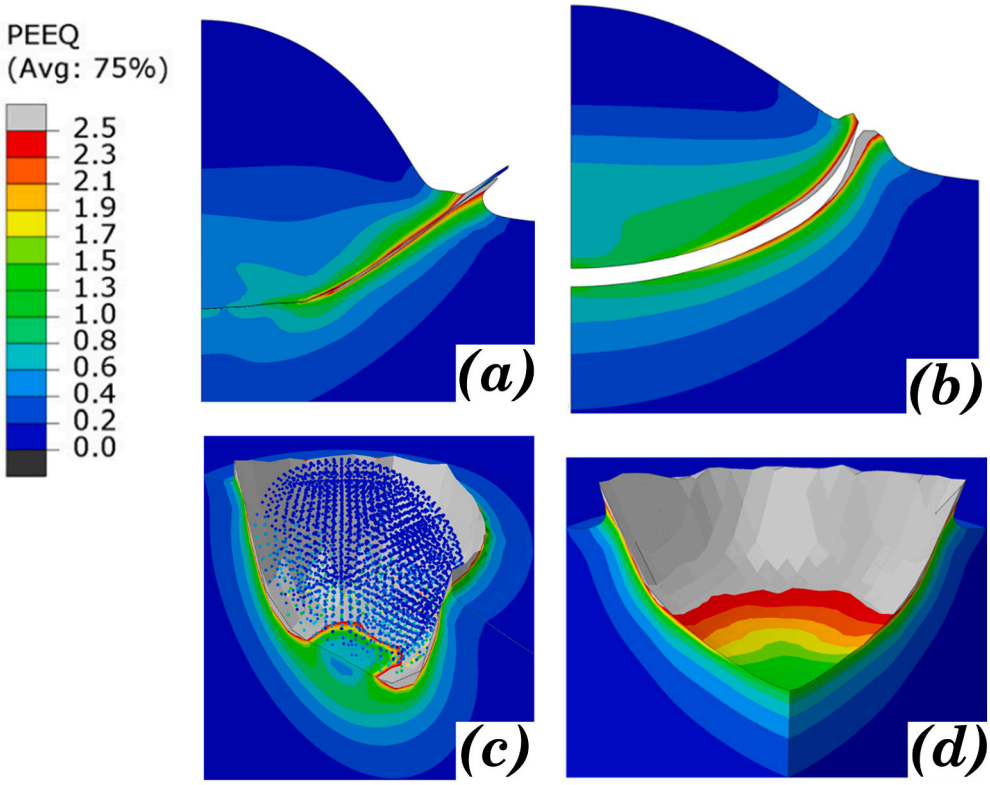

Fig. 8. Equivalent plastic strain contour for (a) Lagrangian, (b) ALE, (c) SPH-Lagrangian and (d) CEL for Al/Al with impact velocity of 700 m/s [33].

CEL methods. The particle velocity varied from 400 to 700 m/s and the particle temperature from 300 to 700 K. Multiple impacts were studied using the CEL method by using a quarter model. It was concluded that the Eulerian method was more effective in estimating porosity and process parameters [31].

Xie et al. used 2D Lagrangian, 3D SPH, ALE and 3D CEL models for Al and Cu under a full factorial design of experiments with the variables of particle diameter (20 and 25 μm), impact velocity (500–840 m/s) and temperature (300–873 K). The coefficient of friction was varied in the CEL model and did not have a significant effect on the plastic strain and temperature [33]. Fig. 8 compares the CEL, SPH-Lagrangian, ALE and Lagrangian models for Al particles on an Al substrate at an impact velocity of 700 m/s [33]. The Lagrangian model (Fig. 8a) was aborted due to excessive element distortion, which is a drawback of this method. The Arbitrary Lagrangian-Eulerian (ALE) model (Fig. 8b) can undergo excessive mesh distortion. The lack of adhesion was identified as gaps between the particle and substrate and indicated rebounding particles. The SPH-Lagrangian model (Fig. 8c) can simulate high deformation where the particle adheres to the Lagrangian substrate. However, the particle undergoes excessive plastic deformation that is different from the Lagrangian and ALE model. It was concluded that the excessive plastic deformation is a limitation of the SPH model within the Abaqus FEA software since thermo-mechanical effects are not considered correctly.

Hassani et al. simulated impact of Cu particle on a Cu substrate using Lagrangian and CEL methods. The impact velocity was 550 m/s and the substrate temperature was 298 K. The main conclusion was that the jetting phenomenon was pressure-driven and not due to ASI. This was concluded by removing the thermal softening exponent during the simulation in the Johnson-Cook model [18]. Some of the drawbacks of CEL are similar to that of the Eulerian method (refer to Section 4.2). The mesh size and particle coalescence in multiple particles are drawbacks. A mesh size study was implemented by Hassani et al. [18] and found its influence on particle deformation and numerical results. The mesh resolution study was carried until a mesh size of 1/80 dp (dp is particle diameter), which is closer to the mesh size of 1/100 dp found by Li et al. for pure Eulerian method [29].

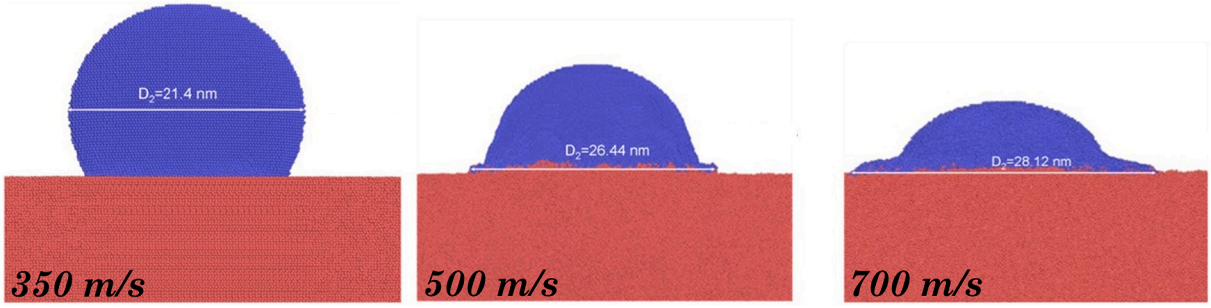

Fig. 9. Molecular Dynamics simulation for 20 nm Ti particle impacting Ti substrate for different initial velocities [232].

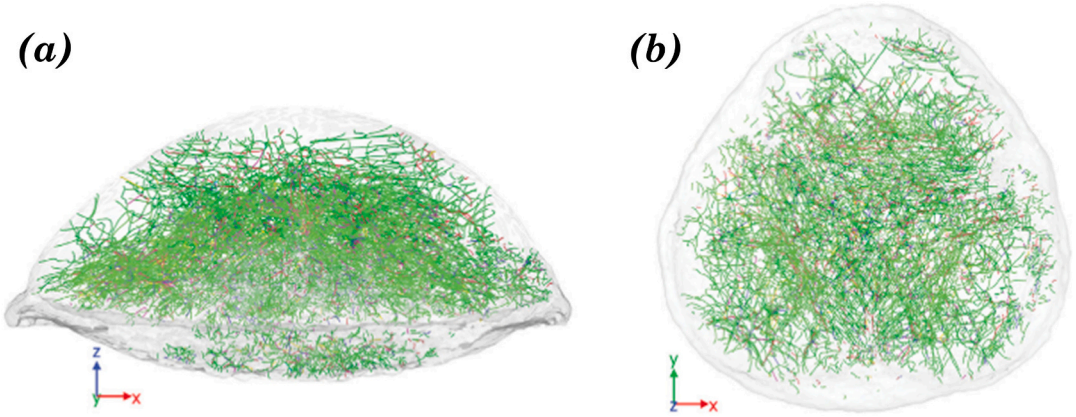

Fig. 10. Dislocation network of 40 nm Cu particle impacting Cu substrate after 25 ps (a) side view, (b) top view using Molecular Dynamics [30].

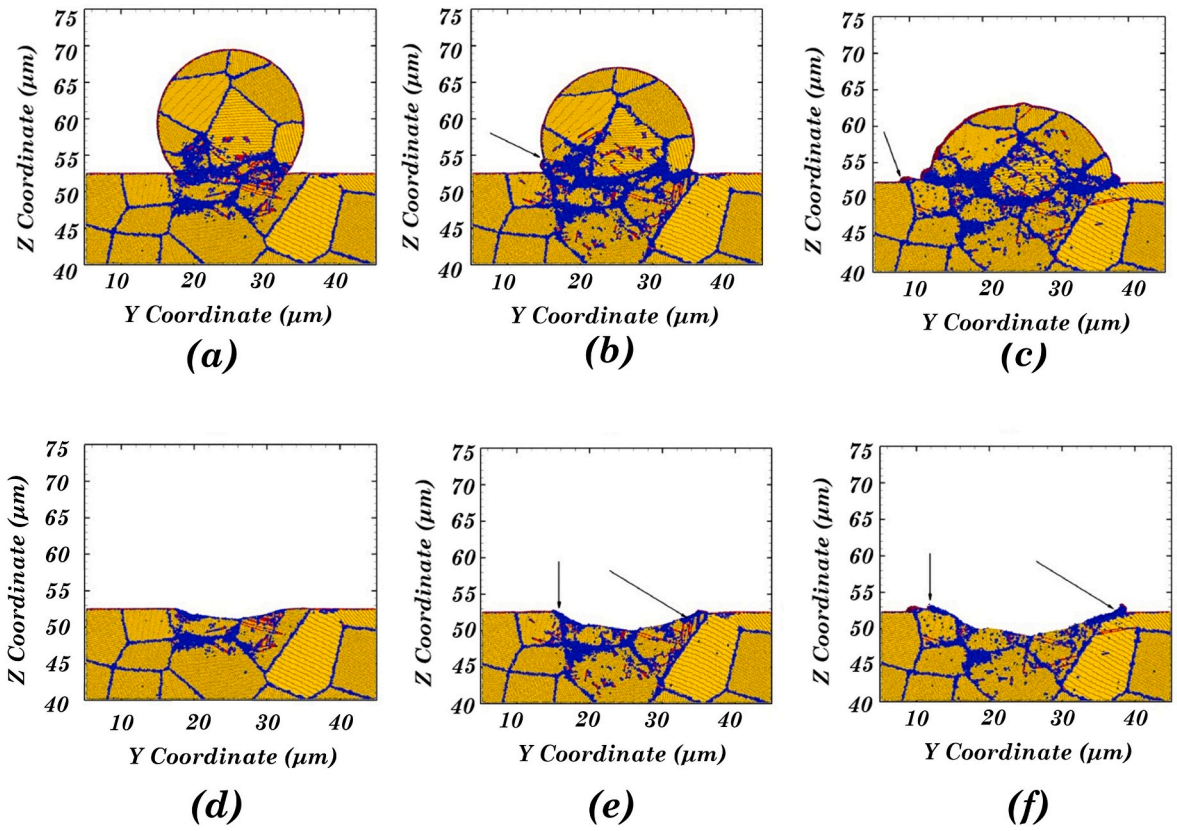

Fig. 11. Molecular Dynamics simulation showing microstructure for an impact velocity of 1300 m/s of 20 μm Al particle impacting Al substrate. The colours indicate the phases: yellow – fcc, red – hcp, magenta – surface and blue – disordered. The arrows indicate the formation of jets [42].

4.5. Molecular dynamics (MD)

Molecular dynamics (MD) simulations can capture the interactions of atoms or molecules using the classical equations of motion [142,143]. Defect formation, grain boundaries, structural transformation, radiation, elastic and plastic mechanical properties, friction and shockwaves are some fields where MD has been applied [144,145]. MD simulations are used to model CS impact to study microscopic mechanisms in the coating and substrate system [146].

Rahmati et al. simulated the impact of Cu particles (5 to 40 nm) on a Cu substrate using LAMMPS code (Large-scale Atomic/Molecular Massively Parallel Simulator) developed by Sandia National Laboratories. The initial pre-heating temperature for the particle and substrate was 300 K with a particle impact velocity of 1000 m/s. The nucleation and gliding of dislocations were reported to form at the point of impact and then spread throughout the particle as it deforms. The Von mises stress and shear stress was also reported. Additionally, the temperature in the jet zone reached about 1000 K [30]. The particle penetration into the substrate and flattening increases with an increase in the impact velocity, as observed in Fig. 9. MD simulations allow the study of nucleation, dislocation glide and microstructural changes. Fig. 10 shows the dislocation network for a particle of 40 nm at an impact velocity of 1000 m/s [30]. The changes in the microstructure during and post-impact deformations can also be studied using a variant of MD known as QCGD (quasi-coarse-grained dynamics), Fig. 11.

Joshi et al. [142,143] reported the impact of Cu particles (0.5 to 2

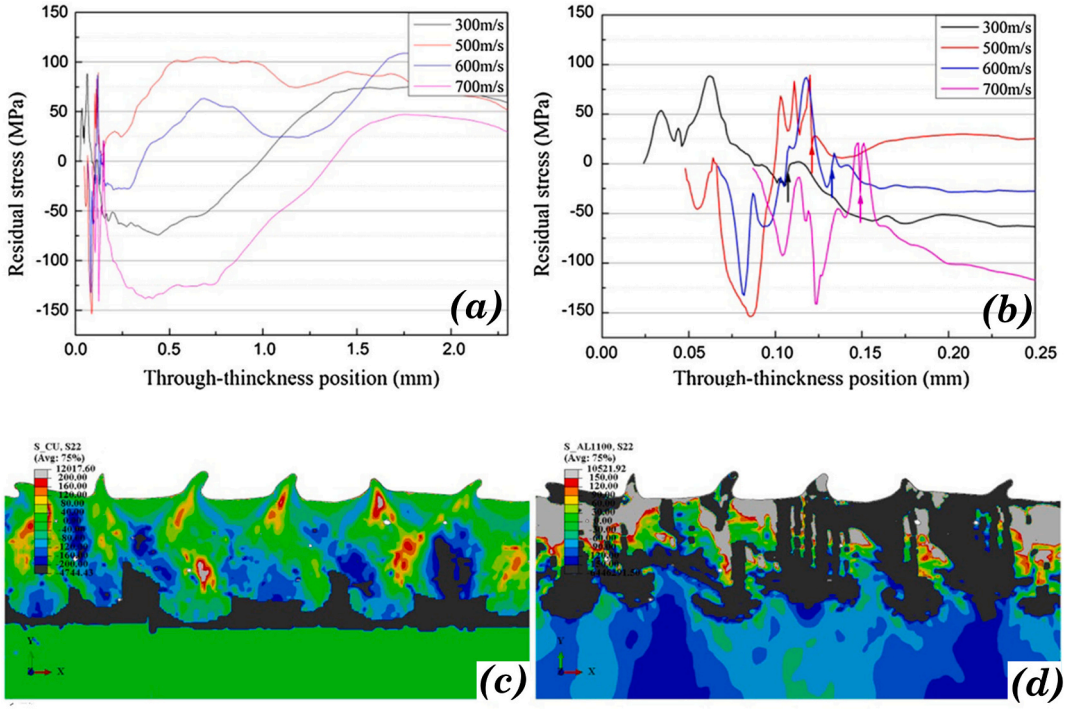

Fig. 12. (a) Through thickness residual stress distribution for Cu/Al configuration, (b) Magnified stress profile of (a) closer to the coating/substrate interface, (c) Residual stress contour acting on Cu coating, (d) Residual stress contour acting on Al substrate for an impact velocity of 700 m/s [57].

nm) on a Cu substrate using LAMMPS code. The initial temperature of the particle and substrate was 300 K. The impact velocity varied from 300 to 850 m/s while the impact angle was from 60° to 90°. The adiabatic softening, ASI and interfacial jet formation at high velocities resulted in a uniform coating. It was concluded that the best deposit was achieved for an impact velocity of 700 m/s, a particle size of 2 nm and an impact angle of 90°. However, as mentioned in a previous section, the particle sizes are in the range of nanometres (nm), which are difficult to relate to CS practice.

Gao et al. simulated impact of a Cu particle on Cu and Ni substrates for velocities of 300, 500, 700, 900 and 1100 m/s and particle temperatures of 300, 400 and 500 K. The size of the particle; impact velocity; and the substrate hardness and temperature affect the bonding strength of the deposit [147]. Gao et al. simulated the impact of Au particles on an Au substrate using the MD method. The size of the particle was defined in terms of the number of atoms and was fixed at 152, 276 and 420 atoms. The impact velocity (300 to 1000 m/s) and particle temperature (300, 400 and 600 K) were varied. Higher impact velocity and larger particle size result in stronger bonding between the particle and substrate due to higher kinetic energy [146]. A notable observation made is that better contact between the particle and substrate is directly translated to a better bonding strength [39,146,147]. However, this observation from the numerical models and has not been validated with experimental work.

Malama et al. reported a study of Ni and Ti particles impacting a Ti substrate. The impact velocity, temperature and particle diameter were varied. The particle deposition increases with an increase in impact velocity, deposition temperature and particle diameter [145]. Goel et al. [148] simulated the impact of copper particles on the copper substrate using the LAMMPS code. The topography, depth of penetration, shape of the splat and flattening ratio depended on the impact velocity. It was also found that the Von Mises stress varied with impact velocities above 500 K, while it was independent of impact velocity below 500 K.

5. Residual stresses

5.1. Numerical modelling of residual stresses

Although there are many publications on the topic of cold spray and particle modelling, there are limited studies on the residual stresses formed due to cold spraying. This Section discusses notable publications that refer to residual stresses in thermal spraying since this knowledge base can be extended to modelling residual stresses in CS. The numerical models that encompass residual stresses from Table 3 are summarised in this Section.

Li et al. [57] used the Eulerian slice method (Abaqus FEA) to model residual stresses for Cu/Cu and Cu/Al combinations for single and multiple particles. The maximum residual stress and plastic deformation acted in the region surrounding the particle and not at the initial point of impact. The combination of material, impact velocity and pre-heating temperature affect significantly the state of the final residual stress. The effect of temperature was more significant for the Cu/Al (ID3b) system than for the Cu/Cu (ID3a) couple. Fig. 12 shows the through-thickness residual stress and residual stress contour obtained from FE simulation for Cu/Al obtained from Li et al. [57].

Song et al. [88] modelled the residual stresses formed when a single Ti6Al4V particle impacts a Ti6Al4V substrate. The 3D Lagrangian model with Johnson-Cook plasticity and dynamic failure model (Abaqus FEA) was used to predict the residual stress profile. The stresses at the microscopic level (ID2a and ID2b) exhibited much higher stress range than the macroscopic level (ID2c) obtained from [149]. The compressive stresses were higher with increasing impact velocity from 700 m/s (ID2a) to 800 m/s (ID2b) in the direction parallel to the particle-substrate interface. The residual stress profile (microscopic level) from the numerical model was comparable with experimental measurements from Focused Ion Beam-Direct Image Correlation.

The numerical study of impact angle on residual stress was carried out by Benenati et al. [150]. The model used the 2D Lagrangian model (ANSYS-AUTODYN) to study the effect of impact angle and material combination on residual stresses. The residual stresses were higher and

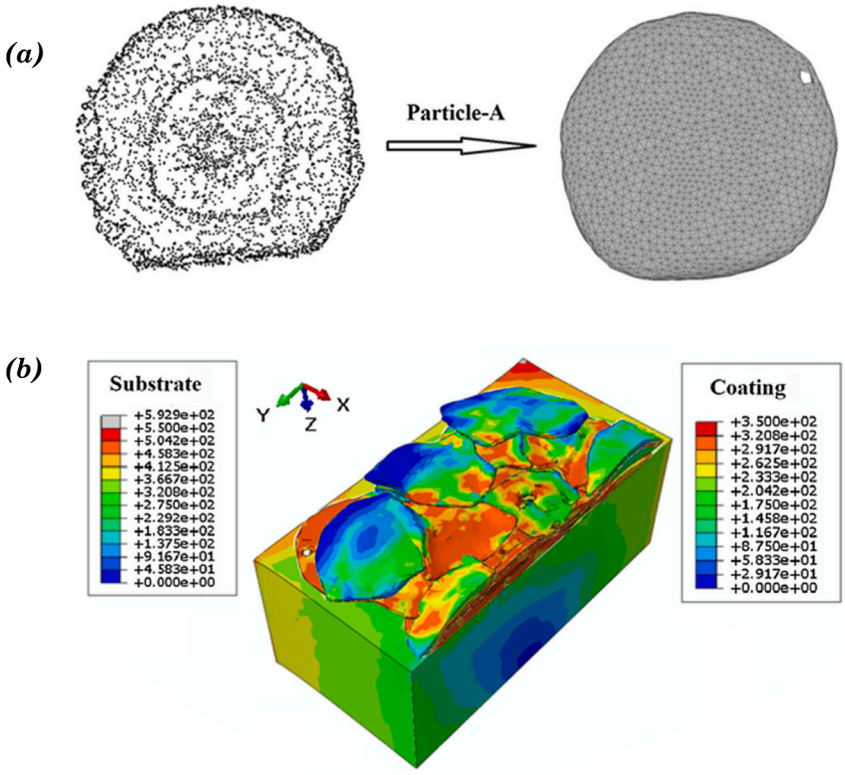

Fig. 13. (a) Conversion of the point cloud to FE mesh, (b) Residual stresses acting in YSZ coating and SS301 substrate [161].

compressive in nature with the increase in incident angle (angle between incident velocity and substrate surface). It was verified, unsurprisingly, that the density and yield stress of the coating material affected the residual stress state. The residual stresses for Al and Cu coating on Al, Cu and Ti substrates had lower values (ID5a to ID5f). While the residual stresses for Ti coatings were of higher magnitudes (ID5g to ID5i). It has been observed that there is a scarcity of published work on the effect of impact angle on residual stresses. This can be a probable future research direction to gain more insights as the impact angle is not going to be in normal direction in all the applications. And from the study done by Benenati et al., it is seen that the nature and magnitude of residual stresses can vary with impact angle.

Saleh et al. [81] studied the residual stresses and bonding mechanism for multiple particles impacting a substrate of AA-6061-T6. It was determined that the bonding between the particles was thermo-metallurgical due to "micro-welding" that occurred in the thin molten rim forming around each particle. It was agreed that the residual stress state is a result of dynamic strengthening and thermal softening of the alloy and the peening effect. The numerical stress profile (ID1) agreed with neutron diffraction experiments and theoretical (Tsui-Clyne) results [151]. Lin et al. [152] studied an AA6061 coating on an AA6061 substrate using single and multiple particle impacts. The bonding between coating and substrate affects the local residual stresses (ID6). The balance between peening stresses, which cause compressive stresses, and relaxation that arises during bonding leads to the final residual stress state.

Shayegan et al. [153] studied Al coating on a magnesium substrate (AZ31B) using single and multiple particle impacts. The residual stresses (ID7) were compared with XRD measurements that revealed compressive stresses on the substrate surface (−20 to −54 MPa); whereas they were close to zero at a depth of 70 μm (material was removed by electropolishing for sub-surface measurements as XRD has limited penetration capability). A parametric study was performed to study the effect of impact velocity, particle diameter, impact angle, particle shape and friction between the particle and substrate on the residual stress. Residual stresses generally increase with an increase in the above-mentioned parameters; however, noting that it remains unchanged for a friction parameter greater than 0.3.

Yildrim et al. [122] simulated impact of Cu particles on a Cu substrate and also found that increasing the impact velocity increased the magnitude and depth of compressive residual stresses (ID8). However, an increase in particle diameter was not influential and this was attributed to differences in strain rate effects because the simulated diameters were 50 μm and 5 mm. Yusof et al. [154] simulated the impact of spherical and elliptical shaped Al particles impacting Al substrate. The elliptical particle did not bond well to the substrate and induced tensile stresses (ID9) that can be harmful for the coating; while spherical particles induced compressive stresses, which is desirable in improving wear and fatigue life.

Ovideo et al. [155] performed a parametric study of the impact of SS316 particles on SS316 substrate using an explicit analysis. The parameters studied were particle velocity, temperature, mass, morphology and substrate temperature. Higher impact velocity increases the compressive residual stress while particles with lower temperatures have slightly higher compressive stresses (ID10). With the increase in particle mass, as indicated by an increase in diameter, the magnitude of residual stress decreases. This was attributed to the model size effects- a larger particle will have effects on a wider region of the substrate, which reduces the axial residual stress. Lower substrate temperatures lead to high compressive stresses in the substrate. This is consistent with the Johnson-Cook model used in the numerical model where plastic deformation at lower temperatures occurs at a higher flow stress.

Phan et al. [156] used a Lagrangian approach to study residual stresses for multiple Ti particles impacting a Ti substrate. It was seen that the residual stresses (ID11) were highest and tensile at the coating/substrate interface, which can be detrimental to the coating because it can cause crack formation and propagation. Wang et al. [157] used the ALE method to model the impact of Cu particle(s) on a Cu substrate for single and multiple particle impact. Residual stresses were reported in the X, Y and *Z*-directions (ID12). Residual stress in the x-direction is

compressive on the top of coating and reduces in magnitude with respect to thickness and eventually becomes tensile. The numerical model is in good agreement with the experimental XRD and contour methods.

Finite element birth and death methods[2] have also studied the thermal-mechanical deformation and residual stress distribution [155,158]. This method has been increasingly used in modelling of cold spray additive manufacturing where large components are simulated to study deformation and process parameter optimization. In the study performed by Lin et al. [158], it was found that the variation in residual stress is dictated by the scan direction; i.e., the direction and pattern of the power source to create a component in additive manufacturing. Stresses were higher towards the end of the scan. This observation can be used to optimize the scan strategy and reduce residual stresses in the final component. The drawback of using the finite element birth and death method is that it does not consider the peening effect that can affect the residual stresses below a deposition temperature of 400 °C. However, quenching and thermal stresses affect the residual stresses for systems exceeding a 400 °C deposition temperature, and these stresses can be captured by using the birth and death method [56,57].

Abu Bakar and Arif [159–161] combined a point cloud and a finite element method to model the spray process. Tensile stresses are formed in the earlier stages due to quenching, the stresses become compressive due to differences in thermal expansion. This analytical method is efficient because it uses the mesh of the deformed particles to perform FE calculations that predict the stresses. It was found that the presence of pores and cracks leads to stress relaxation, which is undesirable since it leads to preferential sites for crack initiation and propagation. The particle impact for these simulations was executed using the SPH method. After impact, the deformation is converted to point cloud and then to a FE mesh that is used to calculate residual stresses (Fig. 13a). Fig. 13b shows the residual stress contour obtained for a ceramic (yttria-stabilized zirconia, YSZ) coating and a SS301 substrate. The residual stresses are largely dominated by the post-deposition stresses due to differences in coefficients of thermal expansion [161].

Fardan et al. [47] studied the thermal spraying of YSZ on a stainless steel (SS) substrate. It was found that the thermal conductance between the coating and substrate can affect the residual stress values. This can be a challenge because the thermal conductance value must be given as an input for thermo-mechanical simulations when using Lagrangian and Coupled-Eulerian-Lagrangian methods. Lyphout et al. [162] studied the residual stresses for HVOF-sprayed Inconel 718 on an Inconel 718 substrate for impact velocities of 500 and 600 m/s. Compressive stresses (ID13) were found to be present in the coating/substrate interface and the magnitude decreased with the increase in coating thickness.

5.2. Experimental measurements of residual stresses

Several experiments have been dedicated to measuring residual stresses in CS coatings and CSAM components; e.g., non-destructive methods such as XRD [58–62,64,67,68,85,157] and neutron diffraction [65,66,69–74,81,82]. Other techniques such as material removal [60,62,68,79,83–87], contour method [71,72] and ring-opening test [90–93] can also be used to measure residual stresses. Diffraction techniques (XRD and neutron diffraction) are extensively used due to their non-destructive nature of measurement. However, XRD has penetration capabilities limited to several micrometres while neutron diffraction can penetrate up to several millimetres [163]. This limitation of XRD may be addressed by incremental electropolishing to remove the material so that through-thickness residual stresses can be measured [61,153]. However, the measured residual stresses can deviate from the original residual stress values. As material removal can lead to a change in volume which in turn affect the residual stresses. This is often

[2] Finite element birth and death refers to a technique where the finite elements can be activated or deactivated at the discretion of the user.

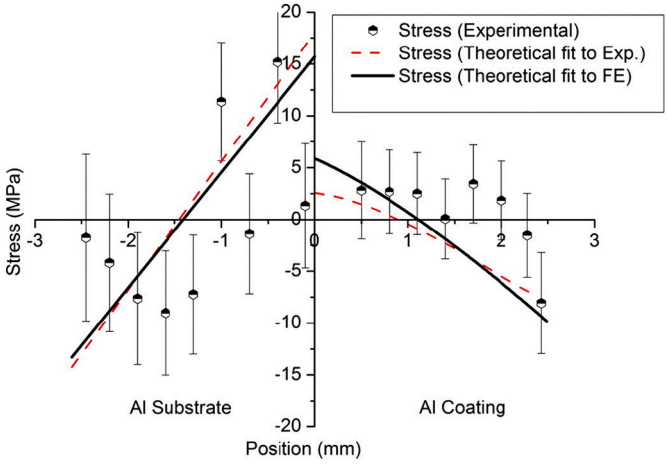

Fig. 14. Residual stress profile from neutron diffraction and numerical model with theoretical fits for AA6061-T6 coating on AA6061-T6 substrate [81].

overcome by compensating for the alteration, but this can prove to be quite difficult for anisotropic materials like cold spray coatings. Hence, a non-destructive technique like neutron diffraction is much more suitable to obtain residual stresses.

Neutron diffraction measurements have also been used to measure residual stresses in CSAM components [65,66]. Luzin et al. [65] studied residual stresses of Ti CSAM component on SS and Al substrates using neutron diffraction. The residual stresses were attributed mainly to the thermal stresses caused due to the different CTEs of the cold spray component and the substrate. It was concluded that the thermal stress was approximately 10 times larger than the deposition stress.

Luzin et al. [65] studied residual stresses in cuboidal components while Sinclair-Adamson et al. [66] studied cylindrical and funnel-shaped Cu components on Al substrate using neutron diffraction. Axial, hoop and radial stresses for both components were reported. The compressive residual stresses were comparable to the previously published results from CS coatings [49,73,75]. The residual stresses in CSAM reveals a lower magnitude than traditional casting or powder bed fusion methods; making it a suitable method for manufacturing certain geometries. Vargas-Uscategui et al. [72] studied residual stresses of CSAM Ti on a Ti substrate using neutron diffraction and the contour method. It is known that the residual stresses in CSAM depends on the component geometry [65,66]. Residual stress measurements showed that the inner and outer surfaces exhibited tensile stresses due to the thermal stresses that arise from temperature transients during the deposition process. It was also found that residual stresses were higher for low traverse speeds. This led to the conclusion that deposition with high traverse speeds and low feed rates were beneficial for CSAM deposition.

The process parameters during CS deposition affects residual stresses. Impact velocity, process temperature, alloy content and deposition speed influence residual stresses [70,72,93]. Spencer et al. [70] used neutron diffraction to measure the residual stress on Al, AA7075 and AA6061 coatings on Mg substrates. The residual stresses were dominated by peening stresses and not thermal stress for AA7075 and AA6061. This behaviour does not agree with the conclusion of Luzin et al. [65]. A probable explanation is that CS coatings formed from alloys are dominated by thermal stress rather than peening stress.

Spencer et al. [73] used neutron diffraction on a Cu/Al configuration and data-fitting by means of an analytical model. The residual stresses in Cu coatings were higher than in Al. Fig. 14 compares the neutron diffraction analysis with the numerical model and indicates good agreement but noting that the errors in experimental measurements are large. This higher deviation in experimental data might be attributed to the type of stresses, such as micro stresses, that are measured. Thus,

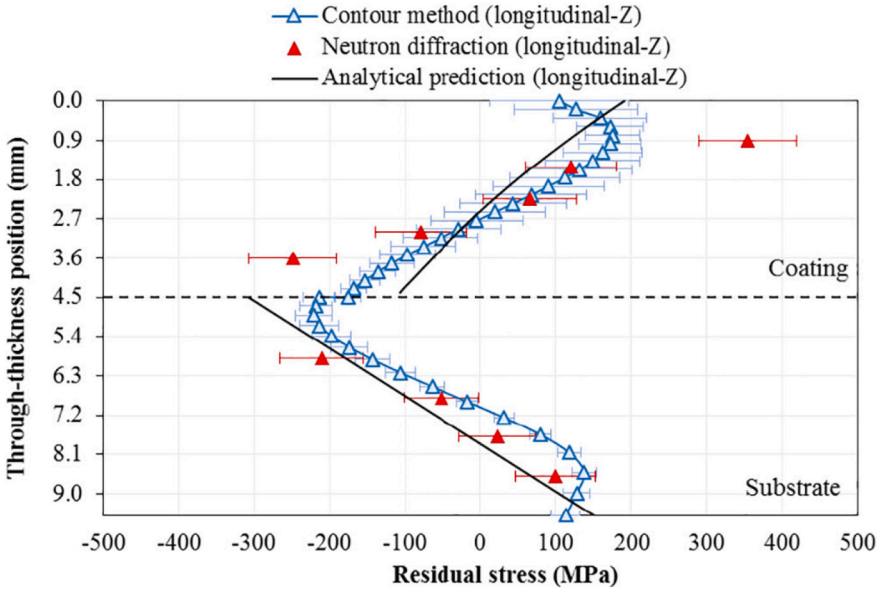

Fig. 15. Comparison of residual stress distribution for Ti6Al4V coating on Ti6Al4V substrate using experimental (neutron diffraction), contour method and analytical prediction [71].

there must be a good understanding of the technique and awareness of potential drawbacks.

Another effective way of measuring residual stresses employ analytical models, which are compared with experimental studies (neutron diffraction and contour method) [69–71,75,80,82]. Boruah et al. [71] studied residual stresses in cold sprayed Ti6Al4V coatings on a Ti6Al4V substrate using neutron diffraction, the contour method and an analytical model. The stresses were tensile on the top of the coating and then become compressive closer to the interface with the substrate. On the other hand, the stresses in the substrate are compressive near the interface and change to tensile through the thickness. The tensile stress was attributed to the higher deposition temperature. Hence, the quenching stress dominates the peening stress because of the thermal gradients imposed by the high deposition temperature. Fig. 15 compares the stress profiles from neutron diffraction, the contour method and the analytical model where it is observed that the analytical model reflects the same trends exhibited by the contour and neutron diffraction methods. The major inconsistencies appear at the coating – substrate interface; i.e., within a band of 2 μm. The neutron diffraction experiments exhibit a high deviation since these studies are limited to a crystallographic plane $\{10\bar{1}1\}$, which may be affected by texture and localized hardening [71].

Methods such as the contour method [157], material layer removal [62,83,86], hole drilling methods [60,68,84,85,87] and curvature measurement [62,83,84] techniques are also capable of measuring residual stresses. An additional method, the ring-opening test, involves cutting a ring and then measuring the deformation to obtain the residual stress [90–93]. The curvature measurement technique can measure deposition stress but is limited in comparison to other techniques. The curvature measurement technique is applicable to samples with certain shape and thickness, which hinders its usage in industry. Additionally, the residual stresses measured using curvature measurement can be inaccurate due to the model assumptions and considering the material behaviour to be linear [46].

Rech et al. [62] studied an Al cold sprayed coating on a AA6061 substrate using the curvature, material layer removal and XRD methods. There was a good agreement between the curvature and XRD methods with a difference of about 15–20% (standard deviation), while the deviation was about 30% for material layer removal. The discrepancy in the measured residual stress values is probably due to the difference in sample preparation with possible attribution to the different stress relaxation. It was also confirmed that the residual profile depends on the number of passes and the thickness of each pass [62].

Ryabchikov et al. [84] used hole drilling and curvature measurements to study Cu, Ni, NiZn, AlZn and Ni95Al5 cold sprayed coatings on an Al substrate. There were differences in the measured stresses between these two methods for the Ni and NiZn coating. The differences are largely due to variations in coating preparation or coating thickness. But it was concluded that the difference for the residual stresses arose from the plastic deformation that is inherent to the hole drilling method. Additionally, the hole drilling method has several other limitations. The residual stresses measured are macro-residual stresses and measuring micro-residual stresses can be difficult [68,79]. However, the micro-residual stresses can be measured using drilling steps smaller than the grain size [68]. The destructive nature of the hole drilling method influences the residual stresses since stress relaxation due to micro-cracking occurs in brittle materials [79]. The FE assumptions and the gauge volume measured can render comparison to other techniques difficult. The sample is assumed to be a homogeneous material and does not account for changes in microstructure such as microvoids, oxides between the deposited particles, and secondary phase particles. The assumption of material homogeneity can significantly affect the residual stress measured using the hole drilling method because local changes in Young's modulus [79] are not considered. Similarly, brittle phases within a composite coating material are prone to cracking during hole drilling, which can be difficult to incorporate when compensating for strain changes with drill depth.

Residual stresses for similar material combinations were mostly affected by peening stresses. Whereas, for dissimilar materials there can be effects of thermal mismatch stress due to different CTEs. As well, coating thickness, deposition pressure, deposition temperature, substrate temperature, stand-off distance, alloy content, surface preparation, and stress relaxation can affect the residual stresses. The influence of such processing variables can be investigated by numerical and analytical models to reduce the time, effort and costs associated with experiments.

6. Effect of process parameters

Process parameters affect the cold sprayed coatings [29,45]. This section examines these effects on cold spray numerical models with a

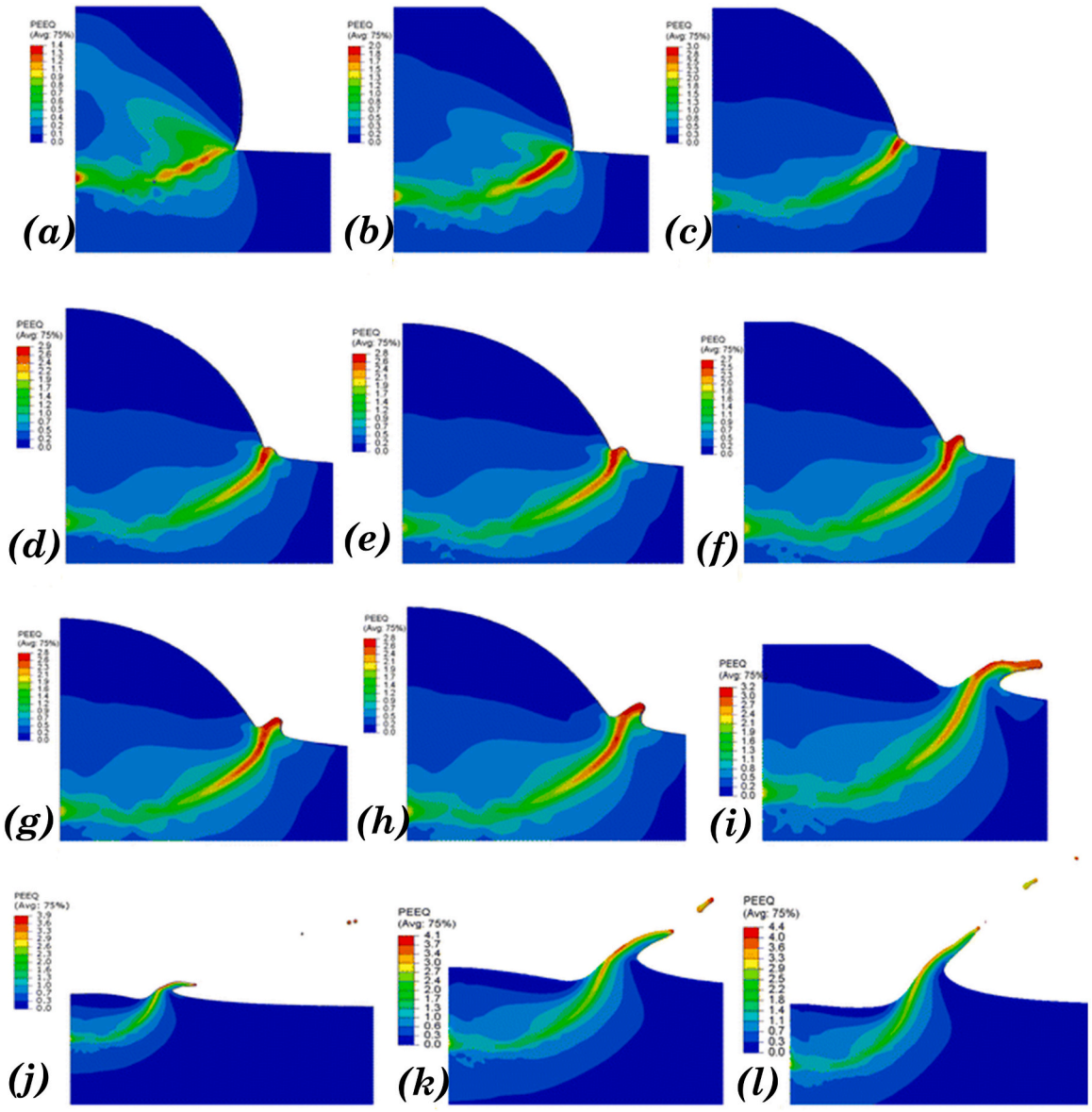

Fig. 16. Plastic contour for 20 μm Cu particle impacting Cu substrate at various impact velocities, (a) 200 m/s, (b) 250 m/s, (c) 280 m/s, (d) 290 m/s, (e) 300 m/s, (f) 310 m/s, (g) 320 m/s, (h) 330 m/s, (i) 400 m/s, (j) 500 m/s, (k) 600 m/s, (l) 700 m/s [126].

focus on particle deformation behaviour and residual stresses.

6.1. Particle impact velocity

The impact velocity of the cold sprayed particles is crucial to achieve bonding of the coating to the substrate. A particle with a higher impact velocity imparts higher kinetic energy that is converted to plastic deformation during impact [29,45].

Several studies have studied the effect of impact velocity (Table 2). These models have been dedicated to determining the critical velocity. Fig. 16 shows the effective plastic contour for a 20 μm Cu particle impacting a Cu substrate at various impact velocities. It is found that the phenomenon of jetting starts at an impact velocity of 290 m/s, which has been confirmed as the critical velocity of Cu from experiments [29]. From numerical simulations, it was observed that the jet formation continues until 400 m/s at which point there is a non-continuous jet. Thus, the deposition window is between 290 and 400 m/s for Cu as predicted from the simulation. A further observation is that the plastic deformation, crater size and jetting increases with an increase in impact velocity. Similar observations have been observed in other investigations on the effect of impact velocity [29,45].

There is no clear correlation between residual stresses and impact velocity [57,88,122,152,153,155]. Residual stress increases in for the Cu/Cu particle/substrate couple when impact velocity is increased from 300 to 500 m/s, whereas there is no change from 500 to 700 m/s. For the Cu/Al combination, residual stress increases between 300 and 500 m/s; while between 500 and 700 m/s, there is a slight increase in compressive stresses [57]. Song et al. concluded that the residual stress increases with an increase in impact velocity for Ti6Al4V/Ti6Al4V from 700 to 800 m/s [88]. However, the residual stress profiles for velocities of 700 and 800 m/s were similar but with higher magnitudes for the latter. However, the study of Li et al. [57] revealed noticeable changes in residual stress profile shapes. This might be attributed to a multiple impact simulation by Li et al. [57] and the inter-particle effect that affects the residual stress profile to a larger extent; while Song et al. used a single particle simulation [88]. The trend observed by other researchers is that residual stresses generally increase with an increase in impact velocity [122,152,153,155].

6.2. Particle and substrate temperature

Pre-heating the particle and substrate in CS coatings increases the deposition efficiency [29,45]. Increasing the particle and substrate temperatures causes thermal softening that facilitates deformation [32]. Pre-heating the particle and substrate provides a more uniform deformation. The plastic strain, flattening ratio, crater depth and jet length increased with the temperature increase of the particle and substrate [29,45,127,164].

Residual stress is also affected by the pre-heating temperatures used in the CS process. Oviedo et al. [155] studied residual stress for a SS316/SS316 couple combination for various pre-heating substrate temperatures. Through-thickness residual stress in three different directions-axial, shear and radial were presented. It was observed that as the pre-heating temperature is increased, there is a shift in the average residual stress from compressive to tensile stresses. This is because of quenching and thermal stresses dominating over peening stresses. It was also found that the residual stress profiles for the axial and shear directions were similar while radial residual stress profile was different. The effect of substrate pre-heating is more pronounced in radial and shear directions than in axial direction. In another study performed by Li et al. [57], there was minimal effect of pre-heating on Cu/Cu combination. But there were significant changes in residual stress contour for Cu/Al. The compressive stresses acting in the particle and substrate reduced with increase in pre-heating temperature from 100 °C to 300 °C. Hence, the nature and magnitude of residual stresses can change drastically with pre-heating temperature and material combination.

6.3. Particle diameter

Certain numerical studies have studied the effect of particle diameter on the CS process. It was found that for a fixed velocity the particle diameter (5 and 25 μm) did not influence the evolution of the particle and substrate shape [103]. On the other hand, the study by Gnanasekaran et al. [26] observed changes in effective plastic strain, shape and temperature; which was attributed to the increase in kinetic energy of the particle as its mass increased with respect to diameter. The temperature also increased with an increase in particle diameter due to a larger portion of kinetic energy being converted to heat and plastic energy. It was concluded that a particle of larger diameter leads to effective bonding and a successful coating. However, the higher temperature pushes the process to transition towards a thermal spray process with associated issues such as oxidation, phase transformation and melting [7,26,165].

The particle diameter also influences the critical velocity that is predicted for material combinations and other fixed parameters [4]. The general trend is that for the same material, larger diameters exhibit lower critical velocities than smaller diameters since smaller particles experience higher dynamic yield strength and behave stiffer due to higher strain rates [166]. Another explanation is larger particles have higher kinetic energy and require lower velocity to bond with the substrate [4].

Residual stress is also affected by the change in particle diameter [153]. It generally increases with an increase in particle diameter due to their higher kinetic energy causing a larger plastic region in the substrate. However, some studies have indicated no significant changes in plastic strain, temperature and residual stresses [122,166]. This deviation in behaviour can be due to several reasons such as (i) the diameters and material considered; as well as (ii) the assumptions embedded within the numerical model. For example, Yildrim et al. [122] considered diameters of 50 μm and 5 mm. These are large boundary conditions where no continuum in response would be expected since other studies have indicated that there are no noticeable changes after a certain diameter [143]. As well this particular numerical model, possibly, did not include heat transfer; nor did the material model capture the physical behaviour accurately [122,166].

No particles of different sizes impact with similar velocity or temperature in the practical application of cold spray. This results from the physics principle of the CS de-Laval nozzle that causes the larger particles to achieve a lower velocity at a higher temperature and vice versa. The CS process does not employ a fixed particle diameter but a particle size distribution. These practical complexities signify the attributes of numerical models in studying particle deformation, plastic strains, temperature and residual stresses. Studies on the way will have more realistic models that incorporate multiple particle impact with diameters similar to the particle size distribution in experiments [152]. Then, these models will need to be verified with the practice of cold spray so that optimization and efficiency gains can be realized.

7. Future research

Numerical modelling of cold spray particle impact has deepened the fundamental knowledge and understanding of this process. Temporal and local distribution of strains, stresses, temperature and pressure distribution have been explored by means of numerical models [16,29,45,103,167]. However, some materials phenomena are not considered in these models; for example, the role of micro and macro-cracks, stress relaxation, interactions between splats, impact onto an uneven surface or previously deposited layer, phase transformations, and microstructural changes. Furthermore, the specific numerical method has further limitations that must be considered. This section suggests future research in the numerical modelling of cold spray processes.

1. Modelling cracks: There are limited models that consider crack formation and propagation for cold spray particle impact. However, there are advances in crack modelling within the field of ballistic impact [168–170] that can be extended to cold spray. Crack modelling due to a single particle impact can be performed using a two-stage step. The first step consists of a dynamic explicit step where the particle impact is modelled. The second step builds on the first step where the reformed mesh, node displacements and stress are now used as input conditions for subsequent iterations. Crack propagation can be instigated by either a standard approach or XFEM (extended finite element method); taking note that (i) the standard method requires more manual intervention than XFEM, and (ii) XFEM has a higher computational time. This approach can be difficult when considering multiple impact problems because it requires multiple coupling between the two steps that increases significantly the computational time. The material properties are modelled using Johnson-Cook plasticity and fracture criterion; such as stress triaxiality [168] and fracture energy [169].
2. Phase transformation stresses: Temperature-dependent phase transformations occurring in cold spray [171] are not as significant when compared to thermal spray. Nevertheless, this field is important to explore since phase transformations lead to changes in the lattice volume and mechanical properties that cause stresses which can be modelled using finite element methods. The modelling technique would require phase transformation equations to be either defined within the finite element method or coupled with software capable of calculating phase diagrams and properties of different phases (e.g., CALPHAD approach by Thermo-Calc Software AB, Solna, Sweden or JMatPro, Sente Software Ltd., Surrey, United Kingdom). A CALPHAD approach is suitable to calculate the properties of the new phases that are then used in a finite element form to calculate stresses. Similar approaches have been used in powder bed fusion additive manufacturing [172,173] and welding [174]. Additionally, phase field modelling along with finite element and CALPHAD has been employed in thermal spray to understand solidification [172,173]. In addition to temperature-dependent phase transformations, some materials e.g. cobalt-based alloys undergo face centred cubic (fcc) to hexagonal close pack (hcp) transformation under high strain during

cold spraying or mechanical strain during service loading [175,176]. Although the transformations are strain-dependent, the rate of this transformation is temperature-dependent as indicated by Cavaliere et al. [176]. Finite element modelling of this strain transformation should thus be modelled as a temperature-dependent behaviour within the material definition.

3. Modelling the whole coating layer: Most models are dedicated to simulating single particle impact. Thick coatings can be simulated by the impact of multiple particles as the expense of high computational time; which makes this approach unattractive. Other methods such as modelling the coating layer through finite element birth and death methods [46] or analytical models [69] can be suitable alternatives. The birth and death method can also be described as a 'layer-by-layer' technique that has been extensively used for thermal spray coatings. However, technical issues arise for cold spray since it is necessary to include the peening effect; which is not an issue with thermal spray because thermal stresses dominate. Hence, future research can consider the inclusion of peening within the birth and death method. The attractive feature of this approach is the relatively low computational time. Modelling the whole coatings also serves the purpose of providing a base model which can be further developed to investigate the thermal and/or mechanical properties of the coating. Currently, mechanical evaluation of coating material in finite element does not include the coating build-up through individual splats. Instead, the microstructure is modelled as a single or composite material [177]. Modelling the whole coating can therefore improve the finite element based prediction of mechanical and/or thermal properties, including material damage behaviour during service loading e.g. using mesh deletion or node adjustment methods [178,179]. Such an approach will provide a complete design package interlinking coating build-up and its properties with superimposed residual stress.
4. Multiscale modelling: The above-mentioned future directions have *pro et contra*. Single or multiple particle impact provides more information at the expense of high computational time. While, the layer-by-layer (or 'birth and death') technique employs assumptions and approximations that may lead to inaccurate results, it is recommended that multiscale models can link these micro- and macroscale models [46,180]. The proposed computational framework would consist of modelling residual stresses at the microscale for single or multiple particles that would be used to generate a representative volume element (RVE). The RVE can be used to predict residual stress level at the macro-scale. Several RVE's can be developed for different process parameters (e.g., particle diameter, impact velocity, temperature) so that residual stresses can be studied [46].

8. Summary

A comprehensive review of the particle impact and residual stress modelling for Lagrangian, Eulerian, Coupled Eulerian-Lagrangian, Smoothed Particle Hydrodynamics, Molecular Dynamics and some hybrid methods were discussed. A brief section on experimental residual stress measurements utilizing XRD, neutron diffraction, material removal (layer and hole drilling), curvature measurement and deformation methods (contour and ring-opening tests) have also been presented. The following is a summary of the study:

1. The earlier particle impact models were modelled using Lagrangian methods. Some of the drawbacks are a) it requires very fine mesh (increased computational time), b) rebound in multiple particle impact and c) termination of the program due to extreme particle distortion. The Eulerian model was capable of simulating the high distortion process and was able to overcome the extreme particle distortion experienced in the Lagrangian method. The deformation from the Eulerian model was also comparable to the experimental observations. Some of the drawbacks in the Eulerian approach include very fine mesh requirement and the contact interactions cannot be varied as the software enforces default interactions.
2. From the study, it is seen that the SPH and CEL are superior to pure Eulerian and Lagrangian method due to their robustness and comparable results with experiments. It is also evident that hybrid models such as using point cloud with the FE method (SPH) can leverage the advantages of each method. Molecular Dynamics method could be of interest to study the microstructural changes (such as recrystallisation and dislocations) but the particle diameter is relatively small (in order of nm) which is a drawback.
3. The deformation bonding behaviour is affected by the material combination. The impact velocity has a certain range between which the bonding is effective. Too low velocity can lead to rebound and too high velocity can cause excessive jetting leading to material loss. It was believed that the adiabatic shear instability (ASI) was the reason for the bonding, but the study by Hassani et al. [18] gives a new mechanical view of adhesion (pressure waves causing hydrodynamic plasticity). The effects and influence of ASI are in question with regard to deformation mechanisms in CS according to Assadi et al. [21]. Nevertheless, this aspect of fundamental understanding has opened the discussion to consider hydrodynamic effects in CS coatings. It was also seen that there is a linear relationship between the mechanical properties (like Vickers hardness and Young's modulus/yield strength ratio) and the critical velocity of the similar material combinations. This means that materials with higher hardness and Young's modulus/yield strength ratio require a higher velocity to deform and adhere the particles to the substrate.
4. The maximum plastic strain and temperature were found to be acting in the surrounding region and not the initial contact zone. It was also reported that the temperature in the particle/substrate interface can reach close to its melting point leading to thermo-metallurgical bonding. Pre-heating the particle and substrate leads to a more synchronized deformation.
5. The residual stresses are dependent on the material combination, impact velocity and temperature of the particle/substrate. For cold-sprayed coatings, there is the presence of compressive stresses on the surface and tensile stresses closer to the interface for both coating and substrate. The effect of temperature is significant for dissimilar materials (e.g.: Cu/Al) while it is minimal for similar materials (Cu/Cu). There also exists a certain velocity above which the residual stresses do not change much. For incline impacts, larger incident angles (angle between incident direction and substrate surface) resulted in the larger compressive zone and higher magnitude of stresses. The residual stress state in cold sprayed coatings are affected by peening effect, dynamic strengthening and thermal softening of the material.
6. Residual stresses can be measured experimentally using non-destructive diffraction techniques like X-ray and neutron diffraction. XRD is widely used in material phase characterization and can measure residual stresses. However, XRD has limited penetration capabilities while neutron diffraction can penetrate up to a few mm. Some destructive techniques such as hole drilling and material removal also provided residual stress profiles similar to the diffraction techniques [60,62,68]. But there have also been certain studies where there can be discrepancies in the profiles [79]. This is because material removal technique is better capable of measuring macro-stresses while diffraction is suited for micro-stresses. However, micro-stresses can be measured using smaller incremental steps in the hole drilling method [68]. Curvature measurement is another experiment suitable for monitoring residual stresses. But curvature measurement is at times not suitable for softer materials due to the excessive plastic deformation and affects the residual strains being measured.
7. Experimental residual stresses also showed that the stress profile is highly affected by process parameters such as particle velocity, particle temperature, deposition pressure, substrate temperature,

Table 1
Summary of the different modelling techniques for cold spray impact modelling.

Method	Advantages	Disadvantages	Computational efficiency	Computational accuracy
Lagrangian	+ Less computational time + Good particle/coating interface tracing	- Termination of the program due to high mesh distortion - Rebound of particles in multiple impacts	High computational effort and time to simulate extreme deformation	Low Due to highly deformed elements
Smoothed particle hydrodynamics (SPH)	+ Capable of modelling extreme deformation	- Less accuracy - Tensile instability - Fine mesh to obtain accurate results - Higher computational time and effort	High computational effort and time to obtain results comparable to other FE methods	Low Requires fine mesh to obtain results comparable to other FE methods
Eulerian	+ Capable of modelling extreme deformation + Deformation pattern is comparable to experimental observations	- Requires fine mesh which increases computational time. - Particle deformation and numerical results affected by mesh size - Particle coalescence - Inter-mixing of particle and substrate - Mass scaling cannot be used	Lower computational effort and time	Good
Coupled Eulerian Lagrangian	+ Capable of modelling extreme deformation + Allows to model interaction between particle and substrate	- Particle coalescence - Requires fine mesh which increases computational time.	Lower computational effort and time	Good
Molecular dynamics	+ Understanding the atomic level mechanism + Capability of modelling deformation of grain boundaries, phase transformations and dislocation movement	- Size effect (nano-level in MD vs micro-level in FEA) - Time limitation (simulate time period of 1–100 ns) - Describing equations of motion and interatomic interactions can be difficult	N/A Very high computational effort and time to simulate micron-sized particle impacts	N/A Difficult to compare MD with other FE method in terms of accuracy

material, stand-off distance, number of passes, thickness of each pass, surface preparation, traverse speed etc. Numerical models are at times not capable of performing process parameter optimisation for such a large pallet of parameters. Some of the analytical models developed by Boruah et al. [69] and Tsui-Clyne progressive deposition model provide residual stress profile closer to the experiments. This signifies that way forward is to have a combination of numerical and analytical model to study the effects of different parameters.

From the author's knowledge, there are still some matters that need to be addressed via numerical simulations. Some of the issues not addressed in the simulations are stress relaxation due to cracks and residual stress due to phase transformations. Moreover, the recrystallisation mechanism should be also studied for a better understanding of the properties. The future direction would be to incorporate hybrid and interlinking multi-scale models to simulate thermo-mechanical with microstructural effects to provide a more holistic view.

Nomenclature

ALE	Arbitrary Lagrangian Eulerian
ASI	Adiabatic Shear Instability
CEL	Coupled Eulerian Lagrangian
CS	Cold spray
CSAM	Cold spray additive manufacturing
CTE	Coefficient of thermal expansion
EOS	Equation of state
FE	Finite element
FEA	Finite element analysis
HT	Heat transfer
HVOF	High-velocity oxygen fuel
JC	Johnson-Cook
MD	Molecular dynamics
MTS	Mechanical Threshold Stress
ND	Neutron diffraction
PTW	Preston-Tonks-Wallace
QCGD	Quasi-Coarse-Grained-Dynamics
RS	Residual stress
SPH	Smoothed particle hydrodynamics
SRH	Strain rate hardening
TS	Thermal softening
XRD	X-ray diffraction
ZA	Zerilli Armstrong

Symbols

A	JC static yield strength
B	JC strain hardening modulus
C	JC strain rate sensitive coefficient
C_o	Isentropic speed of sound
D	Material constant (MTS)
E	Young's modulus
e	Internal energy
E_H	Hugoniot internal energy
E_m	Internal energy per unit volume
G_p	Plastic shear modulus
G_0	Shear modulus at 0 K
m	JC thermal softening
M	Atomic mass
n	JC strain hardening exponent
p	Pressure
p_H	Hugoniot pressure
p_{PTW}	Strain hardening constant (PTW)
s	Pressure derivative of isentropic bulk modulus
s_0	Material constant at 0 K (PTW)
s_∞	Saturation stress near T_m
T	Temperature
T_m	Melting temperature
T_r	Reference temperature
T^*	Homologous temperature
T_0	Material constant temperature (MTS)
$\widehat{T}$	$\widehat{T} = T/T_m$

Table 2
Summary of the process parameters used in the numerical simulation of particle impact modelling. (HT – Heat transfer).

Particle				Substrate		HT	Method	Notes	Ref
Material	Diameter	Velocity (m/s)	Initial Temp (K)	Material	Initial Temp (K)				
Cu Ni Al	20 μm	351 374 514	298 298 298	Al Ni Al Cu Cu Ni	298	✓	Eulerian slice (ABAQUS)	Plastic strain and temperature results were reported. Temperature rise has been reported closer to the particle-substrate interface in the earlier stages of impact.	[2]
Cu	20 μm	500	298	Cu	298	✓	Lagrangian Symmetric (ABAQUS)	Max. plastic deformation and temperature were found in the surrounding region of the contact zone. Higher particle initial temperature promotes the bonding	[3]
Cu Al SS316 Ti Cu Al	5, 25, 100, 5000 μm 25 μm 25 μm 25 μm 25 μm 25 μm	(340–600) (400–790) (500–740) (560–830) (220–450) (450–900)	–	Cu Al SS 316 Ti Al Cu	–	✓	3D Lagrangian Symmetric (ABAQUS)	Various material combinations, impact speed and effective cohesive strength were used. Mechanical interlocking was observed for some combinations	[4]
Cu	20 μm	200–800 (410)	–	Cu	298	✓	2D axisymmetric Lagrangian (LS Dyna)	Critical impact velocity depends on the particle size and velocity distribution. Experimental results reported that oxygen content in the particle affects the critical impact velocity.	[13]
Cu	10 μm	550	298	Cu	298	✓	3D CEL ABAQUS symmetric model (1/4th)	Argued hydrodynamic plasticity causes bonding and not adiabatic shear instability. Plastic strain, Temperature and Von mises stress were reported. Lagrangian model was used to compare with published sources.	[18]
Cu, AA 1100	20 μm 80 μm 20 mm	200–500	298	Cu, AA 1100	298	✓	3D Lagrangian (ABAQUS)	Different settings such as usage of ALE, different meshing size, coefficient of friction and material damage were studied.	[25]
Cu	10–30 μm	350, 500	–	Cu	–	✓	3D SPH Lagrangian 2D SPH Lagrangian	Plastic strain, Temperature and Von mises stress were studied with the variation of particle diameter. 2D SPH method was used for incline and multiple particle impact	[26]
Cu	20 μm	300–700 (310)	–	Cu	–	✓	2D Lagrangian and ALE (LS Dyna)	Comparison between ALE and the Lagrangian method was performed	[27]
Cu	200 μm	500	–	Cu	–	✓	2D Lagrangian (LS Dyna)	Sequential and parallel impacts of 2 particles were performed. Multiple particle (5) impact was also reported.	[28]
Cu	5–40 nm	1000	300	Cu	300	✓	MD with LAMMPS	The evolution of stresses (direct and shear), von Mises stress and temperature data were reported.	[30]
Cu, Al	25 μm	400–700	300–700	Cu, Al	–	✓	Lagrangian, ALE and CEL (ABAQUS)	The impact angle was varied from 45° to 90°. Multiple impacts were also carried out. CEL was found to be effective in modelling the impacts and the results were compared to experiments	[31]
Cu	15 μm	310–890	–	AA 1100-H12 AA 7075-T6	–	✓	2D Lagrangian axisymmetric with ALE meshing	Temperature distribution for the numerical model was reported.	[32]
Cu/Al	20, 25 μm	500–840	Cu/Al	Cu/Al	300–873	✓	Lagrangian, ALE, SPH and CEL (ABAQUS)	CEL is robust and accurate for large deformations. Impact velocity and particle temperature had a significant effect on the results, while the coefficient of friction had minimal effects	[33]
Al Cu Ni	30 μm	120–780	300	Al Cu Ni	300	✓	Axisymmetric Lagrangian with ALE (ABAQUS)	Mie-Gruneisen EOS was used. Preston-Tonks-Wallace (PTW) material model was used to predict behaviour at high strain rates. To model the bonding FE is divided into 3 steps – particle impact, post-processing to find bonded elements and restarting simulation prior to rebounding. Mesh size1/200th particle diameter. The impact velocity started at 120 m/s and increased by 50	[34]

(*continued on next page*)

Table 2 (*continued*)

Particle				Substrate		HT	Method	Notes	Ref
Material	Diameter	Velocity (m/s)	Initial Temp (K)	Material	Initial Temp (K)				
								m/s until bonding occurred. And then reduced by 10 m/s to predict the minimum velocity.	
Al	10–30 μm	300–700	298	Mg	298	✓	ALE (ABAQUS)	Single and multiple particle impacts were deposited on a micro-channel substrate. Effect of particle size, velocity and the pre-heat temperature is studied.	[35]
Al	25 μm	650–900	–	Al	–	✓	SPH with FORTRAN	Experiments were also performed to compare the deformation and the interfacial bonding	[38]
Cu	10 μm	500	–	Cu	–	✓	Lagrangian and SPH in LS-Dyna	Studied variation in impact angle, particle diameter and SPH particle size. The size of the SPH particle size has a minimum effect on the results	[39]
Cu Al	25 μm	700 450–1000	–	Steel	–	✓	SPH and CTH	Performed comparison of SPH and CTH methods. Variation of velocity was used to study the adhesion of Al particle to steel	[40]
Al-Si	25 μm	200–1200	–	Mild Steel	–	✓	SPH	The critical velocity and the range was found for good adhesion of Al-Si particle on mild steel substrate	[41]
Al	20 μm	700–1300	165	Al	300	✓	Quasi-coarse-grained dynamics (QCGD), Molecular Dynamics	Mesocale microstructural development of single Al particle impact was carried out. Evolution of pressure, strain and temperature profiles were reported. Jetting behaviour is attributed to the interaction of shockwave velocity and velocity of particle/substrate interface.	[42]
Al	20 μm	700–1600	530	Al	298	✓	Quasi-coarse-grained dynamics (QCGD), Molecular Dynamics	Model capable of predicting microstructure and kinetics related to heat generation, dissipation, pressure evolution and propagation	[43]
Cu, Al, Ni, 316 L SS, Ti6Al4V	5–25 μm	400–800	295	Cu, Al, Ni, 316 L SS, Ti6Al4V	295	✓	Axisymmetric (ABAQUS)	Various material combinations and process parameters were studied. The adiabatic shear instability in particle/substrate region promotes the adhesion between particle and substrate.	[103]
Ni Al, SS304	22 μm 20 × 40 μm	500	400	AA6061-T6	400	✓	3D Lagrangian (ABAQUS)	Bonding is better for normal impact than angular impact. Plastic strain values from simulation values were compared with shear strength values from experiment and were in good correlation.	[115]
Vitreloy-1	30 μm	385–485	629–983	Carbon steel, SS, AA7075-T6, IN625	373	✓	3D Lagrangian (ABAQUS)	Metallic glass coatings on different metallic substrates have been studied.	[118]
WC-Co	40 μm	300–500	1000, 1200, 1300	SS	300	✓	Lagrangian (ABAQUS)	HVOF process to study impingement and bonding mechanism. The kinetic energy of the particle has a significant role in plastic stress localization and melting in particle/substrate interface	[181]
Cu	20 μm	200–700 (290)	–	Cu	–	✓	Eulerian slice (ABAQUS)	Plastic strain and temperature results were reported.	[126]
Cu	20 μm	290	323–973	Cu	323–973	✓	Eulerian slice (ABAQUS)	The effect of pre-heating the particle and substrate was carried out in the study.	[127]
Al Ti Al Ti	25 μm	(650–900) (750–1000) (400–1050) (630–800)	–	Al Ti Mild steel Al	–	✓	2D SPH Lagrangian	Various material combinations used to predict critical velocity.	[136]
WC12Co, W17Co	30 μm	400–700	700, 850, 1000	WC12Co, W17Co	373	✓	3D CEL symmetric (1/4th) ABAQUS	Pores were introduced in the particle. Plastic deformation, temperature and Von mises were reported.	[139]
Al	5–30 μm	500–800	373–573	Al-2017 T3	–	✓	CEL (ABAQUS)	Single and multiple particle impacts were carried out. Porosity, temperature and plastic strain data were reported.	[141]
Cu	5–20 Å	300–850	–	Cu	–	✖	MD	Plastic strain and Von Mises stress distribution was reported. For a velocity of 500 m/s and 20 Å, the bonding was good.	[143]

(*continued on next page*)

Table 2 (*continued*)

Particle				Substrate		HT	Method	Notes	Ref
Material	Diameter	Velocity (m/s)	Initial Temp (K)	Material	Initial Temp (K)				
Cu/Ni	–	300, 700, 1100	–	Cu/Ni	–	✓	MD	Bigger cluster (particle), higher velocity and higher temperature improves the bonding	[147]
Cu	2.892 nm	500–3000	500–1000	Cu	300	✓	MD	MD simulation was used for process parameter optimization. Impact velocity of 2000 m/s and temperature of 1000 K gave a smooth deposition.	[148]
Cu, Ni, Fe	10, 20, 30 μm	600, 700, 800	373–1073	Cu, Ni, Fe	298	✓	Lagrangian (ABAQUS)	Deposition behaviour of thermally softened particles was studied using numerical and experimental methods. Increasing particle impact temperature leads the particle to deform more intensively.	[164]
Cu	5 μm 10 μm	300–800	298	Al	298	✓	3D Lagrangian (ABAQUS)	Different particle sizes used to study the effect on critical velocity. Three-dimensional simulation is more accurate than two-dimensional due to the additional degrees of freedom.	[165]
High Density Polyethylene (HDPE)	50–500 μm	150–250	248, 298, 348	HDPE, PC, LDPE, Cu	298	✓	3D Lagrangian (ABAQUS)	Impact of polymer particle on particle substrate was studied. Impact velocity, temperature, diameter and the material combination is varied.	[166]
Cu	25 μm	400–700	298	SS	298	✓	CTH code (SANDIA)	Numerical simulations of splat and crater sizes were compared with experimental and were in good agreement.	[182]
Al Ni IN718 Fe Ti	20 μm	200–700 (300) (330) (500) (350) (520)	298	Al Ni IN718 Fe Ti	298	✓	Eulerian slice (ABAQUS)	Studied the impact of various materials on their respective substrates. The effect of variation in velocity was studied.	[183]
Cu Fe Ni SS304 Al IN718 Ti6Al4V	20 μm	250–700	298	Cu Fe Ni SS304 Al IN718 Ti6Al4V	298	✓	Eulerian slice (ABAQUS)	The model is used to predict the critical impact velocity. The paper also predicted critical velocities for Fe, Ni, SS304, Al, Inconel 718 and Ti6Al4V	[184]
WC12-Co	30 μm	375–425	1200	AISI 1045	300	✓	Axisymmetric Lagrangian (ABAQUS)	Optimum velocity was found to be 400 m/s. Adhesion and rebound energy was tracked and confirmed that bonding occurs in a range, and when plotted it is between the 2 intersection points. Above or below the intersection points the adhesion energy is lower than rebound which leads to particle rebound.	[185]
Ni Ti	30 μm 25 μm	500 500,750	298	Ni Ti	298	✓	Axisymmetric Lagrangian (ABAQUS)	Mie-Gruneisen EOS and Preston-Tonks-Wallace (PTW) were used. Morphology of crater of numerical and experimental micrograph are compared.	[186]
AA6061-T6	40 μm	612 612, 800, 980	298 509	AA6061-T6	298	✖	Lagrangian (ABAQUS)	Mie-Gruneisen EOS and Johnson-Cook model were used. Spray angle (45° to 90°) effect was studied for 612 m/s. Effect of velocity was studied for normal impact. Bonding strength increased with spray angle decreased from normal impact while deposition efficiency and strength of bulk material decreased. Increasing impact velocity and pre-heating temperature improves the quality of deposit.	[187]
Al Al_2O_3	~40 μm	457 451	418	Al6061	378	✓	2D Lagrangian (ABAQUS)	Mie-Gruneisen EOS and Johnson-Cook model were used. FE set-up consisted of aluminum particle impacting substrate followed by alumina impacting on aluminum. The shape of the particles was digitized from micrographs.	[188]
Cu	20 μm	290	298	Al, Ni, Steel 20, SS316L, Fe, IN718	298	✖	Eulerian (ABAQUS)	The deformation pattern and particle penetration depend on the material	[189]

(*continued on next page*)

Table 2 (*continued*)

Particle				Substrate		HT	Method	Notes	Ref
Material	Diameter	Velocity (m/s)	Initial Temp (K)	Material	Initial Temp (K)				
								combination. Preheating also provides a coordinated deformation.	
Ti6Al4V	30 μm	730 855	754 865	Ti6Al4V	573	✓	3D Lagrangian (ABAQUS)	Temperature, plastic strain and stress at 3 monitored elements were reported. High plastic deformation and higher temperatures at the peripheries correlated with the experimental observation.	[190]
WC-Co	20 μm	515–629	715–890	Carbon Steel, Al7075	373	✓	Lagrangian and CEL (ABAQUS)	The velocity and temperature employed in the FEA model were obtained from 1D simulations. The study was complementary to experiments and the particle adhesion was mainly due to high-rate, adiabatic plastic deformation of the substrate which leads to material jetting.	[191]
Cu Ni Mild steel	30 μm	300–700 300–850 300–850	298	Cu	298	✓	2D Lagrangian (ABAQUS)	Quantitative prediction of deposition efficiency. The square of plastic strain has a relation with the deposition efficiency.	[192]
Cu	30 μm	500	298	Cu	298	✓	2D Lagrangian (ABAQUS)	Different contact conditions such as tangential friction, normal constraint, and contact geometry are studied. The plastic strain is independent of contact conditions.	[193]
Al	20 μm	300–1000	300	Mg	300	✓	LS-DYNA (Lagrangian)	Single and 2-particle (parallel and sequential) impact were performed. Increased velocity leads to higher deformation and better bonding. Increase in incident angle weakens the bonding.	[194]
Al	25 μm	200–1000	300	Al	300	✓	SPH	The effect of adhesive forces on the rebound of particles at high speed was noticed.	[195]
AA 6061-T6	20 μm	300–900	298	AA 6061-T6	298	✖	Eulerian (LS-DYNA)	The effect of oxide film (0.3 μm) was studied on single and multiple particle impact. Incline impact and also impact on SS and Cu were performed.	[196]
Cu	20 μm	500	297	Cu	297	✓	Axisymmetric Lagrangian (ABAQUS)	Six different material models were tested. JC, PTW, MKHL, VA, MZA and GZ models were tested.	[197]
R-TiO_2	30 μm	800	298	Cu, AlMg3, SS304, Ti, R-TiO_2	298	✓	CEL and SPH (ABAQUS)	Ceramic particle impact on different metal substrates. SPH model to study the effect of surface roughness was also developed.	[198]
Ti6Al4V	10–90 μm	700–1025	800–855	Ti6Al4V	373	✓	CEL (ABAQUS)	Multiple particle impact. Velocity and temperature affect the porosity. High particle temperature and velocity lead to lower porosity. Particle temperature, velocity depends on the size of the particle.	[199]
Cu, Al	20 μm	300–500	25–600	Cu, Al	298	✓	Lagrangian (ABAQUS)	The effect of velocity, temperature, coefficient of friction and material were studied. Increase in velocity and preheating increased the plastic strain.	[200]
Ni	20 μm	440	290	Al, SS	290	✓	Lagrangian (ABAQUS)	Effect of spraying angle was studied. Al substrate deforms more due to the softer nature of the material.	[201]
Cu, Al, Ni, Ti	25 μm	400–950	298, 398, 498	Cu, Al, MS, Ti	298	✓	Lagrangian (ABAQUS)	Effect of surface roughness. Optimum surface roughness for different material combinations were obtained from the thermo-mechanical impact.	[202]
Cu Al	30 μm	450–750 600–850	298	Al Cu	298, 398, 498	✓	2D Lagrangian (ABAQUS)	Performed predictive assessment of deposition efficiency and compared with experimental measurements.	[203]
IN718	30 μm	672	780	IN718	298–723	✓	3D Lagrangian (ABAQUS)	Single particle impact with different preheat temperature to analyze particle bonding behaviour. Substrate preheating could increase the metallurgical bonding and promote coating/substrate adhesion strength.	[204]
Ni	20 μm	518	SS304	Cu		✓			[140]

(*continued on next page*)

Table 2 (*continued*)

Particle				Substrate		HT	Method	Notes	Ref
Material	Diameter	Velocity (m/s)	Initial Temp (K)	Material	Initial Temp (K)				
					298, 473, 673		Eulerian slice (ABAQUS)	It is found that the mechanical interlock of the particle and substrate improved when the substrate temperature is increased.	
Ni	20 μm	300, 500, 700, 900	298	Al 6061, Cu, SS	298	×	Eulerian (LS-Dyna)	Single and multiple particle impact is performed. High velocity leads to higher erosion.	[205]
Cu	20 μm	500	298	Cu	298	✓	2D Lagrangian (ABAQUS)	Early numerical model that tests different settings such as solution procedure, hourglass control, element distortion control, ALE meshing, interface friction, material damage and meshing size	[121]
CP-Ti	25 μm	200–1000	298, 873	CP-Ti	298, 873	✓	2D Lagrangian (ABAQUS)	Single and multiple particle impacts were carried out. Velocity and temperature were varied to study the bonding features and deposition mechanism.	[206]
Cu	20 μm	600, 900 m/s	298	Ni, Al, SS, CS (20 steel)	298	×	2D axisymmetric Lagrangian and Eulerian slice (LS Dyna)	Hardness of the substrate can affect the deformation behaviour of the particle. This is seen only when coatings are thin and not for thick coatings.	[207]
AISI 4340 steel	~180 μm	350–700	–	AISI 4340 steel	–	✓	Lagrangian (ANSYS AUTODYN)	The transfer from impact energy to plastic deformation is studied for different impact angle. The crater volumes from the experiment were compared with the numerical model.	[208]
Ash particle	200 μm	20	–	SS	–	×	DEM	DEM was used to predict the wear rate and erosion mechanism. It was found that shear impact energy affects the wear rate. Simulation is compared with previous experimental data.	[209]
Zn, Al	20 μm	450–500	–	Steel	–	✓	2D Lagrangian (LS-DYNA)	Effective plastic strain contour and morphology were compared with experiment.	[210]
Cu, Ni	–	200–1000	423	SS316, Cu	298	×	3D Lagrangian (ABAQUS)	Critical velocity is estimated for different material combinations. Critical velocity is found to be related to adiabatic shear instability due to high strain rate.	[211]
Cu, SS 316 L	25 μm	–	–	Cu, SS316L	–	✓	2D axisymmetric Lagrangian (ABAQUS)	Analytical and numerical simulations were done. Analytical calculations were used to estimate corrosion and erosion velocities.	[212]
Ti	28 μm	760	1100	Ti, Al, Zr	298	✓	Lagrangian (ABAQUS)	Warm spraying of Ti particle on Ti, Al and Zr substrates were performed. The bonding behaviour was compared with the experimental study.	[213]
Cu	20 μm	200, 430	313	Al	333	✓	2D axisymmetric Lagrangian (ABAQUS)	Bonding of cold sprayed particles was studied using numerical and experimental methods. Mechanical and physical-chemical adhesions were studied. The deformation shape from the numerical model was compared with the experiment.	[214]
Cu	20 μm	100–600	298	Cu	298	✓	2D axisymmetric (MSC-Marc)	Numerical simulation along with the material model is used to identify dislocation distribution. Cell size distribution, plastic strain, temperature and stress distribution have been reported.	[215]
Ti	56.29 × 20 μm	290–473	373–873	Al, SS	298	✓	2D Lagrangian (ABAQUS)	Elliptical shape particle to replicate the experiment. Incline impacts have been also performed. Critical velocity for Ti/SS is lower than Ti/Al. Higher substrate hardness of SS is a reason for this.	[216]
Armco Fe, SS	50 μm	800	353	SS	293	✓	Lagrangian (ABAQUS)	Numerical model is used to characterize the strain localization at the particle/substrate interface.	[217]
AA 5056	25 μm	762–1067	293	AA 6061-T6	293	✓	Lagrangian (ABAQUS)	Two-step ABAQUS analysis- dynamic impact and quasi-static fracture	[218]

(*continued on next page*)

Table 2 (*continued*)

Particle				Substrate		HT	Method	Notes	Ref
Material	Diameter	Velocity (m/s)	Initial Temp (K)	Material	Initial Temp (K)				
								analysis using Virtual Crack Closure Technique.	
Al	30 μm	500	348	Steel 4340	398	✓	2D Lagrangian (ABAQUS)	Surface roughness and preparation method is used to study numerically and experimentally.	[219]
Al	40 μm	100–800	293	Al	293	✓	(ABAQUS)	Adhesion and rebound phenomenon with the increase in impact velocity is studied. A window of velocity is identified. Below this velocity, the rebound is due to elastic energy and above this window it is due to the material strain rate effects	[220]
Ta	–	572	–	Cu	–	×	ALE (ABAQUS)	The 3D model is used to predict the deformation. The particle shape is irregular similar to the experiments.	[36]
Al	30 μm	~580	293	304 SS	293	✓	3D Eulerian (ABAQUS)	The presence of water film for the underwater cold spray is studied. Higher kinetic energy was required for good deposition to break through the water film present on the substrate.	[221]
Cu Ni Fe Al Ti6Al4V IN718	20 μm	300 390 360 420 500 490	298	Cu Ni Fe Al Ti6Al4V IN718	298	✓	Eulerian slice (ABAQUS)	The effect of changing velocity, pre-heat temperature, void size and Eulerian slice thickness were studied. Size of the void influences the solution while the Eulerian slice thickness doesn't have an effect. There is a linear relationship between preheat temperature and critical velocity.	[222]
Cu Ni Ni	20 μm	300–650	298-	AA6061 Cu Al	298–582	✓	Eulerian slice (ABAQUS)	Critical velocity for different material combinations obtained. Pre-heating is used to soften the particle before impact. However, the critical velocity from simulation didn't agree with experiments.	[223]
Cu	16.5	650	623	Cu	573	✓	3D SPH Lagrangian (In-house)	Temperature and strain rate effects have been studied. Johnson-cook model modified to fit with experimental results.	[224]
Ceramic	30 μm	800	298	Cu, Al, MS	298	✓	CEL (ABAQUS)	Particle is Lagrangian and the substrate is Eulerian. Ceramic particle properties are arbitrary, and the particle density and impact angle is varied to study substrate deformation.	[225]
Cu Ti	30 μm	450 650	298 673	Al, SS Ti	298–1273	✓	Axisymmetric (ABAQUS)	Micro and macro model compared with experiment. Substrate with lower effusivity and substrate preheating can result in improved quality of cold sprayed coating.	[226]
Cu	25 μm	571	357	Cu	~293	✓	3D Lagrangian (ABAQUS)	Parameters from OpenFOAM is utilized to model particle impact. The morphology is compared to the SEM images from the experiment.	[227]
Cu	20 μm	300–700	–	Cu	–	✓	MPM (Material Point Method)	Single particle and multiple particle impact analysis were carried out. MPM results compared with FE and experiment in terms of compression ratio.	[228]
Cu Clad diamond	26 μm 50 μm	600 480	–	Al	–	×	Axisymmetric Lagrangian (ABAQUS)	Two different particle- Cu (26 μm) and Cu clad diamond (50 μm) were impacted sequentially. The contact stress of the impact is used to gauge the fracture points in the coating.	[229]
Al	25 μm	400 800	300	Al	300	×	SPH Lagrangian	Lower velocity (400 m/s) is suitable for depositing lighter materials like Al as it results in less porosity.	[230]
Ti	64 μm	589	–	Cu, Al, SS	–	×	3D Lagrangian (ABAQUS)	The substrate hardness and impact angle impact the bonding of the particle and substrate. A similar behaviour was observed in experiments performed.	[231]
Ti	2 nm 20 nm	350–700	300	Ti	300	✓	MD (LAMMPS)	High strain rates and temperature plays a role in the deformation process. Larger diameter causes a higher	[232]

(*continued on next page*)

Table 2 (*continued*)

Particle				Substrate		HT	Method	Notes	Ref
Material	Diameter	Velocity (m/s)	Initial Temp (K)	Material	Initial Temp (K)				
								temperature increase than a smaller particle.	
Al	1 mm	200–700	300	Ni, Cu, Al, Steel, Ti	300	✓	MD (LAMMPS)	Critical velocities determined using experimental and numerical simulation.	[233]
Cu	25 μm 50 μm	800	293	Carbon steel	293	✓	3D Lagrangian (ABAQUS)	Symmetric and non-symmetric multiple impacts performed. Experimental and numerical methods used to study mechanical properties and microstructure.	[234]
Ti	60 μm	600	423	AISI 1050 AISI 2017 Cu Ti6Al4V	423	✓	2D Axisymmetric Lagrangian (ABAQUS)	Numerical analysis used to complement experiment. The increase of temperature in the particle-substrate interface was reported.	[235]
Nb	25 μm	442–515	393–453	Nb	393–453	✓	2D Axisymmetric Lagrangian (ABAQUS)	Variation in velocity and temperature is studied in single and multiple particle impacts. Experiments were performed and FE is used to study Nb coating.	[236]
IN718	25 μm	300–700	873	IN718	300	✓	2D Axisymmetric Lagrangian (ABAQUS)	A numerical model is used to predict critical velocity. Plastic strain of the particle and substrate are dominant factors.	[237]
Metallic glass (Vitreloy-1)	30 μm	385–485	629–983	AISI 4340	–	✓	3D Lagrangian (ABAQUS) with ALE	–	[238]
CRC-410 CRC-425 CRC-300 Amperit 584 Amperit 587 Diamalloy 304	~45 μm	~435 ~430 ~451 ~499 ~509 ~471	–	AISI 4340	463–472	✓	2D Lagrangian (ABAQUS)	Commercially used alloy powders are studied using experimental and numerical simulations. Ceramic and metallic contents were identified, then the shapes identified from SEM are inputted in the numerical model to study the impact behaviour.	[239]
Al	30 μm	380	629	Al7075	298	✓	Eulerian (ABAQUS)	Sequential impact of particles carried out.	[240]
Cu	25 μm	20	298	PEEK	298	✓	Lagrangian (ABAQUS)	Metallic coatings on polymer substrate. Material jet was formed at the substrate at the which facilitates the deposition of coating.	[241]
IN718	22 μm	400 to 1200	–	IN718	–	✓	Lagrangian (ABAQUS)	Single particle impact used to study the deformation. Two different sets of parameters used in the simulations.	[242]
Cu	10 μm	500	298	Al	298	✓	Lagrangian (ABAQUS)	Single and multiple particle impact was performed.	[243]
Cu AA6061 Ti6Al4V	41 μm 22.7 μm 39.6 μm	500 530 1100	298	Cu AA6061 Ti6Al4V	298	✓	2D Lagrangian (ABAQUS)	Different materials belonging to the "soft" and "hard" group were studied. Model could capture strain-rate sensitive behaviour.	[244]

Note: Velocity in brackets were explicitly mentioned as critical velocities for the given process parameters.

U_s Shock velocity
U_p Particle velocity
V Specific volume
y_0 Yield stress constant at 0 K
y_1 Medium strain rate constant
y_2 Medium strain rate exponent
y_∞ Yield stress constant at T_m

Greek symbols

β High strain rate exponent
Γ_o Material constant (Mie- Gruneisen)
Γ Gruneisen parameter
γ Strain rate dependence constant
ε Equivalent plastic strain
$\dot{\varepsilon}^*$ Dimensionless plastic strain rate
$\dot{\varepsilon}$ Strain rate
$\dot{\varepsilon}_o$ Reference strain rate
$\dot{\varepsilon}_p$ Plastic strain rate
$\dot{\zeta}$ MTS parameter
η Nominal volumetric compressive strain
θ Strain hardening rate
κ Temperature dependence constant
ν Poisson's ratio
ρ Density
ρ_o Reference density
σ Stress response
$\hat{\tau}_s$ Normalized work-hardening saturation stress
$\hat{\tau}_y$ Normalized yield stress

Declaration of competing interest

The authors declare that they have no known competing financial interests or personal relationships that could have appeared to influence the work reported in this paper.

Acknowledgements

CCB has the support of the Australian Research Council under the

Table 3
Summary of the process parameters used in the numerical simulation for residual stress modelling.

Particle				Substrate		Verification	RS values	Method	Notes	Ref
Material	Diameter	Velocity (m/s)	Initial Temp (K)	Material	Initial temp (K)					
AA 6061-T6	15 μm	585	–	AA 6061-T6	–	Neutron Diffraction and Tsui-Clyne analytical model	ID1: 40 to −125 MPa	SPH	Multiple particles (400 particles) were used to obtain the residual stresses. The results were compared with neutron diffraction measurements and Tsui-Clyne analytical model	[81]
Ti6Al4V	30 μm	700 800	–	Ti6Al4V	573	Focused Ion Beam Digital Image Correlation	ID2a: 176 to −352 MPa ID2b: 528 to −176 MPa ID2c: −32 to 52 MPa [149]	3D Lagrangian ABAQUS	Residual stress from the simulation was compared with experimental results obtained by Focused Ion Beam- Direct Image Correlation	[88]
Cu	20 μm	500–700	373–573	Cu Al	298	Neutron Diffraction [75]	ID3a: 150 to −25 MPa ID3b: 50 to −140 MPa	Eulerian slice (ABAQUS)	Single and multiple particle impact. Residual stress in the direction of the velocity was also reported.	[57]
YSZ	30 μm	100–240	3067–3250	SS	423	Hole Drilling Method [245]	ID4b: 225 to −200 MPa	CEL and Eulerian (ABAQUS)	The model predicted residual stresses and compared with experimental results (hole drilling method) from the literature	[47]
Al Al Al Cu Cu Cu Ti Ti Ti	20, 25 μm	500	298	Al Cu Ti Al Cu Ti Al Cu Ti	298	–	ID5a: 1662. To −192.3 MPa ID5b: 302.8 to −120.6 MPa ID5c: 155.9 to −204.5 MPa ID5d: 459.2 to −251.4 MPa ID5e: 210.9 to −171.4 MPa ID5f: 296.5 to −3703 MPa ID5g: 519.6 to −496.4 MPa ID5h: 424.9 to −576 MPa ID5i:284.8 to −625.6 MPa	3D Lagrangian (ANSYS-AUTODYN)	Normal and incline impacts for different material combinations (0°, 30°, 60°, 90°). Larger incident angle resulted in in a larger compressive zone and residual stress. Yield strength and density of the material influenced the residual stress. Residual stresses are presented as Von-Mises stress	[150]
AA6061	19 μm 11–78 μm	850–1050 600–1300	293	AA6061	293	X-Ray Diffraction	ID6: 100 to −350 MPa	3D Lagrangian (ABAQUS)	Three cases-single (19 μm), overlapping impact of 6 particles (19 μm) and multiple random impacts (11–78 μm). Residual stresses are reported for different bonding models.	[152]
Al	20–60 μm	400–900	293	Mg	293	X-Ray Diffraction	ID7: 50 to −100 MPa	LS-DYNA	Single and multiple impact analysis is performed. Johnson-Cook and Gruneisen models were used. A parametric study was also performed.	[153]
Cu	50 μm	100–700	293	Cu	293	–	ID8: 275 to −75 MPa	2D Lagrangian and ALE 3D Lagrangian (ABAQUS)	Material failure was also considered in the Lagrangian model. Residual stresses were also studied with varying impact velocities.	[122]

(*continued on next page*)

Table 3 (*continued*)

Particle				Substrate		Verification	RS values	Method	Notes	Ref
Material	Diameter	Velocity (m/s)	Initial Temp (K)	Material	Initial temp (K)					
Al	25 μm	400	300	Al	300	–	ID9: 100 to −400 MPa	SPH	Irregularly shaped particle induces tensile stresses and is harmful for the coating. Spherical particles are better due to the formation of compressive stresses.	[154]
SS316	15–75 μm	400–800	800–1600	SS316	300–1000	–	ID10: 400 to −400 MPa	2D Lagrangian Axisymmetric (ABAQUS)	The effect of particle diameter, particle velocity, particle temperature and substrate temperature are studied. Peening, quenching and thermal residual stresses are studied. Some comparison with published literature	[155]
Ti	22 μm	700	873	Ti	300	–	ID11: 414 to 600 MPa	Lagrangian (ANSYS-AUTODYN)	Higher stress in coating than the substrate. Residual stress is higher in coating/substrate interface which can act as a point of crack formation.	[156]
Cu	36 μm	500	298	Cu	298	Contour method and X-ray diffraction	ID12: 150 to −200 MPa	ALE	Single and multiple particle impact performed. Residual stresses are simulated and compared with experimental methods using XRD and contour method.	[157]
IN718	50 μm	500, 600	1543	IN718	–	Neutron diffraction and modified layer removal method	ID13: 250 to −600 MPa	2D Axisymmetric Lagrangian (MSC Marc)	The HVOF numerical results have been compared to experimental results (neutron diffraction and material layer removal method).	[162]
Cu Cu Al Al	35 μm	579–677	456–598	Cu Al Cu Al	293	–	ID14: −25 to −250 MPa	Lagrangian (ABAQUS)	Three and 100 particle impact were performed.	[246]

Table 4
Summary of the experiments measuring residual stresses (RS) in cold sprayed coatings. (C – Coating, S – Substrate, XRD – X-ray Diffraction, ND – Neutron Diffraction, MR – Material removal (hole drilling and material layer removal), CM – Curvature measurement, Misc. – Miscellaneous, AM – Analytical model, FEM – Finite element model).

Coating		Substrate		RS values	Experimental method					AM	FEM	Notes	**Ref**
Material	Thickness (mm)	Material	Thickness (mm)		XRD	ND	MR	CM	Misc.				
Al_2O_3+A380	1-2	AA6061	3	C: -15 to -90 MPa	✓	✖	✖	✖	✖	✖	✖	Two different blends of Al2O3 with A380 were made – spherical and irregular shaped. Only surface residual stresses were presented.	[58]
IN718	1.22 – 1.30	IN718	3	C: -100 to -400 MPa S: -400 to 300 MPa	✓	✖	✖	✖	✖	✖	✖	Different processing conditions are used and XRD is used to measure residual stress at the surface and the middle of the coatings.	[59]
IN718	0.073 0.211 0.350	IN718	5 to 6.5	C: -50 to -250 MPa S:-400 to 80 MPa C: -50 to -250 MPa S: -250 to 50 MPa C: -100 to -200 MPa	✓	✖	✓	✖	✖	✖	✖	Hole drilling method for 3 thicknesses. XRD for the thin coating after annealing. This caused stress relaxation in the coating, the substrate remains relatively unchanged.	[60]

(*continued on next page*)

Table 4 (*continued*)

Coating		Substrate		RS values	Experimental method					AM	FEM	Notes	Ref
Material	Thickness (mm)	Material	Thickness (mm)		XRD	ND	MR	CM	Misc.				
AA6061	10	AA6061-T6	6	S: -200 to 0 MPa Direction-1 C: 0 to -40 MPa S: -40 to 50 MPa Direction-2 C: -20 to 45 MPa S: 0 to 45 MPa	✓	✖	✖	✖	✖	✖	✖	XRD measurements in different directions. Electropolishing used to get residual stress profile.	[61]
Al	0.674-0.845	AA6061	2 5.95	C: 100 to -350 MPa S: 180 to -450 MPa	✓	✖	✓	✓	✖	✖	✖	The effect of substrate temperature on residual stress is studied. Stress profile obtained using the MR method (layer removal).	[62]
IN718	4	Al	-	C: -400 to 400 MPa	✓	✖	✖	✖	✖	✖	✖	Comparison of cold sprayed and laser-based powder bed fusion performed. Residual stress was high after machining.	[64]
Ti Al		SS Al	-	Ti: -50 to -150 MPa SS: 300 to -200 MPa Ti: -10 to -175 MPa Al: 50 to -50 MPa	✖	✓	✖	✖	✖	✓	✖	Two different geometries were additively manufactured – a thin (3.3 mm) and a thick sample (5.2 mm). The presence of compressive stress on the top surface is beneficial as it prevents crack formation and propagation.	[65]
Cu		Al 6061	-	Cylinder: 103 to -58 MPa Funnel: 100 to -123 MPa	✖	✓	✖	✖	✖	✖	✖	Two geometries were additively manufactured - a cylinder ($\varphi = 15$ mm, height = 100 mm) and a funnel. The stresses in three directions- axial, hoop and radial were presented. The presence of compressive stress on the top surface is beneficial as it prevents crack formation and propagation. Residual stress magnitudes lower than casting and powder-based additive manufacturing where melting is involved.	[66]
Zn	-	Mild Steel	2	C: -0.5 to 26.1 MPa	✓	✖	✖	✖	✖	✖	✖	Different processing parameters used. residual stress range is for all the scenarios.	[67]
Al (AlZn5.5MgCu)	0.14 mm	Steel (S355J2)	2.36	-75 to 50 MPa	✓	✖	✓	✖	✖	✖	✖	Comparison of hole drilling and X-ray diffraction. Micro-stresses by hole drilling and XRD are comparable.	[68]
Cu Cu Al	-	Cu Al Cu	-	Cu(C): -50 to 10 MPa Cu (S): -50 to 60 MPa Cu(C): -80 to 30 MPa	✖	✓ [70,75,80]	✖	✖	✖	✓ and [151]	✓ [80,81]	The analytical model developed in this study is used to compare with finite element modelling, neutron diffraction and Tsui-Clune analytical model.	[69]

(*continued on next page*)

Table 4 (*continued*)

Coating		Substrate		RS values	Experimental method					AM	FEM	Notes	Ref
Material	Thickness (mm)	Material	Thickness (mm)		XRD	ND	MR	CM	Misc.				
Al7075		Mg		Al (S): -75 to 110 MPa Al (C): -10 to 10 MPa Cu (S): -30 to 20 MPa								The model developed is in good agreement with the results obtained through other methods.	
Al6061		Mg		Al7075 (C): -70 to 30 MPa									
Al-6061-T6		Al6061		Mg (S): -80 to 110 MPa Al6061 (C): -20 to 20 MPa									
Ti		Cu		Mg (S): -45 to 50 MPa									
Al		Mg		Al-6061(C): -20 to 10 MPa Al-6061 (S): -10 to 20 MPa Ti (C): -20 to 20 MPa Cu (S): -30 to 50 MPa									
Al		Mg	3	Al (C): -15 to 10 MPa Mg (S): -10 to 30 MPa ©(C); -20 to 30 MPa Mg (S): -10 to 5 MPa	✖	✓	✖	✖	✖	✓	✖	Peening is significant than thermal mismatch stress.	[70]
AA7075				AA7075 (C): -70 to 70 MPa Mg (S): -70 to 90									
AA6061				AA6061 (C): -30 to 20 MPa Mg (S): -40 to 60 MPa									
Ti6Al4V	4.5	Ti6Al4V	5	C: -250 to 350 MPa S: -225 to 100 MPa	✖	✓	✖	✖	✓	✓	✓	Neutron diffraction, contour method with FEM and analytical model were used.	[71]
Ti	50 mm	Ti	10 mm	C: -125 to 60 MPa	✖	✓	✖	✖	✓	✖	✓	Neutron diffraction and contour method (with FEM) were used.	[72]
Cu	3	Cu	3.1	Cu (C): 10 to-40 MPa	✖	✓	✖	✖	✖	✓	✖	RS in Cu coatings is higher than Al.	[73]
Al	3	Cu	3.1	Cu (S): 60 to-45 MPa									
Cu	3	Al	2.6	Al (C): 10 to-10 MPa Cu (S): 5 to -5 MPa									
Al	3	Al	2.6	Cu (C): 40 to -80 MPa Al (S): 90 to-70 MPa									

(*continued on next page*)

Table 4 (*continued*)

Coating		Substrate		RS values	Experimental method					AM	FEM	Notes	Ref
Material	Thickness (mm)	Material	Thickness (mm)		XRD	ND	MR	CM	Misc.				
Al	1.96	Al	3.08	Al (C): 5 to -10 MPa Al (S): 20 to -12.5 MPa C: 5 to -25 MPa S: 50 to -25 MPa	✖	✓	✖	✖	✖	✓	✖	Good agreement between neutron profile and Tsui-Clyne model.	[74]
Cu	3	Cu	3.1	Cu(C): 10 to-40 MPa Cu (S): 60 to-45 MPa	✖	✓	✖	✖	✖	✓	✖	RS in Cu coatings is higher than Al coatings. A higher plastic strain is experienced in Cu particles impact.	[75]
Al	3	Cu	3.1										
Cu	3	Al	2.6	Al(C): 10 to-10 MPa Cu (S): 5 to -5 MPa									
Al	3	Al	2.6										
AA6061-T6		AA6061-T6	-	Cu(C): 40 to -80 MPa Al (S): 90 to-70 MPa Al(C): 5 to -10 MPa Al (S): 20 to -12.5 MPa S: -14 to 30 MPa C: -13 to 7.5 MPa	✖	✓	✖	✖	✖	✖	✓	Experimental and numerical work carried out. A good fit between experimental and numerical results (scaled values).	[81] [82]
IN718	0.216 – 1.173	IN718	3	C: -500 to -200 MPa S: -300 to 200 MPa	✖	✖	✓	✓	✖	✓	✖	RS reduces with increase in coating thickness. The analytical model is based on Hertzian contact Ilyushin's elasto-plastic theory.	[83]
Cu	MR: 0.44 CM: 0.43	Al	1.47	-51 MPa -37 MPa	✖	✖	✓	✓	✖	✖	✖	MR (hole drilling) and CM used to characterize RS.	[84]
Ni	MR: 0.34 CM: 0.27			-98 MPa -57.9 MPa									
NiZn	MR: 0.07 CM: 0.21			-420 MPa -97.1 MPa									
AlZn	MR: 0.22 CM: 0.25			-22 MPa -35.5 MPa									
AA7075		Mg (AZ31B-H24)	-	Al7075 (C): -80 to 20 MPa Mg (S): -180 to 0 MPa	✖	✖	✓	✖	✖	✖	✖	Hole drilling method utilizing Fiber Bragg Grating sensors and thermocouples used to do in-situ measurements of strain and temperature. Temperature and pressure of the carrier gas are known to have the largest effect on residual strains.	[85]
AA6061	0.5-2	AA6061	4	-30 to -110 MPa	✖	✖	✓	✖	✖	✖	✖	RS was higher for thinner coatings. Compressive stress reduced decreased with increasing coating thickness.	[86]
AA7075	0.282	Mg (AZ31B)	-	C: -10 to -122 MPa S: 0 to 12 MPa	✖	✖	✓	✖	✖	✖	✖	Tensile residual stress on substrate and compressive on coating	[87]

(*continued on next page*)

Table 4 (*continued*)

Coating		Substrate		RS values	Experimental method					AM	FEM	Notes	Ref
Material	Thickness (mm)	Material	Thickness (mm)		XRD	ND	MR	CM	Misc.				
												due to the difference in CTE.	
SS 304L	3.1 ±0.1 2.9 ±0.1	AISI 4130 steel	-	As-sprayed: -3.3 ±0.3 MPa Annealed: -3.7 ±0.3 MPa	✖	✖	✖	✖	✓	✖	✖	Ring-opening tests performed. residual stress for as-sprayed and annealed conditions are presented.	[90]
Cu-Cr-Zr	~3	AISI 4130 steel	-	As-sprayed: 6.9 ±1.0 MPa Annealed: 1.0±0.5 MPa	✖	✖	✖	✖	✓	✖	✖	Ring-opening tests performed. residual stress for as-sprayed and annealed conditions are presented.	[91]
Cu-0.1 Ag	~3	AISI 4130 steel	-	As-sprayed: -2.21 ±0.3 MPa Annealed: -0.3±0.3 MPa	✖	✖	✖	✖	✓	✖	✖	Ring-opening tests performed. residual stress for as-sprayed and annealed conditions are presented.	[92]
Cu-0.1Ag Cu-5.7Ag Cu-23.1Ag	3.3 ±0.1 3.1 ±0.1 3.2 ±0.1 3.2 ±0.1 3.6 ±0.1 3.6 ±0.1	AISI 4130 steel	-	As-sprayed: -2.2 ±0.3 MPa Annealed: -0.3 ±0.3 MPa As-sprayed: -10.6 ±0.3 MPa Annealed: -0.9 ±0.3 MPa As-sprayed: 113.8±0.3 MPa Annealed: -0.4 ±0.3 MPa	✖	✖	✖	✖	✓	✖	✖	Ring opening tests were performed. residual stress for as-sprayed and annealed conditions are presented.	[93]

Table 5
Summary of previously published literature reviews on cold spray.

Author	Year	Paper title	Ref
Yin et al.	2018	Cold spray additive manufacturing and repair: Fundamentals and applications	[5]
Assadi et al.	2016	Cold spraying – A materials perspective	[6]
Rokni et al.	2017	Review of Relationship Between Particle Deformation, Coating Microstructure, and Properties in High-Pressure Cold Spray	[7]
Wu et al.	2012	Advanced cold spray technology: Deposition characteristics and potential applications	[9]
Li et al.	2016	Numerical Analysis of Cold Spray Particles Impacting Behaviour by the Eulerian Method: A Review	[29]
Li et al.	2014	Modelling of impact behaviour of cold spray particles: Review	[45]
Viscusi et al.	2019	A perspective review on the bonding mechanisms in cold gas dynamic spray	[97]
Hussain	2012	Cold Spraying of Titanium: A Review of Bonding Mechanisms, Microstructure and Properties	[98]
Li et al.	2020	Solid-state cold spraying of Ti and its alloys: A literature review	[99]
Olakanmi et al.	2014	Laser-assisted cold-sprayed corrosion- and wear-resistant coatings: A review	[100]
Luo et al.	2014	High velocity impact induced microstructure evolution during deposition of cold spray coatings: A review	[101]
Sun et al.	2020	Post-Process Treatments on Supersonic Cold Sprayed Coatings: A Review	[102]
Pathak et al.	2017	Development of sustainable cold spray coatings and 3D additive manufacturing components for repair/manufacturing applications: A critical review	[247]

Table 6
Material properties of some commonly cold sprayed materials.

Material	Critical velocity (m/s)	Hardness (HV)	Young's modulus (GPa)	Yield strength (MPa)	Melting point (K)	Density (g/cm^3)	Thermal conductivity (W/mK)	Specific heat capacity (J/kgK)	Thermal Diffusivity (mm^2/s)	References
Cu	290	50	110	33	1356	8.9300	385	385	111.98	[126,127,248]
Al	300	15	68	15	933	2.6989	210	900	86.45	[183,249]
Ni	330	65	205	59	1723	8.8900	61	460	14.84	[183,250]
SS316	500	173	197	290	1660	7.9700	15	510	3.69	[4,251]
IN718	490	380	205	550	1571	8.1900	11.4	435	3.20	[183,252]
Fe	350	62	200	50	1809	7.8700	76.2	444	21.81	[183,253]
SS304	395	129	197	215	1700	8.000	16.2	500	4.05	[184,254]
Nb	442	134	105	85	2683	8.4000	53.7	260	24.59	[236,255]
Ti6Al4V	500	349	115	880	1905.5	4.4705	7.2	561	2.87	[184,256]

Industrial Transformation Training Centre project IC180100005 that is titled "Surface Engineering for Advanced Materials", SEAM.

References

[1] A. Papyrin, V. Kosarev, S. Klinkov, A. Alkhimov, V.M. Fomin, Chapter 1 - Discovery of the cold spray phenomenon and its basic features, in: Cold Spray Technol., Elsevier, 2007, pp. 1–32, https://doi.org/10.1016/B978-0-08-045155-8.X5000-5.

[2] W. Li, K. Yang, D. Zhang, X. Zhou, X. Guo, Interface behavior of particles upon impacting during cold spraying of Cu/Ni/Al mixture, Mater. Des. 95 (2016) 237–246, https://doi.org/10.1016/j.matdes.2016.01.122.

[3] Y. Li, X. Wang, S. Yin, S. Xu, Influence of particle initial temperature on high velocity impact process in cold spraying, in: Procedia Environ. Sci., Elsevier, 2012, pp. 298–304, https://doi.org/10.1016/j.proenv.2012.01.281.

[4] B. Yildirim, H. Fukanuma, T. Ando, A. Gouldstone, S. Müftü, A numerical investigation into cold spray bonding processes, J. Tribol. 137 (2014) 011102, https://doi.org/10.1115/1.4028471.

[5] S. Yin, P. Cavaliere, B. Aldwell, R. Jenkins, H. Liao, W. Li, R. Lupoi, Cold spray additive manufacturing and repair: Fundamentals and applications, Addit. Manuf. 21 (2018) 628–650, https://doi.org/10.1016/j.addma.2018.04.017.

[6] H. Assadi, H. Kreye, F. Gärtner, T. Klassen, Cold spraying – a materials perspective, Acta Mater. 116 (2016) 382–407, https://doi.org/10.1016/j.actamat.2016.06.034.

[7] M.R. Rokni, S.R. Nutt, C.A. Widener, V.K. Champagne, R.H. Hrabe, Review of relationship between particle deformation, coating microstructure, and properties in high-pressure cold spray, J. Therm. Spray Technol. 26 (2017) 1308–1355, https://doi.org/10.1007/s11666-017-0575-0.

[8] M.R. Rokni, C.A. Widener, S.P. Ahrenkiel, B.K. Jasthi, V.R. Champagne, Annealing behaviour of 6061 Aluminium deposited by high pressure cold spray, Surf. Eng. 30 (2014) 361–368, https://doi.org/10.1179/1743294413Y.0000000209.

[9] X. Wu, J. Zhang, X. Zhou, H. Cui, J. Liu, Advanced cold spray technology: Deposition characteristics and potential applications, Sci. China Technol. Sci. 55 (2012) 357–368, https://doi.org/10.1007/s11431-011-4673-9.

[10] V. Champagne, D. Helfritch, The unique abilities of cold spray deposition, Int. Mater. Rev. 61 (2016) 437–455, https://doi.org/10.1080/09506608.2016.1194948.

[11] A.M. Vilardell, N. Cinca, A. Concustell, S. Dosta, I.G. Cano, J.M. Guilemany, Cold spray as an emerging technology for biocompatible and antibacterial coatings: state of art, J. Mater. Sci. 50 (2015) 4441–4462, https://doi.org/10.1007/s10853-015-9013-1.

[12] V.K. Champagne, D.J. Helfritch, Mainstreaming cold spray - push for applications, Surf. Eng. 30 (2014) 396–403, https://doi.org/10.1179/1743294414Y.0000000277.

[13] C.-J. Li, W.-Y. Li, H. Liao, Examination of the critical velocity for deposition of particles in cold spraying, J. Therm. Spray Technol. 15 (2006) 212–222, https://doi.org/10.1361/105996306X108093.

[14] G. Bae, Y. Xiong, S. Kumar, K. Kang, C. Lee, General aspects of interface bonding in kinetic sprayed coatings, Acta Mater. 56 (2008) 4858–4868, https://doi.org/10.1016/j.actamat.2008.06.003.

[15] H. Assadi, F. Gärtner, T. Stoltenhoff, H. Kreye, Bonding mechanism in cold gas spraying, Acta Mater. 51 (2003) 4379–4394, https://doi.org/10.1016/S1359-6454(03)00274-X.

[16] T. Schmidt, F. Gärtner, H. Assadi, H. Kreye, Development of a generalized parameter window for cold spray deposition, Acta Mater. 54 (2006) 729–742, https://doi.org/10.1016/j.actamat.2005.10.005.

[17] B. Dodd, Y. Bai, 1 - Introduction, in: Adiabatic Shear Localization, 2nd ed., Elsevier, 2012, pp. 1–20, https://doi.org/10.1016/B978-0-08-097781-2.00001-0.

[18] M. Hassani-Gangaraj, D. Veysset, V. Kenneth, C. Jr, C.A. Schuh, Adiabatic shear instability is not necessary for adhesion in cold spray, Acta Mater. 158 (2018) 430–439, https://doi.org/10.1016/j.actamat.2018.07.065.

[19] J. Lienhard, C. Crook, M.Z. Azar, M. Hassani, D.R. Mumm, D. Veysset, D. Apelian, K.A. Nelson, V. Champagne, A. Nardi, C.A. Schuh, L. Valdevit, Surface oxide and hydroxide effects on aluminum microparticle impact bonding, Acta Mater. 197 (2020) 28–39, https://doi.org/10.1016/j.actamat.2020.07.011.

[20] S.V. Klinkov, V.F. Kosarev, M. Rein, Cold spray deposition: Significance of particle impact phenomena, Aerosp. Sci. Technol. 9 (2005) 582–591, https://doi.org/10.1016/j.ast.2005.03.005.

[21] H. Assadi, F. Gärtner, T. Klassen, H. Kreye, Comment on 'Adiabatic shear instability is not necessary for adhesion in cold spray', Scr. Mater. 162 (2019) 512–514, https://doi.org/10.1016/j.scriptamat.2018.10.036.

[22] M. Hassani-Gangaraj, D. Veysset, V.K. Champagne, K.A. Nelson, C.A. Schuh, Response to Comment on "Adiabatic shear instability is not necessary for adhesion in cold spray", Scr. Mater. 162 (2019) 515–519. https://doi.org/10.1016/j.scriptamat.2018.12.015.

[23] R. Ghelichi, D. MacDonald, S. Bagherifard, H. Jahed, M. Guagliano, B. Jodoin, Microstructure and fatigue behavior of cold spray coated Al5052, Acta Mater. 60 (2012) 6555–6561, https://doi.org/10.1016/j.actamat.2012.08.020.

[24] M. Grujicic, J.R. Saylor, D.E. Beasley, W.S. DeRosset, D. Helfritch, Computational analysis of the interfacial bonding between feed-powder particles and the substrate in the cold-gas dynamic-spray process, Appl. Surf. Sci. 219 (2003) 211–227, https://doi.org/10.1016/S0169-4332(03)00643-3.

[25] W.-Y. Li, W. Gao, Some aspects on 3D numerical modeling of high velocity impact of particles in cold spraying by explicit finite element analysis, Appl. Surf. Sci. 255 (2009) 7878–7892, https://doi.org/10.1016/j.apsusc.2009.04.135.

[26] B. Gnanasekaran, G.-R. Liu, Y. Fu, G. Wang, W. Niu, T. Lin, A Smoothed Particle Hydrodynamics (SPH) procedure for simulating cold spray process - a study using particles, Surf. Coat. Technol. 377 (2019) 1–23, https://doi.org/10.1016/j.surfcoat.2019.07.036.

[27] W.Y. Li, H. Liao, C.J. Li, G. Li, C. Coddet, X. Wang, On high velocity impact of micro-sized metallic particles in cold spraying, Appl. Surf. Sci. 253 (2006) 2852–2862, https://doi.org/10.1016/j.apsusc.2006.05.126.

[28] S. Yin, X.F. Wang, W.Y. Li, B.P. Xu, Numerical investigation on effects of interactions between particles on coating formation in cold spraying, J. Therm. Spray Technol. 18 (2009) 686–693, https://doi.org/10.1007/s11666-009-9390-6.

[29] W.Y. Li, K. Yang, S. Yin, X.P. Guo, Numerical analysis of cold spray particles impacting behavior by the eulerian method: a review, J. Therm. Spray Technol. 25 (2016) 1441–1460, https://doi.org/10.1007/s11666-016-0443-3.

[30] S. Rahmati, A. Zúñiga, B. Jodoin, R.G.A. Veiga, Deformation of copper particles upon impact: a molecular dynamics study of cold spray, Comput. Mater. Sci. 171 (2020) 109219, https://doi.org/10.1016/j.commatsci.2019.109219.

[31] J. Xie, D. Nelias, H. Walter-Le Berre, Y. Ichikawa, K. Ogawa, Numerical simulation of the cold spray deposition process for aluminium and copper, in: ASME 2012 11th Bienn. Conf. Eng. Syst. Des. Anal. ESDA 2012, ASME, 2012, pp. 109–111, https://doi.org/10.1115/ESDA2012-82107.

[32] P.C. King, G. Bae, S.H. Zahiri, M. Jahedi, C. Lee, An experimental and finite element study of cold spray copper impact onto two aluminum substrates, J. Therm. Spray Technol. 19 (2010) 620–634, https://doi.org/10.1007/s11666-009-9454-7.

[33] J. Xie, D. Nélias, H.W. Le Berre, K. Ogawa, Y. Ichikawa, Simulation of the cold spray particle deposition process, J. Tribol. 137 (2015) 041101, https://doi.org/10.1115/1.4030257.

[34] S. Rahmati, B. Jodoin, Physically based finite element modeling method to predict metallic bonding in cold spray, J. Therm. Spray Technol. 29 (2020) 611–629, https://doi.org/10.1007/s11666-020-01000-1.

[35] F. Wang, Deposition characteristic of Al particles on Mg alloy micro-channel substrate by cold spray, Int. J. Adv. Manuf. Technol. 91 (2017) 791–802, https://doi.org/10.1007/s00170-016-9807-6.

[36] F. Delloro, M. Jeandin, D. Jeulin, H. Proudhon, M. Faessel, L. Bianchi, E. Meillot, L. Helfen, A morphological approach to the modeling of the cold spray process, J. Therm. Spray Technol. 26 (2017) 1838–1850, https://doi.org/10.1007/s11666-017-0624-8.

[37] Dassault Systems, Abaqus analysis user's guide, in: Abaqus Online Doc., 2016. http://50.16.225.63/v2016/. (Accessed 19 November 2020).

[38] A. Manap, T. Okabe, K. Ogawa, S. Mahalingam, H. Abdullah, Experimental and smoothed particle hydrodynamics analysis of interfacial bonding between aluminum powder particles and aluminum substrate by cold spray technique, Int. J. Adv. Manuf. Technol. 103 (2019) 4519–4527, https://doi.org/10.1007/s00170-019-03846-4.

[39] W.Y. Li, S. Yin, X.F. Wang, Numerical investigations of the effect of oblique impact on particle deformation in cold spraying by the SPH method, Appl. Surf. Sci. 256 (2010) 3725–3734, https://doi.org/10.1016/j.apsusc.2010.01.014.
[40] A. Manap, T. Okabe, K. Ogawa, Computer simulation of cold sprayed deposition using smoothed particle hydrodynamics, Procedia Eng. 10 (2011) 1145–1150, https://doi.org/10.1016/j.proeng.2011.04.190.
[41] A. Manap, K. Ogawa, T. Okabe, Numerical analysis of interfacial bonding of al-si particle and mild steel substrate by cold spray technique using the SPH method, J. Solid Mech. Mater. Eng. 6 (2012) 241–250, https://doi.org/10.1299/jmmp.6.241.
[42] S. Suresh, S.W. Lee, M. Aindow, H.D. Brody, V.K. Champagne, A.M. Dongare, Mesoscale modeling of jet initiation behavior and microstructural evolution during cold spray single particle impact, Acta Mater. 182 (2020) 197–206, https://doi.org/10.1016/j.actamat.2019.10.039.
[43] S. Suresh, S.W. Lee, M. Aindow, H.D. Brody, V.K. Champagne, A.M. Dongare, Unraveling the mesoscale evolution of microstructure during supersonic impact of aluminum powder particles, Sci. Rep. 8 (2018) 1–13, https://doi.org/10.1038/s41598-018-28437-3.
[44] A. Moridi, Powder Consolidation Using Cold Spray: Process Modeling and Emerging Applications, 2017, https://doi.org/10.1007/978-3-319-29962-4.
[45] W.Y. Li, D.D. Zhang, C.J. Huang, S. Yin, M. Yu, F.F. Wang, H.L. Liao, Modelling of impact behaviour of cold spray particles: review, Surf. Eng. 30 (2014) 299–308, https://doi.org/10.1179/1743294414Y.0000000268.
[46] A.A. Abubakar, A.F.M. Arif, K.S. Al-Athel, S.S. Akhtar, J. Mostaghimi, Modeling residual stress development in thermal spray coatings: current status and way forward, J. Therm. Spray Technol. 26 (2017) 1115–1145, https://doi.org/10.1007/s11666-017-0590-1.
[47] A. Fardan, R. Ahmed, Modeling the evolution of residual stresses in thermally sprayed YSZ coating on stainless steel substrate, J. Therm. Spray Technol. 28 (2019) 717–736, https://doi.org/10.1007/s11666-019-00856-2.
[48] R. Ghelichi, S. Bagherifard, D. Macdonald, I. Fernandez-Pariente, B. Jodoin, M. Guagliano, Experimental and numerical study of residual stress evolution in cold spray coating, Appl. Surf. Sci. 288 (2014) 26–33, https://doi.org/10.1016/j.apsusc.2013.09.074.
[49] T. Suhonen, T. Varis, S. Dosta, M. Torrell, J.M. Guilemany, Residual stress development in cold sprayed Al, Cu and Ti coatings, Acta Mater. 61 (2013) 6329–6337, https://doi.org/10.1016/j.actamat.2013.06.033.
[50] B.C. White, W.A. Story, L.N. Brewer, J.B. Jordon, Fracture mechanics methods for evaluating the adhesion of cold spray deposits, Eng. Fract. Mech. 205 (2019) 57–69, https://doi.org/10.1016/j.engfracmech.2018.11.009.
[51] K. Petráčková, J. Kondás, M. Guagliano, Mechanical performance of cold-sprayed A357 aluminum alloy coatings for repair and additive manufacturing, J. Therm. Spray Technol. 26 (2017) 1888–1897, https://doi.org/10.1007/s11666-017-0643-5.
[52] R. Ghelichi, S. Bagherifard, D. Mac Donald, M. Brochu, H. Jahed, B. Jodoin, M. Guagliano, Fatigue strength of Al alloy cold sprayed with nanocrystalline powders, Int. J. Fatigue 65 (2014) 51–57, https://doi.org/10.1016/j.ijfatigue.2013.09.001.
[53] J. Cizek, M. Matejkova, I. Dlouhy, F. Siska, C.M. Kay, J. Karthikeyan, S. Kuroda, O. Kovarik, J. Siegl, K. Loke, K.A. Khor, Influence of cold-sprayed, warm-sprayed, and plasma-sprayed layers deposition on fatigue properties of steel specimens, J. Therm. Spray Technol. 24 (2015) 758–768, https://doi.org/10.1007/s11666-015-0240-4.
[54] A. Valarezo, S. Sampath, An integrated assessment of process-microstructure-property relationships for thermal-sprayed NiCr coatings, J. Therm. Spray Technol. 20 (2011) 1244–1258, https://doi.org/10.1007/s11666-011-9665-6.
[55] R. Ahmed, H. Yu, V. Stoica, L. Edwards, J.R. Santisteban, Neutron diffraction residual strain measurements in post-treated thermal spray cermet coatings, Mater. Sci. Eng. A 498 (2008) 191–202, https://doi.org/10.1016/j.msea.2008.08.023.
[56] A.S.M. Ang, C.C. Berndt, A review of testing methods for thermal spray coatings, Int. Mater. Rev. 59 (2014) 179–223, https://doi.org/10.1179/1743280414Y.0000000029.
[57] W. Li, K. Yang, D. Zhang, X. Zhou, Residual stress analysis of cold-sprayed copper coatings by numerical simulation, J. Therm. Spray Technol. 25 (2016) 131–142, https://doi.org/10.1007/s11666-015-0308-1.
[58] X. Qiu, N. ul H. Tariq, L. Qi, J.R. Tang, X.Y. Cui, H. Du, J.Q. Wang, T.Y. Xiong, Effects of dissimilar alumina particulates on microstructure and properties of cold-sprayed alumina/a380 composite coatings, Acta Metall. Sin. 32 (2019) 1449–1458, https://doi.org/10.1007/s40195-019-00917-z. English Lett.
[59] L.I. Pérez-Andrade, F. Gärtner, M. Villa-Vidaller, T. Klassen, J. Muñoz-Saldaña, J. M. Alvarado-Orozco, Optimization of Inconel 718 thick deposits by cold spray processing and annealing, Surf. Coat. Technol. 378 (2019) 124997, https://doi.org/10.1016/j.surfcoat.2019.124997.
[60] R. Vaßen, J. Fiebig, T. Kalfhaus, J. Gibmeier, A. Kostka, S. Schrüfer, Correlation of microstructure and properties of cold gas sprayed INCONEL 718 coatings, J. Therm. Spray Technol. (2020), https://doi.org/10.1007/s11666-020-00988-w.
[61] M.R. Rokni, C.A. Widener, O.C. Ozdemir, G.A. Crawford, Microstructure and mechanical properties of cold sprayed 6061 Al in As-sprayed and heat treated condition, Surf. Coat. Technol. 309 (2017) 641–650, https://doi.org/10.1016/j.surfcoat.2016.12.035.
[62] S. Rech, A. Trentin, S. Vezzù, J.G. Legoux, E. Irissou, M. Guagliano, Influence of pre-heated Al 6061 substrate temperature on the residual stresses of multipass Al coatings deposited by cold spray, J. Therm. Spray Technol. 20 (2011) 243–251, https://doi.org/10.1007/s11666-010-9596-7.
[63] B. Hunter, B. Aldwell, R. Jenkins, R. Lupoi, A study on the feasibility of laser annealing to relieve residual stresses in cold spray coatings, Procedia CIRP 78 (2018) 91–96, https://doi.org/10.1016/j.procir.2018.08.170.
[64] S. Bagherifard, G. Roscioli, M.V. Zuccoli, M. Hadi, G. D'Elia, A.G. Demir, B. Previtali, J. Kondás, M. Guagliano, Cold spray deposition of freestanding inconel samples and comparative analysis with selective laser melting, J. Therm. Spray Technol. 26 (2017) 1517–1526, https://doi.org/10.1007/s11666-017-0572-3.
[65] V. Luzin, O. Kirstein, S.H. Zahiri, D. Fraser, Residual Stress Buildup in Ti Components Produced by Cold Spray Additive Manufacturing (CSAM), J. Therm. Spray Technol. (2020), https://doi.org/10.1007/s11666-020-01048-z.
[66] R. Sinclair-Adamson, V. Luzin, A. Duguid, K. Kannoorpatti, R. Murray, Residual Stress Distributions in Cold-Sprayed Copper 3D-Printed Parts, J. Therm. Spray Technol. (2020), https://doi.org/10.1007/s11666-020-01040-7.
[67] N.B. Maledi, O.P. Oladijo, I. Botef, T.P. Ntsoane, A. Madiseng, L. Moloisane, Influence of cold spray parameters on the microstructures and residual stress of Zn coatings sprayed on mild steel, Surf. Coat. Technol. 318 (2017) 106–113, https://doi.org/10.1016/j.surfcoat.2017.03.062.
[68] K. Bobzin, W. Wietheger, M.A. Knoch, A. Schacht, U. Reisgen, R. Sharma, L. Oster, Comparison of residual stress measurements conducted by X-ray stress analysis and incremental hole drilling method, J. Therm. Spray Technol. (2020), https://doi.org/10.1007/s11666-020-01056-z.
[69] D. Boruah, X. Zhang, M. Doré, Theoretical prediction of residual stresses induced by cold spray with experimental validation, Multidiscip. Model. Mater. Struct. 15 (2019) 599–616, https://doi.org/10.1108/MMMS-08-2018-0150.
[70] K. Spencer, V. Luzin, N. Matthews, M.X. Zhang, Residual stresses in cold spray Al coatings: The effect of alloying and of process parameters, Surf. Coat. Technol. 206 (2012) 4249–4255, https://doi.org/10.1016/j.surfcoat.2012.04.034.
[71] D. Boruah, B. Ahmad, T.L. Lee, S. Kabra, A.K. Syed, P. McNutt, M. Doré, X. Zhang, Evaluation of residual stresses induced by cold spraying of Ti-6Al-4V on Ti-6Al-4V substrates, Surf. Coat. Technol. 374 (2019) 591–602, https://doi.org/10.1016/j.surfcoat.2019.06.028.
[72] A. Vargas-Uscategui, P.C. King, M.J. Styles, M. Saleh, V. Luzin, K. Thorogood, Residual stresses in cold spray additively manufactured hollow titanium cylinders, J. Therm. Spray Technol. (2020), https://doi.org/10.1007/s11666-020-01028-3.
[73] K. Spencer, V. Luzin, M. Zhang, Structure and properties of cold spray coatings, Mater. Sci. Forum 654–656 (2010) 1880–1883 (doi:10.4028/www.scientific.net/MSF.654-656.1880).
[74] V. Luzin, A. Valarezo, S. Sampath, Through-thickness residual stress measurement in metal and ceramic spray coatings by neutron diffraction, Mater. Sci. Forum 571–572 (2008) 315–320 (doi:10.4028/www.scientific.net/msf.571-572.315).
[75] V. Luzin, K. Spencer, M.-X. Zhang, Residual stress and thermo-mechanical properties of cold spray metal coatings, Acta Mater. 59 (2011) 1259–1270, https://doi.org/10.1016/j.actamat.2010.10.058.
[76] R. Ahmed, N.H. Faisal, A.M. Paradowska, M.E. Fitzpatrick, Residual strain and fracture response of Al 2O 3 coatings deposited via APS and HVOF techniques, J. Therm. Spray Technol. 21 (2012) 23–40, https://doi.org/10.1007/s11666-011-9680-7.
[77] R. Ahmed, N.H. Faisal, A.M. Paradowska, M.E. Fitzpatrick, K.A. Khor, Neutron diffraction residual strain measurements in nanostructured hydroxyapatite coatings for orthopaedic implants, J. Mech. Behav. Biomed. Mater. 4 (2011) 2043–2054, https://doi.org/10.1016/j.jmbbm.2011.07.003.
[78] N.H. Faisal, R. Ahmed, A.K. Prathuru, S.P. Katikaneni, M.F.A. Goosen, S.Y. Zhang, Neutron diffraction residual strain measurements of molybdenum carbide-based solid oxide fuel cell anode layers with metal oxides on Hastelloy X, Exp. Mech. 58 (2018) 585–603, https://doi.org/10.1007/s11340-017-0298-7.
[79] R. Ahmed, M.E. Fitzpatrick, N.H. Faisal, A comparison of neutron diffraction and hole-drilling residual strain measurements in thermally sprayed coatings, Surf. Coat. Technol. 206 (2012) 4180–4185, https://doi.org/10.1016/j.surfcoat.2012.04.018.
[80] V. Luzin, K. Spencer, M. Zhang, N. Matthews, J. Davis, M. Saleh, Residual Stresses in Cold Spray Coatings, in: P. Cavaliere (Ed.), Cold-Spray Coatings Recent Trends Futur. Perspect., Springer International Publishing, Cham, 2018, pp. 451–480, https://doi.org/10.1007/978-3-319-67183-3_16.
[81] M. Saleh, V. Luzin, K. Spencer, Analysis of the residual stress and bonding mechanism in the cold spray technique using experimental and numerical methods, Surf. Coat. Technol. 252 (2014) 15–28, https://doi.org/10.1016/j.surfcoat.2014.04.059.
[82] M. Saleh, V. Luzin, K. Spencer, Evaluation of the residual stress in the cold spray technique using Smooth Particle Hyrodynamics modelling and neutron diffraction, Mater. Sci. Forum 777 (2014) 205–212 (doi:10.4028/www.scientific.net/MSF.777.205).
[83] R. Singh, S. Schruefer, S. Wilson, J. Gibmeier, R. Vassen, Influence of coating thickness on residual stress and adhesion-strength of cold-sprayed Inconel 718 coatings, Surf. Coat. Technol. 350 (2018) 64–73, https://doi.org/10.1016/j.surfcoat.2018.06.080.
[84] A. Ryabchikov, H. Lille, S. Toropov, J. Kõo, T. Pihl, R. Veinthal, Determination of residual stresses in thermal and cold sprayed coatings by the hole-drilling method, Mater. Sci. Forum 681 (2011) 171–176 (doi:10.4028/www.scientific.net/MSF.681.171).
[85] B. Marzbanrad, H. Jahed, E. Toyserkani, On the evolution of substrate's residual stress during cold spray process: a parametric study, Mater. Des. 138 (2018) 90–102, https://doi.org/10.1016/j.matdes.2017.10.062.

[86] S. Rech, A. Trentin, S. Vezzù, E. Vedelago, J.G. Legoux, E. Irissou, Different cold spray deposition strategies: single- and multi-layers to repair aluminium alloy components, J. Therm. Spray Technol. 23 (2014) 1237–1250, https://doi.org/10.1007/s11666-014-0141-y.
[87] S.B. Dayani, S.K. Shaha, R. Ghelichi, J.F. Wang, H. Jahed, The impact of AA7075 cold spray coating on the fatigue life of AZ31B cast alloy, Surf. Coat. Technol. 337 (2018) 150–158, https://doi.org/10.1016/j.surfcoat.2018.01.008.
[88] X. Song, J. Everaerts, W. Zhai, H. Zheng, A.W.Y. Tan, W. Sun, F. Li, I. Marinescu, E. Liu, A.M. Korsunsky, Residual stresses in single particle splat of metal cold spray process – numerical simulation and direct measurement, Mater. Lett. 230 (2018) 152–156, https://doi.org/10.1016/j.matlet.2018.07.117.
[89] N.H. Faisal, L. Mann, C. Duncan, E. Dunbar, M. Clayton, M. Frost, J. McConnachie, A. Fardan, R. Ahmed, Diametral compression test method to analyse relative surface stresses in thermally sprayed coated and uncoated circular disc specimens, Surf. Coat. Technol. (2019), https://doi.org/10.1016/j.surfcoat.2018.10.053.
[90] P. Coddet, C. Verdy, C. Coddet, F. Debray, F. Lecouturier, Mechanical properties of thick 304L stainless steel deposits processed by He cold spray, Surf. Coat. Technol. 277 (2015) 74–80, https://doi.org/10.1016/j.surfcoat.2015.07.001.
[91] P. Coddet, C. Verdy, C. Coddet, F. Lecouturier, F. Debray, Comparison of the properties of cold-sprayed Cu-0.5Cr-0.05Zr alloys after various heat treatments versus forged and vacuum plasma-sprayed alloys, J. Therm. Spray Technol. 23 (2014) 486–491, https://doi.org/10.1007/s11666-013-0028-3.
[92] P. Coddet, C. Verdy, C. Coddet, F. Debray, Mechanical properties of Cu-0.1Ag alloys deposited by cold spray with various powder feed rate and heat treatment, J. Therm. Spray Technol. 24 (2014) 119–125, https://doi.org/10.1007/s11666-014-0159-1.
[93] P. Coddet, C. Verdy, C. Coddet, F. Debray, Effect of cold work, second phase precipitation and heat treatments on the mechanical properties of copper–silver alloys manufactured by cold spray, Mater. Sci. Eng. A 637 (2015) 40–47, https://doi.org/10.1016/j.msea.2015.04.008.
[94] L.N. Zhu, B.S. Xu, H.D. Wang, C.B. Wang, Measurement of residual stresses using nanoindentation method, Crit. Rev. Solid State Mater. Sci. 40 (2015) 77–89, https://doi.org/10.1080/10408436.2014.940442.
[95] Z. Arabgol, H. Assadi, T. Schmidt, F. Gärtner, T. Klassen, Analysis of thermal history and residual stress in cold-sprayed coatings, J. Therm. Spray Technol. 23 (2014) 84–90, https://doi.org/10.1007/s11666-013-9976-x.
[96] Z. Zhu, S. Kamnis, S. Gu, Numerical study of molten and semi-molten ceramic impingement by using coupled Eulerian and Lagrangian method, Acta Mater. 90 (2015) 77–87, https://doi.org/10.1016/j.actamat.2015.02.010.
[97] A. Viscusi, A. Astarita, R. Della Gatta, F. Rubino, A perspective review on the bonding mechanisms in cold gas dynamic spray, Surf. Eng. 35 (2019) 743–771, https://doi.org/10.1080/02670844.2018.1551768.
[98] T. Hussain, Cold Spraying of Titanium: A Review of Bonding Mechanisms, Microstructure and Properties, Key Eng. Mater. 533 (2012) 53–90 (doi:10.4028/www.scientific.net/kem.533.53).
[99] W. Li, C. Cao, S. Yin, Solid-state cold spraying of Ti and its alloys: a literature review, Prog. Mater. Sci. 110 (2020) 100633, https://doi.org/10.1016/j.pmatsci.2019.100633.
[100] E.O. Olakanmi, M. Doyoyo, Laser-assisted cold-sprayed corrosion- and wear-resistant coatings: a review, J. Therm. Spray Technol. 23 (2014) 765–785, https://doi.org/10.1007/s11666-014-0098-x.
[101] X.T. Luo, C.X. Li, F.L. Shang, G.J. Yang, Y.Y. Wang, C.J. Li, High velocity impact induced microstructure evolution during deposition of cold spray coatings: a review, Surf. Coat. Technol. 254 (2014) 11–20, https://doi.org/10.1016/j.surfcoat.2014.06.006.
[102] W. Sun, A.W.Y. Tan, K. Wu, S. Yin, X. Yang, I. Marinescu, E. Liu, Post-process treatments on supersonic cold sprayed coatings: a review, Coatings 10 (2020) 123, https://doi.org/10.3390/coatings10020123.
[103] M. Grujicic, C.L. Zhao, W.S. DeRosset, D. Helfritch, Adiabatic shear instability based mechanism for particles/substrate bonding in the cold-gas dynamic-spray process, Mater. Des. 25 (2004) 681–688, https://doi.org/10.1016/j.matdes.2004.03.008.
[104] P. Landau, S. Osovski, A. Venkert, V. Gärtnerová, D. Rittel, The genesis of adiabatic shear bands, Sci. Rep. 6 (2016) 37226, https://doi.org/10.1038/srep37226.
[105] G. Mie, Zur kinetischen Theorie der einatomigen Korper, Ann. Phys. 316 (1903) 657–697, https://doi.org/10.1002/andp.19033160802.
[106] K.-M. Shyue, A fluid-mixture type algorithm for compressible multicomponent flow with mie–Grüneisen equation of state, J. Comput. Phys. 171 (2001) 678–707, https://doi.org/10.1006/jcph.2001.6801.
[107] M.H. Rice, R.G. McQueen, J.M. Walsh, Compression of Solids by Strong Shock Waves, Solid State Phys. - Adv. Res. Appl. 6 (1958) 1–63, https://doi.org/10.1016/S0081-1947(08)60724-9.
[108] Mark L. Wilkins, Compter Simulation of Dynamic Phenomena, Springer, Berlin, 1999, https://doi.org/10.1007/978-3-662-03885-7.
[109] A.L. Ruoff, Linear shock-velocity-particle-velocity relationship, J. Appl. Phys. 38 (1967) 4976–4980, https://doi.org/10.1063/1.1709263.
[110] N. Nishiyama, K. Fujii, E. Kulik, M. Shiraiwa, N.A. Gaida, Y. Higo, Y. Tange, A. Holzheid, M. Yashima, F. Wakai, Thermal expansion and P-V-T equation of state of cubic silicon nitride, J. Eur. Ceram. Soc. 39 (2019) 3627–3633, https://doi.org/10.1016/j.jeurceramsoc.2019.05.003.
[111] M.I. Katsnelson, M. Sigalas, A.V. Trefilov, K.Y. Khromov, Thermal expansion and the equation of state of Ir and Rh, Philos. Mag. B 75 (1997) 407–418, https://doi.org/10.1080/13642819708202327.
[112] G.R. Johnson, W.H. Cook, Fracture characteristics of three metals subjected to various strains, strain rates, temperatures and pressures, Eng. Fract. Mech. 21 (1985) 31–48, https://doi.org/10.1016/0013-7944(85)90052-9.
[113] G.R. Johnson, W.H. Cook, A constitutive model and data for metals subjected to large strains, high strain rates and high temperatures, in: 7th Int. Symp. Ballist., 1983, pp. 541–547, https://doi.org/10.1038/nrm3209.
[114] D.L. Preston, D.L. Tonks, D.C. Wallace, Model of plastic deformation for extreme loading conditions, J. Appl. Phys. 93 (2003) 211–220, https://doi.org/10.1063/1.1524706.
[115] Y. Cormier, P. Dupuis, B. Jodoin, A. Ghaei, Finite element analysis and failure mode characterization of pyramidal fin arrays produced by masked cold gas dynamic spray, J. Therm. Spray Technol. 24 (2015) 1549–1565, https://doi.org/10.1007/s11666-015-0317-0.
[116] B. Banerjee, The Mechanical Threshold Stress model for various tempers of AISI 4340 steel, Int. J. Solids Struct. 44 (2007) 834–859, https://doi.org/10.1016/j.ijsolstr.2006.05.022.
[117] B. Zhang, V.P.W. Shim, Effect of strain rate on microstructure of polycrystalline oxygen-free high conductivity copper severely deformed at liquid nitrogen temperature, Acta Mater. 58 (2010) 6810–6827, https://doi.org/10.1016/j.actamat.2010.09.009.
[118] J. Henao, G. Bolelli, A. Concustell, L. Lusvarghi, S. Dosta, I.G. Cano, J. M. Guilemany, Deposition behavior of cold-sprayed metallic glass particles onto different substrates, Surf. Coat. Technol. 349 (2018) 13–23, https://doi.org/10.1016/j.surfcoat.2018.05.047.
[119] F.H. Abed, G.Z. Voyiadjis, A consistent modified Zerilli-Armstrong flow stress model for BCC and FCC metals for elevated temperatures, Acta Mech. 175 (2005) 1–18, https://doi.org/10.1007/s00707-004-0203-1.
[120] A.K. Gupta, V.K. Anirudh, S.K. Singh, Constitutive models to predict flow stress in Austenitic Stainless Steel 316 at elevated temperatures, Mater. Des. 43 (2013) 410–418, https://doi.org/10.1016/j.matdes.2012.07.008.
[121] W.-Y. Li, C. Zhang, C.-J. Li, H. Liao, Modeling aspects of high velocity impact of particles in cold spraying by explicit finite element analysis, J. Therm. Spray Technol. 18 (2009) 921–933, https://doi.org/10.1007/s11666-009-9325-2.
[122] B. Yildirim, S. Muftu, A. Gouldstone, Modeling of high velocity impact of spherical particles, Wear 270 (2011) 703–713, https://doi.org/10.1016/j.wear.2011.02.003.
[123] D. Nélias, J. Xie, H. Walter-Le Berre, Y. Ichikawa, K. Ogawa, Simulation of the cold spray deposition process for aluminum and copper using Lagrangian, ALE and CEL methods, in: J. Bergheau (Ed.), Thermomechanical Ind. Process. Model. Numer. Simul., 1st ed., Wiley Online Library, 2014, pp. 321–358, https://doi.org/10.1002/9781118578759.ch7.
[124] W.Y. Li, H. Liao, C.J. Li, H.S. Bang, C. Coddet, Numerical simulation of deformation behavior of Al particles impacting on Al substrate and effect of surface oxide films on interfacial bonding in cold spraying, Appl. Surf. Sci. 253 (2007) 5084–5091, https://doi.org/10.1016/j.apsusc.2006.11.020.
[125] C.J. Li, W.Y. Li, Deposition characteristics of titanium coating in cold spraying, Surf. Coat. Technol. 167 (2003) 278–283, https://doi.org/10.1016/S0257-8972(02)00919-2.
[126] M. Yu, W.Y. Li, F.F. Wang, H.L. Liao, Finite element simulation of impacting behavior of particles in cold spraying by Eulerian approach, J. Therm. Spray Technol. 21 (2012) 745–752, https://doi.org/10.1007/s11666-011-9717-y.
[127] M. Yu, W.Y. Li, F.F. Wang, X.K. Suo, H.L. Liao, Effect of particle and substrate preheating on particle deformation behavior in cold spraying, Surf. Coat. Technol. 220 (2013) 174–178, https://doi.org/10.1016/j.surfcoat.2012.04.081.
[128] S. Yin, X.F. Wang, B.P. Xu, W.Y. Li, Examination on the calculation method for modeling the multi-particle impact process in cold spraying, J. Therm. Spray Technol. 19 (2010) 1032–1041, https://doi.org/10.1007/s11666-010-9489-9.
[129] T. Schmidt, H. Assadi, F. Gärtner, H. Richter, T. Stoltenhoff, H. Kreye, T. Klassen, From particle acceleration to impact and bonding in cold spraying, J. Therm. Spray Technol. 18 (2009) 794–808, https://doi.org/10.1007/s11666-009-9357-7.
[130] L.H. Li, Yu Min Wenya, Wu Hui, Effect of Mesh Resolution on the Particle Deformation during Cold Spraying by Eulerian Formulation, Rare Metal Mater. Eng. 41 (2012) 327–330.
[131] Y.C. Chang, T.Y. Hou, B. Merriman, S. Osher, A level set formulation of Eulerian interface capturing methods for incompressible fluid flows, J. Comput. Phys. 124 (1996) 449–464, https://doi.org/10.1006/jcph.1996.0072.
[132] N. Balcázar, O. Lehmkuhl, J. Rigola, A. Oliva, A multiple marker level-set method for simulation of deformable fluid particles, Int. J. Multiphase Flow 74 (2015) 125–142, https://doi.org/10.1016/j.ijmultiphaseflow.2015.04.009.
[133] P. He, R. Qiao, A full-Eulerian solid level set method for simulation of fluid-structure interactions, Microfluid. Nanofluid. 11 (2011) 557–567, https://doi.org/10.1007/s10404-011-0821-6.
[134] A. Mühlbauer, M.W. Hlawitschka, H.J. Bart, Models for the numerical simulation of bubble columns: a review, Chemie-Ingenieur-Technik. 91 (2019) 1747–1765, https://doi.org/10.1002/cite.201900109.
[135] M. Van Sint Annaland, N.G. Deen, J.A.M. Kuipers, Numerical simulation of gas bubbles behaviour using a three-dimensional volume of fluid method, Chem. Eng. Sci. 60 (2005) 2999–3011, https://doi.org/10.1016/j.ces.2005.01.031.
[136] A. Manap, O. Nooririnah, H. Misran, T. Okabe, K. Ogawa, Experimental and SPH study of cold spray impact between similar and dissimilar metals, Surf. Eng. 30 (2014) 335–341, https://doi.org/10.1179/1743294413Y.0000000237.
[137] Dassault Systems, Smoothed particle hydrodynamics, in: Abaqus Anal. User's Guid., 2016. http://130.149.89.49:2080/v2016/books/usb/default.htm?startat=pt04ch15s02aus96.html. (Accessed 19 November 2020).

[138] M. Hassani-Gangaraj, D. Veysset, K.A. Nelson, C.A. Schuh, In-situ observations of single micro-particle impact bonding, Scr. Mater. 145 (2018) 9–13, https://doi.org/10.1016/j.scriptamat.2017.09.042.
[139] G. Bolelli, S. Dosta, L. Lusvarghi, T. Manfredini, J.M. Guilemany, I.G. Cano, Building up WC-Co coatings by cold spray: A finite element simulation, Surf. Coat. Technol. 374 (2019) 674–689, https://doi.org/10.1016/j.surfcoat.2019.06.054.
[140] S. Yin, X. Suo, Y. Xie, W. Li, R. Lupoi, H. Liao, Effect of substrate temperature on interfacial bonding for cold spray of Ni onto Cu, J. Mater. Sci. 50 (2015) 7448–7457, https://doi.org/10.1007/s10853-015-9304-6.
[141] S. Weiller, F. Delloro, P. Lomonaco, M. Jeandin, C. Garion, A finite elements study on porosity creation mechanisms in cold sprayed coatings, Key Eng. Mater. 813 (2019) 358–363 (doi:10.4028/www.scientific.net/kem.813.358).
[142] A. Joshi, S. James, Molecular dynamics simulation study on effect of process parameters on coatings during cold spray process, Procedia Manuf. 26 (2018) 190–197, https://doi.org/10.1016/j.promfg.2018.07.026.
[143] A. Joshi, S. James, Molecular dynamics simulation study of cold spray process, J. Manuf. Process. 33 (2018) 136–143, https://doi.org/10.1016/j.jmapro.2018.05.005.
[144] D.C. Rapaport, R.L. Blumberg, S.R. McKay, W. Christian, The art of molecular dynamics simulation, Comput. Phys. 10 (1996) 456, https://doi.org/10.1063/1.4822471.
[145] T. Malama, A. Hamweendo, I. Botef, Molecular dynamics simulation of ti and ni particles on Ti substrate in the cold gas dynamic spray (CGDS) process, Mater. Sci. Forum 828–829 (2015) 453–460 (doi:10.4028/www.scientific.net/MSF.828-829.453).
[146] H. Gao, L. Zhao, D. Zeng, L. Gao, Molecular dynamics simulation of Au cluster depositing on Au surface in cold gas spray, in: Proc. 2007 First Int. Conf. Integr. Commer. Micro Nanosyst., ASME, Hainan, China, 2007, pp. 195–202, https://doi.org/10.1115/MNC2007-21609.
[147] H. Gao, C. Liu, F. Song, Molecular dynamics simulation of the influence factors of particle depositing on surface during cold spray, Adv. Mater. Res. 652–654 (2013) 1916–1924 (doi:10.4028/www.scientific.net/AMR.652-654.1916).
[148] S. Goel, N.H. Faisal, V. Ratia, A. Agrawal, A. Stukowski, Atomistic investigation on the structure-property relationship during thermal spray nanoparticle impact, Comput. Mater. Sci. 84 (2014) 163–174, https://doi.org/10.1016/j.commatsci.2013.12.011.
[149] T.S. Price, P.H. Shipway, D.G. McCartney, Effect of cold spray deposition of a titanium coating on fatigue behavior of a titanium alloy, J. Therm. Spray Technol. 15 (2006) 507–512, https://doi.org/10.1361/105996306X147108.
[150] G. Benenati, R. Lupoi, Development of a deposition strategy in cold spray for additive manufacturing to minimize residual stresses, in: 5th Procedia CIRP Glob. Web Conf. Res. Innov. Futur. Prod. Dev., The Author(s), 2016, pp. 101–108, https://doi.org/10.1016/j.procir.2016.08.042.
[151] Y.C. Tsui, T.W. Clyne, An analytical model for predicting residual stresses in progressively deposited coatings: Part 1: planar geometry, Thin Solid Films 306 (1997) 23–33, https://doi.org/10.1016/S0040-6090(97)00199-5.
[152] E. Lin, Q. Chen, O.C. Ozdemir, V.K. Champagne, S. Müftü, Effects of interface bonding on the residual stresses in cold-sprayed Al-6061: a numerical investigation, J. Therm. Spray Technol. 28 (2019) 472–483, https://doi.org/10.1007/s11666-019-00827-7.
[153] G. Shayegan, H. Mahmoudi, R. Ghelichi, J. Villafuerte, J. Wang, M. Guagliano, H. Jahed, Residual stress induced by cold spray coating of magnesium AZ31B extrusion, Mater. Des. 60 (2014) 72–84, https://doi.org/10.1016/j.matdes.2014.03.054.
[154] S.N.A. Yusof, A. Manap, N.F. Afandi, Numerical analysis of Al coating using different particle shape in LPCS, in: IOP Conf. Ser., Earth Environ. Sci., 2016, pp. 8–12, https://doi.org/10.1088/1755-1315/32/1/012038.
[155] F. Oviedo, A. Valarezo, Residual stress in high-velocity impact coatings: parametric finite element analysis approach, J. Therm. Spray Technol. (2020), https://doi.org/10.1007/s11666-020-01026-5.
[156] T.D. Phan, S. Masood, M. Jahedi, S. Zahiri, Residual stresses in cold spray process using finite element analysis, Mater. Sci. Forum 654–656 (2010) 1642–1645 (doi:10.4028/www.scientific.net/MSF.654-656.1642).
[157] Q. Wang, X. Luo, S. Tsutsumi, T. Sasaki, C. Li, N. Ma, Measurement and analysis of cold spray residual stress using arbitrary Lagrangian–Eulerian method, Addit. Manuf. 35 (2020) 101296, https://doi.org/10.1016/j.addma.2020.101296.
[158] E. Lin, I. Nault, O.C. Ozdemir, V.K. Champagne, A. Nardi, S. Müftü, Thermo-Mechanical Deformation History and the Residual Stress Distribution in Cold Spray, J. Therm. Spray Technol. (2020), https://doi.org/10.1007/s11666-020-01034-5.
[159] A.A. Abubakar, A.F.M. Arif, A hybrid computational approach for modeling thermal spray deposition, Surf. Coat. Technol. 362 (2019) 311–327, https://doi.org/10.1016/j.surfcoat.2019.02.010.
[160] A.A. Abubakar, A.F.M. Arif, S. Sohail Akhtar, K.S. Al-Athel, Prediction of residual stress and damage in thermal spray coatings using hybrid computational approach, in: ASME Int. Mech. Eng. Congr. Expo. Proc., Pittsburgh, Pennsylvania, USA, 2018, pp. 1–8, https://doi.org/10.1115/IMECE2018-86504.
[161] A.A. Abubakar, A.F.M. Arif, S.S. Akhtar, J. Mostaghimi, Splats formation, interaction and residual stress evolution in thermal spray coating using a hybrid computational model, J. Therm. Spray Technol. 28 (2019) 359–377, https://doi.org/10.1007/s11666-019-00828-6.
[162] C. Lyphout, A. Manescu, Residual Stresses Distribution through Thick HVOF Sprayed Inconel 718 Coatings, 2008, https://doi.org/10.1007/s11666-008-9242-9.
[163] J. Guo, H. Fu, B. Pan, R. Kang, Recent progress of residual stress measurement methods: A review, Chin. J. Aeronaut. (2020), https://doi.org/10.1016/j.cja.2019.10.010.
[164] S. Yin, X. Wang, X. Suo, H. Liao, Z. Guo, W. Li, C. Coddet, Deposition behavior of thermally softened copper particles in cold spraying, Acta Mater. 61 (2013) 5105–5118, https://doi.org/10.1016/j.actamat.2013.04.041.
[165] L. Zhu, T.C. Jen, Y.T. Pan, H.S. Chen, Particle bonding mechanism in cold gas dynamic spray: a three-dimensional approach, J. Therm. Spray Technol. 26 (2017) 1859–1873, https://doi.org/10.1007/s11666-017-0652-4.
[166] S. Shah, J. Lee, J.P. Rothstein, Numerical simulations of the high-velocity impact of a single polymer particle during cold-spray deposition, J. Therm. Spray Technol. 26 (2017) 970–984, https://doi.org/10.1007/s11666-017-0557-2.
[167] P.L. Fauchais, J.V.R. Heberlein, M.I. Boulos, Thermal Spray Fundamentals, 2014, https://doi.org/10.1007/978-0-387-68991-3.
[168] X. Teng, T. Wierzbicki, Numerical study on crack propagation in high velocity perforation, Comput. Struct. 83 (2005) 989–1004, https://doi.org/10.1016/j.compstruc.2004.12.001.
[169] B. Irhan, J. Ożbolt, D. Ruta, 3D finite element simulations of high velocity projectile impact, Int. J. Solids Struct. 72 (2015) 38–49, https://doi.org/10.1016/j.ijsolstr.2015.07.010.
[170] M. Fossati, M. Pagani, S. Miccoli, A. Manes, M. Giglio, Numerical calculation of crack parameters for propagation assessment in a complex component with residual stresses, Procedia Eng. 74 (2014) 360–367, https://doi.org/10.1016/j.proeng.2014.06.280.
[171] P. Cavaliere, Cold-Spray Coatings Recent Trends and Future Perspectives, 2020 (n.d.).
[172] T. Keller, G. Lindwall, S. Ghosh, L. Ma, B.M. Lane, F. Zhang, U.R. Kattner, E. A. Lass, J.C. Heigel, Y. Idell, M.E. Williams, A.J. Allen, J.E. Guyer, L.E. Levine, Application of finite element, phase-field, and CALPHAD-based methods to additive manufacturing of Ni-based superalloys, Acta Mater. 139 (2017) 244–253, https://doi.org/10.1016/j.actamat.2017.05.003.
[173] Y. Ji, L. Chen, L.Q. Chen, Understanding Microstructure Evolution During Additive Manufacturing of Metallic Alloys Using Phase-field Modeling, 1st ed., Elsevier Inc., 2018 https://doi.org/10.1016/B978-0-12-811820-7.00008-2.
[174] D. Deng, FEM prediction of welding residual stress and distortion in carbon steel considering phase transformation effects, Mater. Des. 30 (2009) 359–366, https://doi.org/10.1016/j.matdes.2008.04.052.
[175] R. Ahmed, A. Ashraf, M. Elameen, N.H. Faisal, A.M. El-Sherik, Y.O. Elakwah, M.F. A. Goosen, Single asperity nanoscratch behaviour of HIPed and cast Stellite 6 alloys, Wear 312 (2014) 70–82, https://doi.org/10.1016/j.wear.2014.02.006.
[176] P. Cavaliere, A. Perrone, A. Silvello, Cold-sprayed nanostructured pure cobalt coatings, J. Therm. Spray Technol. 25 (2016) 1168–1176, https://doi.org/10.1007/s11666-016-0434-4.
[177] G. Bolelli, A. Candeli, H. Koivuluoto, L. Lusvarghi, T. Manfredini, P. Vuoristo, Microstructure-based thermo-mechanical modelling of thermal spray coatings, Mater. Des. 73 (2015) 20–34, https://doi.org/10.1016/j.matdes.2015.02.014.
[178] V. Hegadekatte, N. Huber, O. Kraft, Finite element based simulation of dry sliding wear, Model. Simul. Mater. Sci. Eng. 13 (2004) 57–75, https://doi.org/10.1088/0965-0393/13/1/005.
[179] M.A. Ashraf, R. Ahmed, O. Ali, N.H. Faisal, A.M. El-Sherik, M.F.A. Goosen, Finite element modeling of sliding wear in a composite alloy using a free-mesh, J. Tribol. 137 (2015) 031605, https://doi.org/10.1115/1.4029998.
[180] B. Patham, X. Huang, Multiscale modeling of residual stress development in continuous fiber-reinforced unidirectional thick thermoset composites, J. Compos. 2014 (2014) 1–17, https://doi.org/10.1155/2014/172560.
[181] S. Kamnis, S. Gu, T.J. Lu, C. Chen, Numerical modeling the bonding mechanism of HVOF sprayed particles, Comput. Mater. Sci. 46 (2009) 1038–1043, https://doi.org/10.1016/j.commatsci.2009.05.009.
[182] R.C. Dykhuizen, M.F. Smith, D.L. Gilmore, R. a Neiser, X. Jiang, S. Sampath, Impact of high velocity cold spray particles, J. Therm. Spray Technol. 8 (1999) 559–564, https://doi.org/10.1361/105996399770350250.
[183] W.Y. Li, M. Yu, F.F. Wang, S. Yin, H.L. Liao, A generalized critical velocity window based on material property for cold spraying by eulerian method, J. Therm. Spray Technol. 23 (2014) 557–566, https://doi.org/10.1007/s11666-013-0023-8.
[184] F.F. Wang, W.Y. Li, M. Yu, H.L. Liao, Prediction of critical velocity during cold spraying based on a coupled thermomechanical eulerian model, J. Therm. Spray Technol. 23 (2014) 60–67, https://doi.org/10.1007/s11666-013-0009-6.
[185] M.J. Azizpour, S. Norouzi, D. Sajedipour, An Axisymmetrical finite element model for prediction of the bonding behavior in HVOF thermal spraying coatings, J. Appl. Sci. 12 (2012) 492–497, https://doi.org/10.3923/jas.2012.492.497.
[186] R. Nikbakht, S.H. Seyedein, S. Kheirandish, H. Assadi, B. Jodoin, Asymmetrical bonding in cold spraying of dissimilar materials, Appl. Surf. Sci. 444 (2018) 621–632, https://doi.org/10.1016/j.apsusc.2018.03.103.
[187] X. Wang, F. Feng, M.A. Klecka, M.D. Mordasky, J.K. Garofano, T. El-Wardany, A. Nardi, V.K. Champagne, Characterization and modeling of the bonding process in cold spray additive manufacturing, Addit. Manuf. 8 (2015) 149–162, https://doi.org/10.1016/j.addma.2015.03.006.
[188] R. Fernandez, B. Jodoin, Cold Spray Aluminum–Alumina Cermet Coatings: Effect of Alumina Content, J. Therm. Spray Technol. 27 (2018) 603–623, https://doi.org/10.1007/s11666-018-0702-6.
[189] M. Yu, W.Y. Li, F.F. Wang, H.L. Liao, Effect of preheating on deformation in cold spraying dissimilar combinations, Surf. Eng. 30 (2014) 329–334, https://doi.org/10.1179/1743294413Y.0000000203.
[190] A.W.Y. Tan, J.Y. Lek, W. Sun, A. Bhowmik, I. Marinescu, X. Song, W. Zhai, F. Li, Z. Dong, C.B. Boothroyd, E. Liu, Influence of particle velocity when propelled

using N2 or N2-He mixed gas on the properties of cold-sprayed Ti6Al4V coatings, Coatings 8 (2018) 327, https://doi.org/10.3390/COATINGS8090327.
[191] S. Dosta, G. Bolelli, A. Candeli, L. Lusvarghi, I.G. Cano, J.M. Guilemany, Plastic deformation phenomena during cold spray impact of WC-Co particles onto metal substrates, Acta Mater. 124 (2017) 173–181, https://doi.org/10.1016/j.actamat.2016.11.010.
[192] F. Meng, S. Yue, J. Song, Quantitative prediction of critical velocity and deposition efficiency in cold-spray: A finite-element study, Scr. Mater. 107 (2015) 83–87, https://doi.org/10.1016/j.scriptamat.2015.05.026.
[193] F. Meng, H. Aydin, S. Yue, J. Song, The Effects of Contact Conditions on the Onset of Shear Instability in Cold-Spray, J. Therm. Spray Technol. 24 (2015) 711–719, https://doi.org/10.1007/s11666-015-0229-z.
[194] F. Wang, M. Zhao, Simulation of particle deposition behavior in cold-sprayed mg anticorrosion coating, Mater. Manuf. Process. 31 (2016) 1483–1489, https://doi.org/10.1080/10426914.2014.952042.
[195] P. Profizi, A. Combescure, K. Ogawa, SPH modeling of adhesion in fast dynamics: application to the cold spray process, Comptes Rendus - Mec. 344 (2016) 211–224, https://doi.org/10.1016/j.crme.2016.02.001.
[196] S. Yin, X. Wang, W. Li, H. Liao, H. Jie, Deformation behavior of the oxide film on the surface of cold sprayed powder particle, Appl. Surf. Sci. 259 (2012) 294–300, https://doi.org/10.1016/j.apsusc.2012.07.036.
[197] S. Rahmati, A. Ghaei, The use of particle/substrate material models in simulation of cold-gas dynamic-spray process, J. Therm. Spray Technol. 23 (2014) 530–540, https://doi.org/10.1007/s11666-013-0051-4.
[198] R. Chakrabarty, J. Song, Numerical simulations of ceramic deposition and retention in metal-ceramic composite cold spray, Surf. Coat. Technol. 385 (2020) 125324, https://doi.org/10.1016/j.surfcoat.2019.125324.
[199] X. Song, K.L. Ng, J.M.K. Chea, W. Sun, A.W.Y. Tan, W. Zhai, F. Li, I. Marinescu, E. Liu, Coupled Eulerian-Lagrangian (CEL) simulation of multiple particle impact during Metal Cold Spray process for coating porosity prediction, Surf. Coat. Technol. 385 (2020) 125433, https://doi.org/10.1016/j.surfcoat.2020.125433.
[200] S.T. Oyinbo, T.C. Jen, Investigation of the process parameters and restitution coefficient of ductile materials during cold gas dynamic spray (CGDS) using finite element analysis, Addit. Manuf. 31 (2020) 100986, https://doi.org/10.1016/j.addma.2019.100986.
[201] Y. Xie, C. Chen, M.P. Planche, S. Deng, H. Liao, Effect of spray angle on Ni particle deposition behaviour in cold spray, Surf. Eng. 34 (2018) 352–360, https://doi.org/10.1080/02670844.2017.1312221.
[202] S. Kumar, G. Bae, C. Lee, Influence of substrate roughness on bonding mechanism in cold spray, Surf. Coat. Technol. 304 (2016) 592–605, https://doi.org/10.1016/j.surfcoat.2016.07.082.
[203] F. Meng, D. Hu, Y. Gao, S. Yue, J. Song, Cold-spray bonding mechanisms and deposition efficiency prediction for particle/substrate with distinct deformability, Mater. Des. 109 (2016) 503–510, https://doi.org/10.1016/j.matdes.2016.07.103.
[204] W. Sun, A.W.Y. Tan, A. Bhowmik, I. Marinescu, X. Song, W. Zhai, F. Li, E. Liu, Deposition characteristics of cold sprayed Inconel 718 particles on Inconel 718 substrates with different surface conditions, Mater. Sci. Eng. A 720 (2018) 75–84, https://doi.org/10.1016/j.msea.2018.02.059.
[205] S. Yin, H.L. Liao, X.F. Wang, Euler based finite element analysis on high velocity impact behaviour in cold spraying, Surf. Eng. 30 (2014) 309–315, https://doi.org/10.1179/1743294413Y.0000000240.
[206] G. Bae, S. Kumar, S. Yoon, K. Kang, H. Na, H.J. Kim, C. Lee, Bonding features and associated mechanisms in kinetic sprayed titanium coatings, Acta Mater. 57 (2009) 5654–5666, https://doi.org/10.1016/j.actamat.2009.07.061.
[207] S. Yin, X.F. Wang, W.Y. Li, H.E. Jie, Effect of substrate hardness on the deformation behavior of subsequently incident particles in cold spraying, Appl. Surf. Sci. 257 (2011) 7560–7565, https://doi.org/10.1016/j.apsusc.2011.03.126.
[208] W.Y. Li, J. Wang, H. Zhu, H. Li, C. Huang, On ultrahigh velocity micro-particle impact on steels - a single impact study, Wear 305 (2013) 216–227, https://doi.org/10.1016/j.wear.2013.06.011.
[209] H. Ashrafizadeh, F. Ashrafizadeh, A numerical 3D simulation for prediction of wear caused by solid particle impact, Wear 276–277 (2012) 75–84, https://doi.org/10.1016/j.wear.2011.12.003.
[210] X.L. Zhou, S.J. Mou, X.K. Wu, J.S. Zhang, Deposition behavior of mixed binary metallic powders in cold spraying process, Appl. Surf. Sci. 257 (2011) 10628–10633, https://doi.org/10.1016/j.apsusc.2011.07.061.
[211] R. Ghelichi, S. Bagherifard, M. Guagliano, M. Verani, Numerical simulation of cold spray coating, Surf. Coat. Technol. 205 (2011) 5294–5301, https://doi.org/10.1016/j.surfcoat.2011.05.038.
[212] A. Moridi, S.M. Hassani-Gangaraj, M. Guagliano, A hybrid approach to determine critical and erosion velocities in the cold spray process, Appl. Surf. Sci. 273 (2013) 617–624, https://doi.org/10.1016/j.apsusc.2013.02.089.
[213] K.H. Kim, M. Watanabe, S. Kuroda, Bonding mechanisms of thermally softened metallic powder particles and substrates impacted at high velocity, Surf. Coat. Technol. 204 (2010) 2175–2180, https://doi.org/10.1016/j.surfcoat.2009.12.001.
[214] S. Guetta, M.H. Berger, F. Borit, V. Guipont, M. Jeandin, M. Boustie, Y. Ichikawa, K. Sakaguchi, K. Ogawa, Influence of particle velocity on adhesion of cold-sprayed splats, J. Therm. Spray Technol. 18 (2009) 331–342, https://doi.org/10.1007/s11666-009-9327-0.
[215] V. Lemiale, Y. Estrin, H.S. Kim, R. O'Donnell, Forming nanocrystalline structures in metal particle impact, Metall. Mater. Trans. A. 42 (2011) 3006–3012, https://doi.org/10.1007/s11661-010-0588-5.
[216] S. Yin, P. He, H. Liao, X. Wang, Deposition features of Ti coating using irregular powders in cold spray, J. Therm. Spray Technol. 23 (2014) 984–990, https://doi.org/10.1007/s11666-014-0116-z.
[217] O. Bielousova, J. Kocimski, R.G. Maev, I. Smurov, W. Scharff, V. Leshchynsky, Localisation of deformation in cold gas dynamic spraying, Surf. Eng. 32 (2016) 655–662, https://doi.org/10.1179/1743294415Y.0000000059.
[218] P.V. Cavallaro, A.W. Hulton, Interfacial fracture behaviors of single particle impacts during aluminum cold spray additive manufacturing and repair process, in: Proc. ASME 2017 Int. Mech. Eng. Congr. Expo., 2017, pp. 1–9, https://doi.org/10.1115/IMECE2017-70621.
[219] A. Nastic, M. Vijay, A. Tieu, S. Rahmati, B. Jodoin, Experimental and Numerical Study of the Influence of Substrate Surface Preparation on Adhesion Mechanisms of Aluminum Cold Spray Coatings on 300M Steel Substrates, J. Therm. Spray Technol. 26 (2017) 1461–1483, https://doi.org/10.1007/s11666-017-0602-1.
[220] A. Viscusi, Numerical investigations on the rebound phenomena and the bonding mechanisms in cold spray processes, in: AIP Conf. Proc., 2018, p. 100017, https://doi.org/10.1063/1.5034957.
[221] Y. Liu, C. xin Li, X.F. Huang, K. Ma, X.T. Luo, C.J. Li, Effect of water environment on particle deposition of underwater cold spray, Appl. Surf. Sci. 506 (2020) 144542, https://doi.org/10.1016/j.apsusc.2019.144542.
[222] C. Sun, X. Zhou, L. Xu, C. Xie, Effect of preheating on the deformation in cold spraying, Surf. Eng. 34 (2018) 791–799, https://doi.org/10.1080/02670844.2017.1412892.
[223] C. Sun, X. Zhou, C. Xie, B. Liu, Investigating hard/soft combinations of cold spraying by Eulerian approach, Surf. Eng. (2020) 1–9, https://doi.org/10.1080/02670844.2019.1710036.
[224] V. Lemiale, P.C. King, M. Rudman, M. Prakash, P.W. Cleary, M.Z. Jahedi, S. Gulizia, Temperature and strain rate effects in cold spray investigated by smoothed particle hydrodynamics, Surf. Coat. Technol. 254 (2014) 121–130, https://doi.org/10.1016/j.surfcoat.2014.05.071.
[225] R. Chakrabarty, J. Song, Effect of impact angle on ceramic deposition behavior in composite cold spray: a finite-element study, J. Therm. Spray Technol. 26 (2017) 1434–1444, https://doi.org/10.1007/s11666-017-0604-z.
[226] Z. Arabgol, M. Villa Vidaller, H. Assadi, F. Gärtner, T. Klassen, Influence of thermal properties and temperature of substrate on the quality of cold-sprayed deposits, Acta Mater. 127 (2017) 287–301, https://doi.org/10.1016/j.actamat.2017.01.040.
[227] K.H. Leitz, M. O'Sullivan, A. Plankensteiner, H. Kestler, L.S. Sigl, OpenFOAM modeling of particle heating and acceleration in cold spraying, J. Therm. Spray Technol. 27 (2018) 135–144, https://doi.org/10.1007/s11666-017-0644-4.
[228] Y. Liu, C. Xu, Investigating the cold spraying process with the material point method, Int. J. Mech. Mater. Des. 15 (2019) 361–378, https://doi.org/10.1007/s10999-018-9419-4.
[229] S. Yin, Y. Xie, J. Cizek, E.J. Ekoi, T. Hussain, D.P. Dowling, R. Lupoi, Advanced diamond-reinforced metal matrix composites via cold spray: Properties and deposition mechanism, Compos. Part B Eng. 113 (2017) 44–54, https://doi.org/10.1016/j.compositesb.2017.01.009.
[230] S.N.A. Yusof, A. Manap, H. Misran, S.Z. Othman, Computational analysis of single and multiple impacts of low pressure and high pressure cold sprayed aluminum particles using SPH, Adv. Mater. Res. 974 (2014) 147–151 (doi:10.4028/www.scientific.net/AMR.974.147).
[231] S. Yin, X. Suo, J. Su, Z. Guo, H. Liao, X. Wang, Effects of substrate hardness and spray angle on the deposition behavior of cold-sprayed ti particles, J. Therm. Spray Technol. 23 (2014) 76–83, https://doi.org/10.1007/s11666-013-0039-0.
[232] H. Jami, A. Jabbarzadeh, Unravelling ultrafast deformation mechanisms in surface deposition of titanium nanoparticles, Appl. Surf. Sci. 489 (2019) 446–461, https://doi.org/10.1016/j.apsusc.2019.05.271.
[233] K. Ito, Y. Ichikawa, K. Ogawa, Experimental and numerical analyses on the deposition behavior of spherical aluminum particles in the cold-spray-emulated high-velocity impact process, Mater. Trans. 57 (2016) 525–532, https://doi.org/10.2320/matertrans.T-M2016803.
[234] R.G. Maev, V. Leshchynsky, E. Strumban, D. Dzhurinskiy, J. Kocimski, E. Maeva, Structure and Mechanical Properties of Thick Copper Coating Made by Cold Spray, J. Therm. Spray Technol. 25 (2016) 113–122, https://doi.org/10.1007/s11666-015-0313-4.
[235] D.K. Christoulis, S. Guetta, V. Guipont, M. Jeandin, The influence of the substrate on the deposition of cold-sprayed titanium: an experimental and numerical study, J. Therm. Spray Technol. 20 (2010) 523–533, https://doi.org/10.1007/s11666-010-9608-7.
[236] S. Kumar, M. Ramakrishna, N.M. Chavan, S.V. Joshi, Correlation of splat state with deposition characteristics of cold sprayed niobium coatings, Acta Mater. 130 (2017) 177–195, https://doi.org/10.1016/j.actamat.2017.03.023.
[237] Y. Ichikawa, K. Ogawa, Critical deposition condition of CoNiCrAlY cold spray based on particle deformation behavior, J. Therm. Spray Technol. 26 (2017) 340–349, https://doi.org/10.1007/s11666-016-0477-6.
[238] J. Henao, A. Concustell, S. Dosta, G. Bolelli, I.G. Cano, L. Lusvarghi, J. M. Guilemany, Deposition mechanisms of metallic glass particles by Cold Gas Spraying, Acta Mater. 125 (2017) 327–339, https://doi.org/10.1016/j.actamat.2016.12.007.
[239] R. Fernandez, B. Jodoin, Effect of Particle Morphology on Cold Spray Deposition of Chromium Carbide-Nickel Chromium Cermet Powders, J. Therm. Spray Technol. 26 (2017) 1356–1380, https://doi.org/10.1007/s11666-017-0580-3.
[240] C. Sun, X. Zhou, C. Xie, L. Xu, R. Li, B. Liu, Formation of Al-based amorphous/nanocrystalline coatings by cold spraying, Surf. Coat. Technol. 389 (2020) 125644, https://doi.org/10.1016/j.surfcoat.2020.125644.

[241] C. Chen, X. Xie, Y. Xie, X. Yan, C. Huang, S. Deng, Z. Ren, H. Liao, Metallization of polyether ether ketone (PEEK) by copper coating via cold spray, Surf. Coat. Technol. 342 (2018) 209–219, https://doi.org/10.1016/j.surfcoat.2018.02.087.
[242] W. Ma, Y. Xie, C. Chen, H. Fukanuma, J. Wang, Z. Ren, R. Huang, Microstructural and mechanical properties of high-performance Inconel 718 alloy by cold spraying, J. Alloys Compd. 792 (2019) 456–467, https://doi.org/10.1016/j.jallcom.2019.04.045.
[243] M.K. Hamiyanze, T.-C. Jen, Numerical analysis of the cold gas dynamic spray surface coating process, in: Proc. Second Int. Conf. Mech. Mater. Struct. Eng. (ICMMSE 2017), 2017, pp. 75–79, https://doi.org/10.2991/icmmse-17.2017.13.
[244] R. Chakrabarty, J. Song, A modified Johnson-Cook material model with strain gradient plasticity consideration for numerical simulation of cold spray process, Surf. Coat. Technol. 397 (2020) 125981, https://doi.org/10.1016/j.surfcoat.2020.125981.
[245] G. Montay, A. Cherouat, J. Lu, N. Baradel, L. Bianchi, Development of the high-precision incremental-step hole-drilling method for the study of residual stress in multi-layer materials: Influence of temperature and substrate on ZrO2-Y2O38 wt % coatings, Surf. Coat. Technol. 155 (2002) 152–160, https://doi.org/10.1016/S0257-8972(01)01718-2.
[246] B. Yıldırım, A. Hulton, S.A. Alavian, T. Ando, A. Gouldstone, S. Müftü, On simulation of multi-particle impact interactions in the cold spray process, in: Proc. ASME/STLE 2012 Int. Jt. Tribol. Conf., ASME, Denver, Colorado, USA, 2012, pp. 83–85, https://doi.org/10.1115/IJTC2012-61202.
[247] S. Pathak, G.C. Saha, Development of sustainable cold spray coatings and 3D additive manufacturing components for repair/manufacturing applications: a critical review, Coatings 7 (2017) 122, https://doi.org/10.3390/coatings7080122.
[248] Matweb, Copper, Cu, Annealed, Matweb Mater. Prop. Data., 2020. http://www.matweb.com/search/datasheet_print.aspx?matguid=9aebe83845c04c1db5126fada6f76f7e. (Accessed 3 August 2020).
[249] Matweb, Aluminum, Al, Matweb Mater. Prop. Data., 2020. http://www.matweb.com/search/datasheet.aspx?bassnum=AMEAL00&ckck=1. (Accessed 3 August 2020).
[250] AZoM, Nickel - Properties, Fabrication and Applications of Commercially Pure Nickel, AZoM, 2003. https://www.azom.com/properties.aspx?ArticleID=2193. (Accessed 3 August 2020).
[251] AzoM, Stainless Steel - Grade 316 (UNS S31600), AZoM, 2001. https://www.azom.com/properties.aspx?ArticleID=863. (Accessed 3 August 2020).
[252] AZoM, Nickel Alloy Inconel 718 - Properties and Applications by United Performance Metals, AZoM, 2008. https://www.azom.com/article.aspx?ArticleID=4459. (Accessed 3 August 2020).
[253] AZoM, Iron (Fe) - Properties, Applications, AZoM, 2013. https://www.azom.com/article.aspx?ArticleID=9094. (Accessed 3 August 2020).
[254] AZoM, Stainless Steel - Grade 304 (UNS S30400), AZoM, 2001. https://www.azom.com/article.aspx?ArticleID=965. (Accessed 3 August 2020).
[255] AZoM, Niobium, Nb (Formerly Columbium, Cb) - Properties, Applications, AZoM, 2013. https://www.azom.com/article.aspx?ArticleID=9558. (Accessed 3 August 2020).
[256] AZoM, Titanium Alloys - Ti6Al4V Grade 5, AZoM, 2002. https://www.azom.com/properties.aspx?ArticleID=1547. (Accessed 3 August 2020).